



The Early Data Release of the Dark Energy Spectroscopic Instrument

DESI Collaboration,

A. G. Adame¹, J. Aguilar², S. Ahlen³, S. Alam⁴, G. Aldering², D. M. Alexander^{5,6}, R. Alfarsy⁷, C. Allende Prieto^{8,9}, M. Alvarez², O. Alves¹⁰, A. Anand², F. Andrade-Oliveira¹⁰, E. Armengaud¹¹, J. Asorey¹², S. Avila¹³, A. Aviles^{14,15}, S. Bailey², A. Balaguera-Antolínez^{8,9}, O. Ballester¹³, C. Baltay¹⁶, A. Bault¹⁷, J. Bautista¹⁸, J. Behera¹⁹, S. F. Beltran²⁰, S. BenZvi²¹, L. Beraldo e Silva^{10,22}, J. R. Bermejo-Climent²¹, A. Berti²³, R. Besuner^{24,25}, F. Beutler²⁶, D. Bianchi²⁷, C. Blake²⁸, R. Blum²⁹, A. S. Bolton²⁹, S. Brieden²⁶, A. Brodzeller²³, D. Brooks³⁰, Z. Brown²¹, E. Buckley-Geer^{31,32}, E. Burtin¹¹, L. Cabayol-Garcia¹³, Z. Cai^{33,34,35}, R. Canning⁷, L. Cardiel-Sas¹³, A. Carnero Rosell^{8,9}, F. J. Castander^{36,37}, J. L. Cervantes-Cota¹⁵, S. Chabanier², E. Chaussidon¹¹, J. Chaves-Montero¹³, S. Chen³⁸, X. Chen¹⁶, C. Chuang^{23,39,40}, T. Claybaugh², S. Cole⁶, A. P. Cooper⁴¹, A. Cuceu^{42,43,44}, T. M. Davis⁴⁵, K. Dawson²³, R. de Belsunce^{2,46}, R. de la Cruz²⁰, A. de la Macorra⁴⁷, J. Della Costa⁴⁸, A. de Mattia¹¹, R. Demina²¹, U. Demirbozan¹³, J. DeRose², A. Dey²⁹, B. Dey⁴⁹, G. Dhungana⁵⁰, J. Ding³⁵, Z. Ding⁵¹, P. Doel³⁰, R. Doshi⁵², K. Douglass²¹, A. Edge⁶, S. Eftekharzadeh⁵³, D. J. Eisenstein⁵⁴, A. Elliott^{43,44}, J. Ereira⁵⁷, S. Escoffier¹⁸, P. Fagrelus²⁹, X. Fan⁵⁵, K. Fanning⁴⁴, V. A. Fawcett⁵⁶, S. Ferraro^{2,25}, B. Flaugher³², A. Font-Ribera¹³, J. E. Forero-Romero^{59,60}, D. Forero-Sánchez⁵⁸, C. S. Frenk⁶, B. T. Gänsicke⁶¹, L. Á. García⁶², J. García-Bellido¹, C. Garcia-Quintero⁶³, L. H. Garrison^{64,65}, H. Gil-Marín⁶⁶, J. Golden-Marx⁵¹, S. Gontcho A Gontcho², A. X. Gonzalez-Morales^{14,20}, V. Gonzalez-Perez^{1,67}, C. Gordon¹³, O. Graur⁷, D. Green¹⁷, D. Gruen^{68,69}, J. Guy², B. Hadzhiyska^{2,25}, C. Hahn⁷⁰, J. J. Han⁵⁴, M. M. S Hanif¹⁰, H. K. Herrera-Alcántar²⁰, K. Honscheid^{42,43,44}, J. Hou⁷¹, C. Howlett⁴⁵, D. Huterer^{10,72}, V. Iršič⁴⁶, M. Ishak⁶³, A. Jacques²⁹, A. Jana¹⁹, L. Jiang⁷³, J. Jimenez¹³, Y. P. Jing⁵¹, S. Joudaki⁷⁴, R. Joyce²⁹, E. Jullo⁷⁵, S. Juneau²⁹, N. G. Karaçaylı^{42,43,44,76}, T. Karim⁵⁴, R. Kehoe⁵⁰, S. Kent^{31,32}, A. Khederlarian⁴⁹, S. Kim⁷⁷, D. Kirkby¹⁷, T. Kisner², F. Kitaura^{8,9}, N. Kizhuprakkat⁴¹, J. Kneib⁵⁸, S. E. Kposov^{26,78}, A. Kovács^{79,80}, A. Kremin², A. Krowleski^{74,81,82}, B. L'Huillier⁸³, O. Lahav³⁰, A. Lambert², C. Lamman⁵⁴, T.-W. Lan⁸⁴, M. Landriau², D. Lang⁸¹, J. U. Lange^{10,72}, J. Lasker⁵⁰, A. Leauthaud^{33,35}, L. Le Guillou⁸⁵, M. E. Levi², T. S. Li⁸⁶, E. Linder^{2,24,25}, A. Lyons⁸⁷, C. Magneville¹¹, M. Manera^{13,88}, C. J. Manser^{61,89}, D. Margala², P. Martini^{42,44,76}, P. McDonald², G. E. Medina⁸⁶, L. Medina-Varela⁶³, A. Meisner²⁹, J. Mena-Fernández¹², J. Meneses-Rizo⁴⁷, M. Mezcua^{36,37}, R. Miquel^{13,90}, P. Montero-Camacho³⁴, J. Moon⁸³, S. Moore⁶, J. Moustakas⁹¹, E. Mueller⁹², J. Mundet¹³, A. Muñoz-Gutiérrez⁴⁷, A. D. Myers⁹³, S. Nadathur⁷, L. Napolitano⁹³, R. Neveux²⁶, J. A. Newman⁴⁹, J. Nie⁹⁴, R. Nikutta²⁹, G. Niz^{20,95}, P. Norberg^{5,6}, H. E. Noriega⁴⁷, E. Paillas⁷⁴, N. Palanque-Delabrouille^{2,11}, A. Palmese⁹⁶, Z. Pan⁷³, D. Parkinson⁹⁷, S. Penmetsa⁷⁴, W. J. Percival^{74,81,82}, A. Pérez-Fernández⁴⁷, I. Pérez-Ràfols⁹⁸, M. Pieri⁷⁵, C. Poppett^{2,24,25}, A. Porredon^{26,44}, S. Pothier²⁹, F. Prada⁵⁷, R. Pucha⁵⁵, A. Raichoor², C. Ramírez-Pérez¹³, S. Ramirez-Solano⁴⁷, M. Rashkovetskiy⁵⁴, C. Ravoux^{11,18}, A. Rocher¹¹, C. Rockosi^{33,35,99}, A. J. Ross^{42,44,76}, G. Rossi⁸³, R. Ruggeri^{28,45}, V. Ruhlmann-Kleider¹¹, C. G. Sabiu⁷⁷, K. Said⁴⁵, A. Saintonge³⁰, L. Samushia^{19,100,101}, E. Sanchez¹², C. Saulder⁹⁷, E. Schaan⁴⁰, E. F. Schlafly¹⁰², D. Schlegel², D. Scholte³⁰, M. Schubnell^{10,72}, H. Seo¹⁰³, A. Shafieloo⁹⁷, R. Sharples^{6,104}, W. Sheu¹⁰⁵, J. Silber², F. Sinigaglia^{8,9}, M. Siudek³⁷, Z. Slepian^{2,71}, A. Smith⁶, M. T. Soumagnac^{2,106}, D. Sprayberry²⁹, L. Stephey², J. Suárez-Pérez⁵⁹, Z. Sun³⁴, T. Tan⁸⁵, G. Tarlé¹⁰, R. Tojeiro¹⁰⁷, L. A. Ureña-López²⁰, R. Vaisakh⁵⁰, D. Valcin¹⁰³, F. Valdes²⁹, M. Valluri^{10,22}, M. Vargas-Magaña⁴⁷, A. Variu⁵⁸, L. Verde^{66,90}, M. Walther^{68,69}, B. Wang^{34,108}, M. S. Wang²⁶, B. A. Weaver²⁹, N. Weaverdyck², R. H. Wechsler^{39,40,109}, M. White^{25,52}, Y. Xie⁶³, J. Yang⁵⁵, C. Yèche¹¹, J. Yu⁵⁸, S. Yuan⁴⁰, H. Zhang¹⁹, Z. Zhang⁵², C. Zhao^{34,58}, Z. Zheng²³, R. Zhou², Z. Zhou⁹⁴, H. Zou⁹⁴, S. Zou³⁴, and Y. Zu^{42,51,110}

¹ Instituto de Física Teórica (IFT) UAM/CSIC, Universidad Autónoma de Madrid, Cantoblanco, E-28049, Madrid, Spain; spokespersons@desi.lbl.gov² Lawrence Berkeley National Laboratory, 1 Cyclotron Road, Berkeley, CA 94720, USA³ Physics Dept., Boston University, 590 Commonwealth Avenue, Boston, MA 02215, USA⁴ Tata Institute of Fundamental Research, Homi Bhabha Road, Mumbai 400005, India⁵ Centre for Extragalactic Astronomy, Department of Physics, Durham University, South Road, Durham, DH1 3LE, UK⁶ Institute for Computational Cosmology, Department of Physics, Durham University, South Road, Durham DH1 3LE, UK⁷ Institute of Cosmology & Gravitation, University of Portsmouth, Dennis Sciama Building, Portsmouth, PO1 3FX, UK⁸ Departamento de Astrofísica, Universidad de La Laguna (ULL), E-38206, La Laguna, Tenerife, Spain⁹ Instituto de Astrofísica de Canarias, C/ Vía Láctea, s/n, E-38205 La Laguna, Tenerife, Spain¹⁰ University of Michigan, Ann Arbor, MI 48109, USA¹¹ IRFU, CEA, Université Paris-Saclay, F-91191 Gif-sur-Yvette, France¹² CIEMAT, Avenida Complutense 40, E-28040 Madrid, Spain¹³ Institut de Física d'Altes Energies (IFAE), The Barcelona Institute of Science and Technology, Campus UAB, 08193 Bellaterra Barcelona, Spain¹⁴ Consejo Nacional de Ciencia y Tecnología, Av. Insurgentes Sur 1582. Colonia Crédito Constructor, Del. Benito Juárez C.P. 03940, México D.F., México¹⁵ Departamento de Física, Instituto Nacional de Investigaciones Nucleares, Carretera México-Toluca S/N, La Marquesa, Ocoyoacac, Edo. de México C.P. 52750, México¹⁶ Physics Department, Yale University, P.O. Box 208120, New Haven, CT 06511, USA¹⁷ Department of Physics and Astronomy, University of California, Irvine, CA 92697, USA¹⁸ Aix Marseille Univ, CNRS/IN2P3, CPPM, Marseille, France

- ¹⁹ Department of Physics, Kansas State University, 116 Cardwell Hall, Manhattan, KS 66506, USA
- ²⁰ Departamento de Física, Universidad de Guanajuato—DCI, C.P. 37150, Leon, Guanajuato, México
- ²¹ Department of Physics & Astronomy, University of Rochester, 206 Bausch and Lomb Hall, P.O. Box 270171, Rochester, NY 14627-0171, USA
- ²² Department of Astronomy, University of Michigan, Ann Arbor, MI 48109, USA
- ²³ Department of Physics and Astronomy, The University of Utah, 115 South 1400 East, Salt Lake City, UT 84112, USA
- ²⁴ Space Sciences Laboratory, University of California, Berkeley, 7 Gauss Way, Berkeley, CA 94720, USA
- ²⁵ University of California, Berkeley, 110 Sproul Hall #5800 Berkeley, CA 94720, USA
- ²⁶ Institute for Astronomy, University of Edinburgh, Royal Observatory, Blackford Hill, Edinburgh EH9 3HJ, UK
- ²⁷ Dipartimento di Fisica “Aldo Pontremoli,” Università degli Studi di Milano, Via Celoria 16, I-20133 Milano, Italy
- ²⁸ Centre for Astrophysics & Supercomputing, Swinburne University of Technology, P.O. Box 218, Hawthorn, VIC 3122, Australia
- ²⁹ NSF’s NOIRLab, 950 N. Cherry Avenue, Tucson, AZ 85719, USA
- ³⁰ Department of Physics & Astronomy, University College London, Gower Street, London, WC1E 6BT, UK
- ³¹ Department of Astronomy and Astrophysics, University of Chicago, 5640 South Ellis Avenue, Chicago, IL 60637, USA
- ³² Fermi National Accelerator Laboratory, P.O. Box 500, Batavia, IL 60510, USA
- ³³ Department of Astronomy and Astrophysics, University of California, Santa Cruz, 1156 High Street, Santa Cruz, CA 95065, USA
- ³⁴ Department of Astronomy, Tsinghua University, 30 Shuangqing Road, Haidian District, Beijing, 100190, People’s Republic of China
- ³⁵ Department of Astronomy and Astrophysics, UCO/Lick Observatory, University of California, 1156 High Street, Santa Cruz, CA 95064, USA
- ³⁶ Institut d’Estudis Espacials de Catalunya (IEEC), 08034 Barcelona, Spain
- ³⁷ Institute of Space Sciences, ICE-CSIC, Campus UAB, Carrer de Can Magrans s/n, 08913 Bellaterra, Barcelona, Spain
- ³⁸ Institute for Advanced Study, 1 Einstein Drive, Princeton, NJ 08540, USA
- ³⁹ Physics Department, Stanford University, Stanford, CA 93405, USA
- ⁴⁰ SLAC National Accelerator Laboratory, Menlo Park, CA 94305, USA
- ⁴¹ Institute of Astronomy and Department of Physics, National Tsing Hua University, 101 Kuang-Fu Road Sec. 2, Hsinchu 30013, Taiwan
- ⁴² Center for Cosmology and AstroParticle Physics, The Ohio State University, 191 West Woodruff Avenue, Columbus, OH 43210, USA
- ⁴³ Department of Physics, The Ohio State University, 191 West Woodruff Avenue, Columbus, OH 43210, USA
- ⁴⁴ The Ohio State University, Columbus, 43210 OH, USA
- ⁴⁵ School of Mathematics and Physics, University of Queensland, 4072, Australia
- ⁴⁶ Kavli Institute for Cosmology, University of Cambridge, Madingley Road, Cambridge CB3 0HA, UK
- ⁴⁷ Instituto de Física, Universidad Nacional Autónoma de México, Cd. de México C.P. 04510, México
- ⁴⁸ Department of Astronomy, San Diego State University, 5500 Campanile Drive, San Diego, CA 92182, USA
- ⁴⁹ Department of Physics & Astronomy and Pittsburgh Particle Physics, Astrophysics, and Cosmology Center (PITT PACC), University of Pittsburgh, 3941 O’Hara Street, Pittsburgh, PA 15260, USA
- ⁵⁰ Department of Physics, Southern Methodist University, 3215 Daniel Avenue, Dallas, TX 75275, USA
- ⁵¹ Department of Astronomy, School of Physics and Astronomy, Shanghai Jiao Tong University, Shanghai 200240, People’s Republic of China
- ⁵² Department of Physics, University of California, Berkeley, 366 LeConte Hall MC 7300, Berkeley, CA 94720-7300, USA
- ⁵³ Universities Space Research Association, NASA Ames Research Center, USA
- ⁵⁴ Center for Astrophysics | Harvard & Smithsonian, 60 Garden Street, Cambridge, MA 02138, USA
- ⁵⁵ Steward Observatory, University of Arizona, 933 N, Cherry Avenue, Tucson, AZ 85721, USA
- ⁵⁶ School of Mathematics, Statistics and Physics, Newcastle University, Newcastle, UK
- ⁵⁷ Instituto de Astrofísica de Andalucía (CSIC), Glorieta de la Astronomía, s/n, E-18008 Granada, Spain
- ⁵⁸ Ecole Polytechnique Fédérale de Lausanne, CH-1015 Lausanne, Switzerland
- ⁵⁹ Departamento de Física, Universidad de los Andes, Cra. 1 No. 18A-10, Edificio Ip, CP 111711, Bogotá, Colombia
- ⁶⁰ Observatorio Astronómico, Universidad de los Andes, Cra. 1 No. 18A-10, Edificio H, CP 111711 Bogotá, Colombia
- ⁶¹ Department of Physics, University of Warwick, Gibbet Hill Road, Coventry, CV4 7AL, UK
- ⁶² Universidad ECCI, Cra. 19 No. 49-20, Bogotá, Colombia. Código Postal 111311, Colombia
- ⁶³ Department of Physics, The University of Texas at Dallas, Richardson, TX 75080, USA
- ⁶⁴ Scientific Computing Core, Flatiron Institute, 162 5th Avenue, New York, NY 10010, USA
- ⁶⁵ Center for Computational Astrophysics, Flatiron Institute, 162 5th Avenue, New York, NY 10010, USA
- ⁶⁶ Instituto de Ciencias del Cosmoc, (ICCUB) Universidad de Barcelona (IEEC-UB), Martí i Franquès 1, E08028 Barcelona, Spain
- ⁶⁷ Centro de Investigación Avanzada en Física Fundamental (CIAFF), Facultad de Ciencias, Universidad Autónoma de Madrid, ES-28049 Madrid, Spain
- ⁶⁸ Excellence Cluster ORIGINS, Boltzmannstrasse 2, D-85748 Garching, Germany
- ⁶⁹ University Observatory, Faculty of Physics, Ludwig-Maximilians-Universität, Scheinerstr. 1, 81677 München, Germany
- ⁷⁰ Department of Astrophysical Sciences, Princeton University, Princeton, NJ 08544, USA
- ⁷¹ Department of Astronomy, University of Florida, 211 Bryant Space Science Center, Gainesville, FL 32611, USA
- ⁷² Department of Physics, University of Michigan, Ann Arbor, MI 48109, USA
- ⁷³ Kavli Institute for Astronomy and Astrophysics at Peking University, PKU, 5 Yiheyuan Road, Haidian District, Beijing 100871, People’s Republic of China
- ⁷⁴ Department of Physics and Astronomy, University of Waterloo, 200 University Avenue W, Waterloo, ON N2L 3G1, Canada
- ⁷⁵ Aix Marseille Univ, CNRS, CNES, LAM, Marseille, France
- ⁷⁶ Department of Astronomy, The Ohio State University, 4055 McPherson Laboratory, 140 W 18th Avenue, Columbus, OH 43210, USA
- ⁷⁷ Natural Science Research Institute, University of Seoul, 163 Seoulsiripdae-ro, Dongdaemun-gu, Seoul, Republic of Korea
- ⁷⁸ Institute of Astronomy, University of Cambridge, Madingley Road, Cambridge CB3 0HA, UK
- ⁷⁹ Konkoly Observatory, CSFK, MTA Centre of Excellence, Budapest, Konkoly Thege Miklós út 15-17. H-1121, Hungary
- ⁸⁰ MTA-CSFK Lendület Large-scale Structure Research Group, H-1121 Budapest, Konkoly Thege Miklós út 15-17, Hungary
- ⁸¹ Perimeter Institute for Theoretical Physics, 31 Caroline Street North, Waterloo, ON N2L 2Y5, Canada
- ⁸² Waterloo Centre for Astrophysics, University of Waterloo, 200 University Avenue W, Waterloo, ON N2L 3G1, Canada
- ⁸³ Department of Physics and Astronomy, Sejong University, Seoul, 143-747, Republic of Korea
- ⁸⁴ Graduate Institute of Astrophysics and Department of Physics, National Taiwan University, No. 1, Sec. 4, Roosevelt Road, Taipei 10617, Taiwan
- ⁸⁵ Sorbonne Université, CNRS/IN2P3, Laboratoire de Physique Nucléaire et de Hautes Energies (LPNHE), FR-75005 Paris, France
- ⁸⁶ Department of Astronomy & Astrophysics, University of Toronto, Toronto, ON M5S 3H4, Canada
- ⁸⁷ Department of Physics, Harvard University, 17 Oxford Street, Cambridge, MA 02138, USA
- ⁸⁸ Departament de Física, Universitat Autònoma de Barcelona, 08193 Bellaterra (Barcelona), Spain
- ⁸⁹ Astrophysics Group, Department of Physics, Imperial College London, Prince Consort Road, London, SW7 2AZ, UK
- ⁹⁰ Institució Catalana de Recerca i Estudis Avançats, Passeig de Lluís Companys, 23, 08010 Barcelona, Spain
- ⁹¹ Department of Physics and Astronomy, Siena College, 515 Loudon Road, Loudonville, NY 12211, USA
- ⁹² Department of Physics and Astronomy, University of Sussex, Falmer, Brighton BN1 9QH, UK
- ⁹³ Department of Physics & Astronomy, University of Wyoming, 1000 E. University, Dept. 3905, Laramie, WY 82071, USA

- ⁹⁴ National Astronomical Observatories, Chinese Academy of Sciences, A20 Datun Road, Chaoyang District, Beijing, 100012, People's Republic of China
- ⁹⁵ Instituto Avanzado de Cosmología A.C., San Marcos 11—Atenas 202, Magdalena Contreras, 10720. Ciudad de México, México
- ⁹⁶ Department of Physics, Carnegie Mellon University, 5000 Forbes Avenue, Pittsburgh, PA 15213, USA
- ⁹⁷ Korea Astronomy and Space Science Institute, 776, Daedeokdae-ro, Yuseong-gu, Daejeon 34055, Republic of Korea
- ⁹⁸ Departament de Física Quàntica i Astrofísica, Universitat de Barcelona, Martí i Franquès 1, E08028 Barcelona, Spain
- ⁹⁹ University of California Observatories, 1156 High Street, Sana Cruz, CA 95065, USA
- ¹⁰⁰ Abastumani Astrophysical Observatory, Tbilisi, GE-0179, Georgia
- ¹⁰¹ Faculty of Natural Sciences and Medicine, Iliia State University, 0194 Tbilisi, Georgia
- ¹⁰² Space Telescope Science Institute, 3700 San Martin Drive, Baltimore, MD 21218, USA
- ¹⁰³ Department of Physics & Astronomy, Ohio University, Athens, OH 45701, USA
- ¹⁰⁴ Centre for Advanced Instrumentation, Department of Physics, Durham University, South Road, Durham DH1 3LE, UK
- ¹⁰⁵ Department of Physics & Astronomy, University of California, Los Angeles, 430 Portola Plaza, Los Angeles, CA 90095, USA
- ¹⁰⁶ Department of Physics, Bar-Ilan University Ramat-Gan 52900, Israel
- ¹⁰⁷ SUPA, School of Physics and Astronomy, University of St Andrews, St Andrews, KY16 9SS, UK
- ¹⁰⁸ Beihang University, Beijing 100191, People's Republic of China
- ¹⁰⁹ Kavli Institute for Particle Astrophysics and Cosmology, Stanford University, Menlo Park, CA 94305, USA
- ¹¹⁰ Shanghai Key Laboratory for Particle Physics and Cosmology, Shanghai Jiao Tong University, Shanghai 200240, People's Republic of China

Received 2023 July 5; revised 2024 February 8; accepted 2024 March 7; published 2024 July 5

Abstract

The Dark Energy Spectroscopic Instrument (DESI) completed its 5 month Survey Validation in 2021 May. Spectra of stellar and extragalactic targets from Survey Validation constitute the first major data sample from the DESI survey. This paper describes the public release of those spectra, the catalogs of derived properties, and the intermediate data products. In total, the public release includes good-quality spectral information from 466,447 objects targeted as part of the Milky Way Survey, 428,758 as part of the Bright Galaxy Survey, 227,318 as part of the Luminous Red Galaxy sample, 437,664 as part of the Emission Line Galaxy sample, and 76,079 as part of the Quasar sample. In addition, the release includes spectral information from 137,148 objects that expand the scope beyond the primary samples as part of a series of secondary programs. Here, we describe the spectral data, data quality, data products, Large-Scale Structure science catalogs, access to the data, and references that provide relevant background to using these spectra.

Unified Astronomy Thesaurus concepts: [Astronomy data reduction \(1861\)](#); [Observational cosmology \(1146\)](#); [Astronomy databases \(83\)](#); [Astronomy data analysis \(1858\)](#); [Astronomy software \(1855\)](#); [Surveys \(1671\)](#); [Redshift surveys \(1378\)](#)

1. Introduction

Wide-field imaging and spectroscopy enable a host of astrophysical studies that range from the largest cosmological scales to the local environment of the Milky Way. Starting in 2000, the Sloan Digital Sky Survey (SDSS; York et al. 2000) represents the largest such program. The largest public release of SDSS spectroscopic data, DR17, includes 5,580,057 optical and near-infrared (NIR) spectra passing quality cuts (Abdurro'uf et al. 2022). Data from SDSS has been used in more than 11,200 peer-reviewed publications.¹¹¹ Following the precedent of SDSS, recent releases from the Dark Energy Survey (DES; Abbott et al. 2021; Sevilla-Noarbe et al. 2021), Gaia collaboration (Gaia Collaboration et al. 2022), Hyper Suprime-Cam (HSC) Subaru Strategic Program (Aihara et al. 2022), and the Galaxy And Mass Assembly (GAMA) team (Driver et al. 2022) represent broader efforts of wide-field survey teams to provide well-calibrated data with comprehensive documentation to the public.

The Dark Energy Spectroscopic Instrument (DESI; DESI Collaboration et al. 2016a, 2016b) began science observations in 2020 December, making it the first Stage-IV (Albrecht et al. 2006) dark energy program to begin operations. DESI will obtain spectra of stars, galaxies, and quasars over

approximately 14,000 deg². Data from the Milky Way Survey (MWS) program (Cooper et al. 2023), comprised of more than 7 million spectroscopically confirmed stars, will be used to characterize the assembly history and mass profile of our Galaxy. The extragalactic spectroscopic sample, consisting of nearly 14 million bright galaxies (Bright Galaxy Survey, hereafter BGS; Hahn et al. 2022), 7.5 million luminous red galaxies (LRG; Zhou et al. 2023), 15.5 million emission line galaxies (ELG; Raichoor et al. 2023), and 3 million quasars (QSO; Chaussidon et al. 2023), will be used to explore the fundamental physics that governs the evolution of the Universe. The DESI sample size will be 10 times larger than the totality of the SDSS spectroscopic programs for extragalactic targets.

In this paper, we describe the public release of the first sample of DESI spectroscopic data, the Early Data Release (EDR). The data in this release originate from the Survey Validation (SV) of DESI (DESI Collaboration et al. 2023) that took place between 2020 December and 2021 May, prior to the start of the DESI Main Survey. The first phase of SV, “Target Selection Validation” (abbreviated SV1), was comprised of observations made to refine and validate the selection of targets for the MWS, BGS, LRG, ELG, and QSO samples (Myers et al. 2023). Compared to the DESI Main Survey, this phase used looser target selection cuts to span a larger range of observed properties and observed these targets to a higher signal-to-noise ratio (S/N). This enabled building truth samples, optimizing target selection cuts, and tuning the necessary S/N to meet the survey requirements (DESI Collaboration et al. 2023). After a brief “Operations Development” phase (SV2), DESI finished SV with the “One-Percent

¹¹¹ <http://tinyurl.com/SDSSPapers1>



Survey” (SV3), which further optimized the efficiency of observing procedures and produced samples with very high fiber assignment completeness for clustering studies over an area that is approximately 1% of the final DESI Main Survey.

This paper is organized as follows. In Section 2, we present the DESI instrument, the design of SV observations, and a brief summary of the target classes contained in this data release. A full description of target classes can be found in Appendices A and B. In Section 3, we discuss the spectral processing, data quality, and data included in this release. Next, in Section 4, we detail the creation and uses of the Large-Scale Structure (LSS) value-added catalogs (VACs) of the One-Percent Survey that accompany this release. In Section 5, we describe online access to the data and tutorials with examples of working with the data. Finally, in Section 6, we provide a brief summary of results produced with these SV data and the plans for future releases.

2. Data Acquisition

The DESI spectrographs were built to obtain spectra of roughly 40 million galaxies and quasars over a 5 yr period to study dark energy through measurements of LSS. The maps produced with these spectroscopic samples are expected to allow volume-averaged measurements of the baryon acoustic oscillation (BAO) feature at a precision better than 0.5% over each of the intervals $0.0 < z < 1.1$, $1.1 < z < 1.9$, and $1.9 < z < 3.7$. These maps will also allow percent-level precision measurements of redshift space distortions (RSD) over each interval $0.0 < z < 1.1$ and $1.1 < z < 1.9$. Here, we present an overview of the instrument design, observing strategy, phases of SV observing, and the SV samples that were used to inform the strategy to make these cosmological measurements.

2.1. Instrument Design

DESI requires a wide field of view that was made possible with a new prime focus corrector at the NOIRLab’s¹¹² 4 m Mayall telescope at Kitt Peak National Observatory in AZ. These optics allow spectroscopy over a 0.8 m diameter focal plane (Miller et al. 2023) located at the prime focus, corresponding to roughly $3^{\circ}2$ on the sky and a field of view just over 8 deg^2 . Installed in this focal plane are 5020 robotically controlled fiber positioners (Silber et al. 2023), each holding a unique fiber with a core diameter of $107 \mu\text{m} \sim 1^{\prime}5$ (C. Poppett et al. 2023, in preparation). Twenty fibers direct light to a camera to monitor the sky brightness, while the remaining 5000 fibers direct the light of a targeted object from the primary focus to one of ten spectrographs. The focal plane is constructed of 10 “petals,” with each petal of 500 science fibers mapping to a single spectrograph that measures all 500 targets simultaneously. These spectrographs have three cameras, denoted as *B* (3600–5800 Å), *R* (5760–7620 Å), and *Z* (7520–9824 Å),¹¹³ that provide a resolving power of roughly 2000 at 3600 Å, increasing to roughly 5500 at 9800 Å (P. Jelinsky et al. 2023, in preparation).

The full system has the sensitivity to measure and resolve the [OII] doublet down to fluxes of $8 \times 10^{-17} \text{ erg s}^{-1} \text{ cm}^{-2}$ in effective exposure times of 1000 s for galaxies $0.6 < z < 1.6$. Here, the effective exposure time corresponds to an exposure

time in reference conditions—zenith, dark sky, FWHM seeing of $1^{\prime}1$, and no galactic extinction (see Section 3.1.2 for a summary; and Section 4.14 of Guy et al. 2023 for details). At this effective exposure time, and accounting for increased overhead due to galactic extinction, air mass, weather, operational overheads, and engineering downtime, the DESI instrument can be used to complete a $14,000 \text{ deg}^2$ survey in 5 yr. A comprehensive description of the completed instrument can be found in DESI Collaboration et al. (2022).

2.2. Observing Strategy

DESI has five “primary” target classes (MWS, BGS, LRG, ELG, and QSO in increasing order of mean redshift), as well as many “secondary” target classes, which are generally used as filler samples for fibers that cannot reach a primary target. The observations are based upon *tiles*, which are a given pointing of the telescope combined with assignments of each fiber to a specific target for that telescope pointing. Tiles are associated with a single *survey*, or phase of the DESI operations. Tiles are further grouped within a survey by their *program* indicating the observing conditions under which they should be observed. For example, BGS and MWS targets are assigned to “bright” program tiles, while fainter ELG, LRG, and QSO targets are assigned to “dark” program tiles. The bright versus dark distinction is based upon the survey speed, or how quickly the instrument can accumulate S/N given the current observing conditions, as estimated by the exposure time calculator (ETC; D. Kirkby et al. 2023, in preparation). Bright tiles are observed when the survey speed is $2.5 \times$ worse than the reference conditions described in Section 2.1. “Backup” program tiles are used when conditions are too poor for bright tiles, $12.5 \times$ worse than reference conditions, where bright stars are targeted. Multiple programs were interleaved during each survey, selected dynamically based upon current observing conditions. During SV, some bright tiles were purposefully observed under both bright and dark conditions to provide comparison data sets for quality assurance tracking.

Each program is subdivided into one or more subprograms, called *fiberassign programs* (data column FAPRGRM). For the majority of programs, there is only one fiberassign program of the same name; however, some programs like the SV1 survey’s dark program contained multiple fiberassign programs to differentiate the various purposes of each set of tiles. More information on fiberassign programs will be described in A. Raichoor et al. (2023b, in preparation). Table 1 lists the surveys, programs, and fiberassign programs available in the EDR, with further details in Table 5 and Appendices A and B. With the exception of commissioning and specifically designed tiles in a “special” survey, each survey included dark, bright, and backup programs, while Target Selection Validation (SURVEY=sv1) also includes an “other” program for tiles dedicated to secondary targets.

DESI files typically follow the convention of uppercase column names and lowercase string values, e.g., PROGRAM=dark.¹¹⁴ In the data files, the tiles are tracked with a unique integer TILEID, and each tile is associated with specific strings for SURVEY, PROGRAM, and FAPRGRM.

Tiles overlap on the sky, enabling both greater fiber assignment completeness for dense targets such as ELGs, as well as the opportunity to observe fainter targets to higher S/N

¹¹² Formerly named the National Optical Astronomy Observatory.

¹¹³ Future DESI data releases may adjust the exact wavelength grid extracted from the data.

¹¹⁴ A notable exception is the spectral classification SPECTYPE column, which has uppercase values GALAXY, QSO, and STAR.

Table 1
Surveys, Programs, and Fiberassign Programs Available in the EDR, in Increasing Order of Specificity

SURVEY	PROGRAM	FAPRGRM
cmx	other	m33
special	dark	dark
sv1	backup	backup1
sv1	bright	bgsrms
sv1	dark	elg elgqso lrgqso lrgqso2
sv1	other	dc3r2 m31 mwclusgaldeep praesepe rosette scndcosmos scndhetdex ssv umaii unwisebluebright unwisebluefaint unwisegreen
sv2	backup	backup
sv2	bright	bright
sv2	dark	dark
sv3	backup	backup
sv3	bright	bright
sv3	dark	dark

Note. Each fiberassign program represents a choice for how targets were selected for a given observation and under what conditions a tile should be nominally observed. See Table 5 for more details on the nonstandard fiberassign programs.

by combining observations across multiple tiles, e.g., for high-redshift quasars. Each target has a unique integer TARGETID to track their observations across multiple tiles, targeting bitmasks¹¹⁵ to track the reason(s) that they were selected for observation, as detailed in Myers et al. (2023), and Appendices A and B.

A given TARGETID could be assigned to a single tile; multiple tiles of the same SURVEY and PROGRAM (such as QSO targets); or multiple tiles of different SURVEYS or PROGRAMS (such as brighter LRGs on PROGRAM=dark tiles also being selected as BGS targets on PROGRAM=bright tiles). To preserve the data uniformity within a (survey, program) combination, target selection and fiber assignments within a (survey, program) are independent of whether the target is also selected and assigned in a different (survey, program), even when this results in additional observations of the same target. Similarly, these data are also processed independently such that spectra are not coadded or fit across different surveys and programs.

2.3. SV Observations

DESI SV observations began on 2020 December 14, and nominally concluded on 2021 May 13 (see DESI Collaboration et al. 2023; and Section 2.3 of Myers et al. 2023 for further details). An additional 22 SV-designed tiles were observed on 5 nights after the start of the Main Survey on 2021 May 14; with the final observations taking place on 2021 June 10. The additional tiles were observed to improve the completeness of the

¹¹⁵ A bitmask is an integer generated from setting multiple predefined bits to either 0 or 1 to indicate false or true respectively. The integer is then computed as $\sum_i 2^i b_i$, with b_i being 0 or 1 and i being the bit number. For more information, see <https://github.com/desihub/desitarget/blob/2.5.0/doc/nb/target-selection-bits-and-bitmasks.ipynb>.

One-Percent Survey areas, and are included in the EDR. Table 2 lists the number of nights, tiles, exposures, effective exposure times, and area covered by tiles for each survey included in the EDR. Figure 1 shows the number of unique tiles per night for each of the three phases of SV. Although there are distinct boundaries for when each survey began, there is an overlap in dates as incomplete tiles from a previous survey were sometimes completed after the start of the next survey. A given tile can be observed on multiple nights, and thus contributes to multiple bins, but if it was observed multiple times on a single night, it is only counted once for that night in Figure 1.

The covered area listed in Table 2 is simply the unique area that is overlapped by any tile in that survey, while not double-counting the area covered by more than one tile. This gives a sense of the scope of the SV observations, but note that these areas are larger than the true effective area due to gaps in the focal plane coverage, disabled or broken hardware, and target assignment priorities, as will be discussed in Section 4.1.

2.3.1. Target Selection Validation

The first phase of SV observations, Target Selection Validation, optimized the DESI survey strategy and target selection algorithms. Target Selection Validation used SURVEY=sv1.¹¹⁶

A key product of the observations for Target Selection Validation was the calibration of effective exposure times. As stated previously, effective exposure times account for varying throughput and background and provide a standard metric of exposure depth that corresponds to an exposure time at air mass 1, zero galactic extinction, 1'' FWHM seeing, and zenith dark sky. DESI uses two effective times, EFFTIME_ETC and EFFTIME_SPEC, which are used for determining when to stop an exposure of a tile at the telescope and determining when a tile has been observed enough to meet survey specifications, respectively. EFFTIME_SPEC is based on the offline spectroscopic data and will be described in Section 3.1.2. EFFTIME_ETC is based on active monitoring of the sky conditions and the location on the sky (D. Kirkby et al. 2023, in preparation). The sky brightness is monitored with sky monitor fibers along the outer rim of the focal plane, which send light to a dedicated imaging system that is read out regularly during the spectroscopic exposure. These are independent of the sky targets used in the spectroscopic data processing. Sky targets used in the data processing are assigned to robotic positioners on the focal plane along with the other target types, and their light is acquired using one of the DESI spectrographs. The image quality and sky transparency are derived from the guide focus assembly system. For more information about these components, see DESI Collaboration et al. (2022). For the Main Survey, a calibrated algorithm called the ETC determines when the exposure is estimated to be complete (D. Kirkby et al. 2023, in preparation). For SV1, there was no calibration of sky conditions to effective time, so a power law $t_{\text{exp}} = t_0 X^{1.25}$ was used. Here, X is the air mass, t_0 is the nominal time, and the relation is empirically derived from BOSS/eBOSS data. These data were used to calibrate the EFFTIME_SPEC of the offline pipeline, which in turn was used to calibrate EFFTIME_ETC.

During Target Selection Validation, requested effective exposure times were increased by approximately a factor of 4

¹¹⁶ We use capital "SV1" as the acronym in text descriptions and column names, but lowercase sv1 for values in data files, as well as directory and file names on disk.

Table 2
Number of Nights, Tiles, Exposures, Effective Exposure Time, and Approximate Area Covered by Tiles for Surveys Included in the Early Data Release

Survey	Description	Nights	Tiles	Exposures	Effective Hours (hr)	Covered Area (deg ²)
cmx	Commissioning	1	1	4	0.9	8
special	Test Tiles	2	16	21	0.3	75
sv1	Target Selection Validation	73	175	1568	137.5	1040
sv1	Secondary Tiles	18	13	105	37.9	67
sv2	Operations Development	10	39	72	6.4	102
sv3	One-Percent Survey	38	488	710	102.2	197

Note. SURVEY=sv1 includes both Target Selection Validation tiles and tiles dedicated to secondary targets. The area covered by tiles is larger than the true effective area available to targets due to bright star exclusions, focal plane geometry, hardware configuration, and higher-priority targets blocking lower-priority targets.

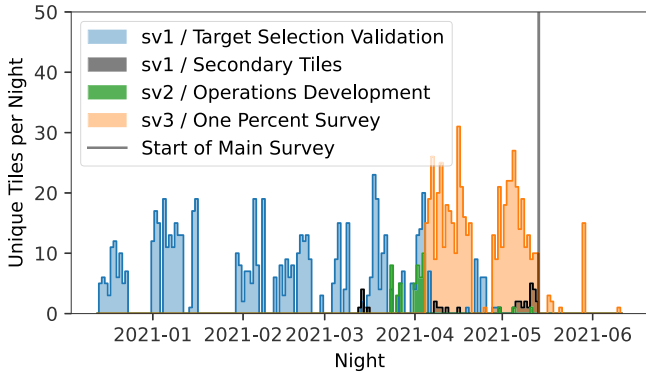


Figure 1. The number of unique tiles per night observed during Survey Validation. The same tile can be observed on multiple nights.

relative to the survey design to provide high S/N spectra. These data were typically collected over four different nights to allow tests of redshift classification using subsets of data acquired under different observing conditions.

In addition to the four-epoch strategy, Target Selection Validation observations included even deeper exposures of some tiles. The deepest tiles for each of the five primary DESI target classes (MWS, BGS, LRG, ELG, and QSO) are listed in Table 3. These tiles contain spectra that are much higher S/N than most data expected from the program and can therefore be used for unique studies of stellar, galaxy, or quasar astrophysics. A subset of these deep tiles (including tiles not listed in Table 3) also have visual inspections; see Section 3.3.6.

In total, 137.5 effective hr during SV were dedicated to 175 Target Selection Validation (SV1) tiles.

2.3.2. Operations Development

After Target Selection Validation, SV continued with an Operations Development phase with SURVEY=sv2, in preparation for the One-Percent Survey. The purpose of these observations was to validate the end-to-end operational procedures needed to schedule observations of targets in a tile, process those observations, identify successfully acquired redshifts, and determine which targets were completed or should be scheduled for new observations in additional overlapping tiles. A major focus of this phase was to establish the “Merged Target List” (MTLs) ledgers (see Section 5 of Schlafly et al. 2023), which track the observational state and redshift of each target and determine whether a target requires further observations. In total, 6.4 effective hr during SV were dedicated to 39 Operations Development tiles.

Table 3
The Five Deepest Tiles for the Five Primary Target Classes in DESI

TILEID	Targets	Effective Time (hr)
80613	MWS, BGS	0.85
80736	MWS	0.95
80607	LRG, QSO	2.6
80608	ELG	4.2
80711	ELG, QSO	6.7

2.3.3. One-Percent Survey

The final phase of the SV program, the One-Percent Survey, (SURVEY=sv3) was used to validate final operational procedures and compile extensive samples of sources that could be used for clustering studies. The One-Percent Survey was conducted over the period 2021 April 5–June 10, with the vast majority of observations occurring on or before 2021 May 13. In total, the One-Percent Survey covered 20 fields, each with a “rosette” pattern of ~ 10 – 11 overlapping tiles in bright time and ~ 12 – 13 tiles in dark time whose centers were offset in a circle of radius $0''.12$ from the field center. The overlapping tiles provided high fiber assignment completeness over an area of 6.48 deg^2 ; within which more than 95% of MWS and ELG targets and more than 99% of BGS, LRG, and QSO targets received fibers. Targets covering an additional $\sim 2 \text{ deg}^2$ were observed with fewer visits and a lower completeness in fiber assignment because of fewer overlapping tiles in the outer edge of the rosette of each field and the hole in the center of the DESI focal plane. Figure 4 shows the tile coverage of one bright-time rosette. LSS catalogs were created covering the entire area and are detailed in Section 4.

One-Percent Survey rosettes were selected to cover major data sets from other surveys, including the Cosmic Evolution Survey (COSMOS; Scoville et al. 2007), HSC (Aihara et al. 2018a), DES (Dark Energy Survey Collaboration et al. 2016) deep fields, GAMA (Driver et al. 2011), Great Observatories Origins Deep Survey (GOODS; Dickinson & Giavalisco 2003), and anticipated deep fields from future Legacy Survey of Space and Time (LSST; Ivezić et al. 2019) and Euclid (Euclid Collaboration et al. 2022) observations. These are summarized in Table 4. In total, 102.2 effective hr during SV were dedicated to 488 tiles in the One-Percent Survey (SV3).

2.3.4. Other SV Observations

In addition to Target Selection Validation, Operations Development, and One-Percent Survey tiles, SV observed additional tiles dedicated to secondary targets proposed by

Table 4
Selected DESI Tiles with Visual Inspections (VI) or Overlapping with Data Sets from Other Surveys

Set	R.A.	Decl.	TILEID(s)	Other Surveys
VI LRG+QSO	36.448	−4.601	80605	XMM-LSS
VI ELG	36.448	−4.501	80606	XMM-LSS
VI LRG+QSO	106.74	56.100	80607	Lynx
VI ELG	106.74	56.200	80608	Lynx
VI BGS	106.74	56.100	80613	Lynx
VI LRG+QSO	150.12	2.206	80609	COSMOS
VI ELG	150.12	2.306	80610	COSMOS
SV3 R0	150.10	2.182	1–21, 23–24, 442	COSMOS, DES deep, LSST deep, CFHTLS-D2 HSC ultradeep, VVDS-F10, DESI SV1 80871
SV3 R1	179.60	0.000	28–53, 445	GAMA G12, KiDS-N, DESI SV1 80662
SV3 R2	183.10	0.000	55–79, 448	GAMA G12, KiDS-N
SV3 R3	189.90	61.800	82–107, 451–452	GOODS-North
SV3 R4	194.75	28.200	109–129, 131–133, 454	Coma cluster, DESI SV1 80707
SV3 R5	210.00	5.000	136–156, 158, 457	VVDS-F14
SV3 R6	215.50	52.500	163–187, 460	DEEP2, CFHTLS-D3/W3, DESI SV1 80711 & 80712
SV3 R7	217.80	34.400	190–215, 463	Bootes NDWFS/AGES
SV3 R8	216.30	−0.600	217–238, 466	GAMA G15, HSC DR2, KiDS-N
SV3 R9	219.80	−0.600	244–265, 469	GAMA G15, HSC DR2, KiDS-N
SV3 R10	218.05	2.430	271–291, 472	GAMA G15, HSC DR2, KiDS-N
SV3 R11	242.75	54.980	298–321, 475	ELAIS N1, HSC deep field, DESI SV1 80865–80867
SV3 R12	241.05	43.450	325–347, 478	HSC DR2
SV3 R13	245.88	43.450	352–375, 433	HSC DR2
SV3 R14	252.50	34.500	379–402, 436–437	XDEEP2
SV3 R15	269.73	66.020	406–429, 439	Ecliptic pole, Euclid deep field
SV3 R16	194.75	24.700	481–491, 495–504, 506	Coma cluster outskirts
SV3 R17	212.80	−0.600	511–521, 525–534	GAMA G15, HSC DR2, KiDS-N
SV3 R18	269.73	62.520	541–551, 555–565	Near ecliptic pole
SV3 R19	236.10	43.450	571–581, 585–596	HSC DR2

Note. “SV3 R n ” denotes rosette number n from the One-Percent Survey, with R.A. and decl. referring to the center of the Rosette rather than the center of an individual tile.

members of the DESI collaboration to extend the scientific reach of this EDR. These tiles are listed in Table 5, with the target selection bits described in Appendix B. Secondary targets were also used as low-priority filler targets on other tiles, to be used in cases when an available fiber could not reach a primary target and was not needed for calibration targets (standard stars or sky locations). DESI observed 37.9 effective hr of these 13 dedicated secondary target tiles.

EDR includes one commissioning tile (TILEID=80615, SURVEY=cmx) covering M33 that was observed during the SV time period. It also includes sixteen SURVEY=special tiles used for fiber assignment testing (TILEIDs 81100–81115). Although these special tiles used dark-time targets (LRG, ELG, QSO), most were observed for less than 1 minute of effective exposure time and have very low spectroscopic S/N. Only tiles 81100 and 81112 will be retained in future data releases, as they have effective exposure times greater than 2 minutes and may provide sufficient signal for brighter targets. In total, 0.9 effective hr of exposure time were dedicated to commissioning observations; and 0.3 effective hr were dedicated to SURVEY=special observations.

2.4. SV Target Samples

DESI primary targets (MWS, BGS, LRG, ELG, and QSO) are selected from Data Release 9 of the Legacy Imaging Surveys (LS/DR9; Zou et al. 2017; Dey et al. 2019; D. J. Schlegel et al. 2023, in preparation), while secondary targets could come from LS/DR9 or other sources. Targets identified for spectroscopic observations are recorded from the imaging

data and documented for downstream redshift and clustering catalogs (see Myers et al. 2023; and Appendix A). The target selections used for the SV data in EDR are described in Allende Prieto et al. (2020) for MWS, Ruiz-Macias et al. (2020) for BGS, Zhou et al. (2020) for LRG, Raichoor et al. (2020) for ELG, and Yèche et al. (2020) for QSO. Secondary targeting programs are briefly summarized in Appendix B and references therein. These algorithms were updated based on analysis of the EDR data resulting in the DESI Main Survey final target selections documented for the MWS program in Cooper et al. (2023), BGS in Hahn et al. (2022), LRG in Zhou et al. (2023), ELG in Raichoor et al. (2023), and QSO in Chaussidon et al. (2023).

The EDR consists of 2,847,435 spectra unique to a given survey and program, when including science targets, standard stars, and sky fiber spectra. Of those, 2,757,937 are unique locations on the sky. Selecting only spectra that do not have hardware or observing flags yields 2,183,282 unique spectra. Further subselecting to science targets, the EDR contains 1,852,883 unique science spectra free of hardware (e.g., fiber, CCD pixels, positioner) flags and observing (e.g., poor positioning, low effective exposure time) flags. Finally, restricting to those that are free of redshift fitting (e.g., a bad fit) flags results in 1,712,004 unique, “good” target spectra and redshifts; including 1,125,635 GALAXY, 90,241 QSO, and 496,128 STAR spectral classifications. For more details about these selection choices, see Section 3.2, and for more information on the redshift classification, see Section 3.1.3 and S. J. Bailey et al. (2023, in preparation). For the selection

Table 5
Fiberassign Programs, Descriptions, TILEID Ranges, Effective Exposure Time, and Targeting Bits for All Tiles Dedicated to Secondary Targets

FAPRGRM	Description	TILEID(s) (hr)	Effective Hours	Targeting Bit-names
m33	M33	80615	0.94	M33_{H2PN, GC, QSO, M33cen, M33out}
...	SV0_{WD, QSO, LRG, ELG}
m31	M31	80715	0.50	M31_KNOWN, M31_QSO, M31_STAR
rosette	Rosette Nebula	80718	0.01	All secondary target bits
praesepe	Praesepe (Beehive cluster)	80719	0.03	All secondary target bits except LOW_Z
umaii	Ursa Major II dwarf galaxy	80720	0.03	MWS_{ANY, CALIB, MAIN_CLUSTER_SV, RRLYR}
...	BHB, BACKUP_CALIB
ssv	Stellar survey validation	80721–80738	0.37	MWS_{NEARBY, MAIN_BROAD, MAIN_FAINT}
...	MWS_{WD, BHB, CALIB}
...	MWS_{MAIN_CLUSTER_SV, RRLYR}
...	WD_{BINARIES_BRIGHT, BINARIES_DARK}
...	BACKUP_{FAINT, VERY_FAINT, CALIB}
mwclusgaldeep	Star clusters and dwarf galaxies	80862–80863	2.38	MWS_{MAIN_BROAD, NEARBY, MAIN_FAINT}
...	MWS_{WD, BHB, CLUS_GAL_DEEP}
...	WD_BINARIES_DARK
unwisegreen	n(z) calibration for CMB lensing cross-correlations	80865	7.85	UNWISE_GREEN_II_{3700, II_3800, 3900, 4000}
...	UNWISE_BLUE_FAINT_II
...	LOW_MASS_AGN, LOW_Z
unwisebluebright	n(z) calibration for CMB lensing cross-correlations	80866	0.68	UNWISE_BLUE_BRIGHT_II
unwisebluefaint	n(z) calibration for CMB lensing cross-correlations	80867	1.79	UNWISE_BLUE_FAINT_II
scndhetdex	HETDEX follow-up and Ly- α tomography	80869–80870	5.33	LBG_TOMOG_W3, HETDEX_{HP, MAIN}
...	LOW_MASS_AGN, LOW_Z
scndcosmos	Various samples	80871–80872	5.22	DESILBG_{TMG_FINAL, BXU_FINAL, G_FINAL}
...	QSO, ISM_CGM_QGP, HSC_HI_Z_SNE
dc3r2	Photo-z calibration	80971–80975	1.40	DC3R2_GAMA and all DARK primary targets as filler

Note. See Appendix B for a description of the targeting bits for each program. Most of these fiberassign programs targeted specific secondary program objects, while “rosette” and “praesepe” used all available secondary targets, and “dc3r2” used dark-time primary targets as filler targets after assigning the desired secondary targets.

Table 6
The Number of “Good” Spectra Obtained in Each Phase of SV, Along with Details for Dedicated Pointings (Special) and Commissioning (cmx)

SURVEY	N_{BGS}	N_{ELG}	N_{LRG}	N_{QSO}	N_{STAR}	N_{SCND}
cmx	247	761	1037	275	468	0
sv1	134,419	111,692	66,161	29,839	163,254	60,430
sv2	46,628	12,308	22,151	11,032	10,506	0
sv3	253,915	312,790	137,317	34,173	295,232	75,947
special	925	3866	3588	3045	867	3482
Total	428,758	437,664	227,318	76,079	466,447	137,148

Note. Here, each target class is selected with the bitmasks for that tracer in that survey, and “good” refers to science targets that have no Redrock ZWARN bits set and whose best-fitting templates are consistent with the tracer (GALAXY for BGS, ELG, and LRG targets; QSO for QSO targets, and STAR for MWS). Each row counts unique targets, but since some targets were observed under multiple surveys, the total number of unique targets is less than the sum of the rows.

criteria used for the DESI LSS catalogs, which are generally more restrictive, see Section 4.

Table 6 summarizes the number of good objects per target class in each survey as well as in the total EDR sample, with the additional restriction that the target was classified as the intended target selection type—GALAXY for BGS, ELG, and LRG samples; QSO for QSO samples; and STAR for MWS samples. Note that the sum of a column or row may not be equal to the total due to individual objects being observed in multiple surveys or individual objects being selected for multiple target classes. The numbers as a function of redshift for the full EDR sample are shown in Figure 2. This includes both primary targets that were classified as their targeted type (colored histograms), as well as confident classifications of any

targets (primary or secondary) regardless of their expected target type (gray histograms). For example, the bump at $z < 0.5$ in the gray histogram for QSO classifications comes primarily from BGS targets that were either quasars or active galactic nucleus (AGN)-like galaxies that Redrock classified as QSO instead of galaxies. Although they may be valid redshifts, these are not included in Table 6.

Figure 3 shows the density of good target redshifts on the sky for each of the three primary phases of SV — Target Selection Validation (sv1, blue), Operations Development (sv2, green), and the One-Percent Survey (sv3, orange). Target Selection Validation has many tiles distributed over the sky, while the One-Percent Survey has a larger number of tiles over a smaller area, leading to much higher good target densities

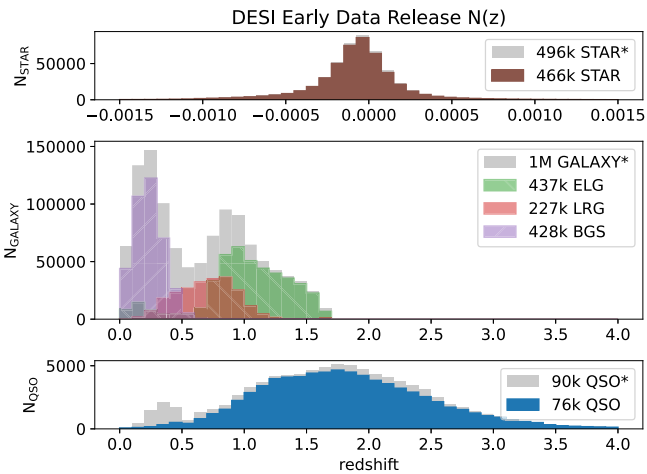


Figure 2. The number of good, unique target redshifts as a function of redshift for each tracer type as defined in Section 3.2. The reddish-brown distribution is for objects targeted to be a star and classified by Redrock to be `SPECTYPE==STAR`. The purple, green, and red histograms show objects targeted as BGS, ELG, and LRG respectively, and classified as a `GALAXY`. The blue distribution shows objects targeted as a QSO and classified as a `QSO`. The gray distributions depict all objects that were classified by Redrock as a `STAR`, `GALAXY`, or `QSO` for the top, middle, and bottom panels respectively. (*) Note that the gray differs from the colored histograms because of secondary targets and other target types that were classified to a different category (e.g., a QSO target that was classified as a `STAR`). Also, note that an object can be targeted by two galaxy target classes, and such objects will appear in both distributions.

(and thus much higher target completeness for those patches of sky) for the One-Percent Survey.

Metadata about the targets included in each file are recorded in the `FIBERMAP` header/data unit extension of the `FITS`¹¹⁷ files in the EDR. These include the input photometry used for target selection,¹¹⁸ target selection bitmasks recording, which target classes each target was selected for, and information about which fiber each target was assigned to and how accurately that fiber was positioned. This information is also propagated into the final redshift catalogs. The target selection bitmasks for each of the surveys included in the EDR are described in Appendix A, with further details in Section 2.4 of Myers et al. (2023).

3. Data Reduction and Data Products

3.1. Data Reduction

3.1.1. Spectroscopic Calibration and Reduction

The spectroscopic data reduction for DESI is performed with a newly developed, Python-based pipeline. The EDR is a reprocessing of the raw data performed using a tagged version of the pipeline code.¹¹⁹ The directory structure and filenames retain the internal name of the release, `fujii`, named after the mountain and signifying the sixth internal release of data. A detailed description of the DESI pipeline can be found in Guy et al. (2023); here, we provide a short summary.

Spectroscopic data are transferred from the telescope at Kitt Peak in nearly real time to the National Energy Research Scientific Computing Center (NERSC) for processing and

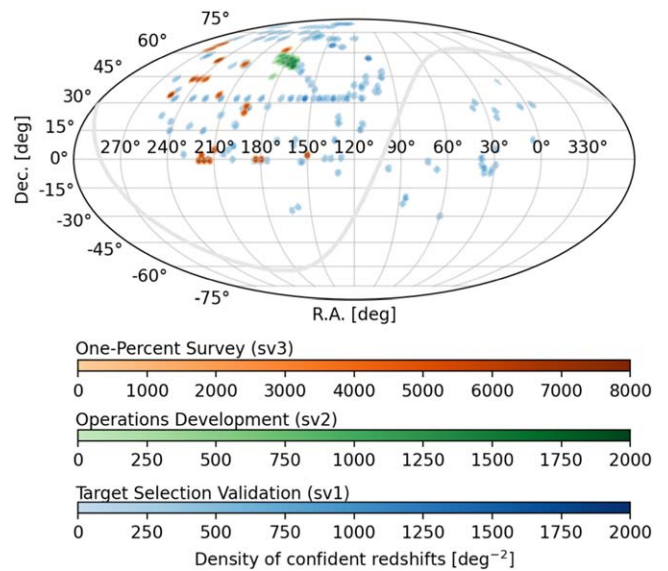


Figure 3. The density of good, unique target redshifts on the sky, split by the three primary phases of Survey Validation — Target Selection Validation (sv1, blue), Operations Development (sv2, green), and the One-Percent Survey (sv3, orange). Note that the orange One-Percent Survey colormap goes to 4× higher density than the others, reflecting the much higher density of targets in the One-Percent Survey rosettes of overlapping tiles.

archiving. Each night, the data are processed from raw images to redshifts such that tiles identified as being observed to full-depth can be approved as complete, and the targets entered into the MTL ledgers can be approved as being observed (see Section 5 of Schlafly et al. 2023). This allows for subsequent overlapping tiles to be designed and observed in the same region of sky with new targets (and repeated high-redshift QSO targets for those identified as Ly α forest sources).

The DESI instrument consists of ten petals of 500 fibers each that send light to 10 corresponding spectrographs. Each spectrograph has three arms: blue, red, and NIR (denoted *B*, *R*, and *Z* in the data files). In its nominal configuration, the instrument generates 10 4096 × 4096 pixel blue images and 20 4114 × 4128 pixel red and NIR images, with each containing the data for 500 fibers in one of the three wavelength ranges. In the afternoon before each night of observation, calibration data are acquired and processed so that they can be applied to the scientific data taken throughout the night. Twenty-five 0 s *zero* exposures are taken with the shutter closed to generate a master bias for the night. This bias is removed from all other calibrations and science exposures for the night. Next, a 300 s *dark* exposure, again with the shutters closed, is taken to identify new bad columns or pixels in the CCD and to test the nightly master bias against a template bias to determine which gives the smallest residuals in the processed image. If the template produces smaller residuals, then it is used instead of the master bias derived on that night.

Five *arc* exposures are then taken with Ar, Cd, Hg, Kr, Ne, and Xe arc lamps. These are used for an initial wavelength calibration for each fiber throughout the night, in addition to generating a full 2D point-spread function (PSF) model for each image to be used for extracting the spectral signal from the 2D data using an implementation of the spectroperfectionism algorithm described in Bolton & Schlegel (2010). These exposures are also used to determine the fiber traces representing the 2D extent of each fiber on the image. Finally, four sets of three *flat* exposures are taken with LED lamps on a

¹¹⁷ https://fits.gsfc.nasa.gov/fits_standard.html

¹¹⁸ Targets that were secondary only and not matched to LS/DR9 do not have photometry included.

¹¹⁹ <https://github.com/desihub/desispec/releases/tag/0.51.13>

white dome screen and combined to generate a per-fiber flat field correction that is applied to the subsequent science exposures on the night.

Science data taken throughout the night are first preprocessed to convert analog digital units into electron counts, identify and mask cosmic rays and bad pixels, remove detector bias and correct for dark current, apply a CCD flat field correction, and estimate the per-pixel variance in the image. Next, the wavelength solution derived from the *arc* exposures is refined using sky lines, small trace shifts are identified, and a new 2D PSF model is generated for each exposure. Counts for each fiber are then extracted, along with estimates of the variance and the resolution matrix that encapsulates the mapping between the 2D model and the 1D, uncorrelated, linear wavelength binned output spectra. The output spectra are then flat fielded using the per-fiber flat field vectors derived from the *flat* exposures. The sky is then removed using fibers explicitly positioned to empty sky locations. These sky fibers are combined to create one high-resolution sky model for each spectrograph, before using the resolution matrix of each fiber to subtract the sky.

After sky subtraction, main-sequence F stars are used for flux calibration. The selected standard star fiber spectra are fit to all three cameras simultaneously using theoretical models for a wide range of stellar effective temperature (T_{eff}), surface gravity ($\log_{10} g$), and iron abundance ([Fe/H]). The resulting fits can be used to derive the throughput of the instrument by relating the measured counts to the expected flux from photometry, which enables the generation of calibration vectors for all fibers on the petal to convert counts into fluxes in units of $10^{-17} \text{ erg s}^{-1} \text{ cm}^{-2} \text{ \AA}^{-1}$. To improve S/N, if multiple exposures of a single tile are observed on a night, then all of the exposures are used to jointly model standard stars, before each exposure is used independently to generate a calibration vector for that exposure. The per-star calibration is used to derive the observed flux compared to the expected flux from imaging photometry, and 3σ outliers are rejected compared to the scatter observed for all standard stars across all spectrographs. The final calibration vector per camera is an average over the remaining standard stars on that camera. Finally, a crosstalk correction is applied to account for the fact that the 2D PSF of each fiber extends into the region of its neighbors before writing out the per-exposure per-fiber calibrated fluxes and variances.

During SV1, tiles were allocated with 80 sky fibers and a goal of 20 standard stars per petal. Using these data, tests were performed to identify the minimum number of sky fibers and standard stars that could be used per petal before degradation in sky subtraction or flux calibration would be observed. It was shown that as few as 20 sky fibers per petal and 10 standard stars per petal were sufficient to maintain ELG redshift efficiency, which was used as a proxy for measuring the impact of sky subtraction residuals on the resulting spectra. For SV3 and the Main Survey, DESI requires a minimum of 40 sky fibers and 10 standard star fibers per petal to be conservative.

DESI tiles are observed to have a roughly equal effective exposure time rather than raw exposure time. This results in varying raw exposure times and a varying number of exposures acquired for a given tile. For the EDR, the median number of exposures for a tile is 1, with a mean of ~ 3.4 , and a maximum of 30 for deep SV1 BGS tile 80613.

3.1.2. Spectroscopic Effective Exposure Time

The ETC provides a real-time estimated effective exposure time to determine when to end the observations of a given tile, using information available during an exposure. However, a more ideal quantity would be an effective time that incorporates the instrumental effects on the spectra themselves and how a particular target class might be impacted by such effects. `EFFTIME_SPEC`, which is derived from the spectroscopic data themselves each night as the data are acquired, was designed to incorporate these features. This quantity is what is used by survey operations to determine if observations of a tile have achieved enough effective time to be marked as complete for the designated `PROGRAM`.

The spectroscopic effective time estimate is detailed in Section 4.14 of Guy et al. (2023). First, a template S/N squared (TSNR^2) is defined as the mean of the squared S/N for an ensemble of templates over a representative redshift range, which incorporates instrument and observational quantities such as fiber aperture losses, detector read noise, and sky residuals. Finally, the mean TSNR^2 value for all fibers is multiplied by a constant to get the `EFFTIME_SPEC` for the exposure. Each tracer class has a different morphology and redshift range, so this is done for each separately, with each target class having a different constant of proportionality. The constants are empirically fit to equal the actual exposure time when observing in nominal conditions at zenith with a dark sky, ideal transparency, no galactic extinction, and median seeing of $1''.1$. This is done for all target classes, but the reported `EFFTIME_SPEC` for dark time is based on the LRG value, while the bright-time `EFFTIME_SPEC` is based on the BGS value.

3.1.3. Redshift Fitting and Classifications

Spectral classifications and redshifts are measured using the Redrock software package¹²⁰ (S. J. Bailey et al. 2023, in preparation). Redrock performs a χ^2 versus redshift scan, fitting a set of principal component analysis (PCA) templates to every target at every redshift. The fit with the lowest χ^2 determines the spectral classification (`SPECTYPE=GALAXY`, `QSO`, or `STAR` for DESI) and redshift. Each set of templates is fit on all spectra regardless of target selection type; including standard stars, sky-subtracted sky fibers, and spectra from nonfunctioning positioners that were not pointing at any known target. This procedure is similar to the method used in SDSS/BOSS (Bolton et al. 2012), with improvements to the underlying PCA templates, more exact error propagation, and more detailed modeling of the per-wavelength per-fiber spectral resolution. Although Redrock was originally developed for DESI, it was previously used by eBOSS for their final cosmology analyses (Ross et al. 2020).

The primary outputs from Redrock are the redshift (Z), redshift uncertainty (`ZERR`), spectral classification (`SPECTYPE`), a warning bitmask (`ZWARN`), the coefficients for the linear combination of the best-fitting templates (`COEFF`), the χ^2 of the fit (`CHI2`), and the value $\Delta\chi^2$ (`DELTACHI2`) giving the difference between the best-fit χ^2 and that of the second best fit. Larger values of `DELTACHI2` represent greater statistical confidence that the best fit is correct.

¹²⁰ <https://github.com/desihub/redrock/releases/tag/0.15.4>

In addition to classifications and redshifts, Redrock includes a per-object ZWARN bitmask indicating if there are any known problems with the data or the fit. ZWARN==0 means that there are no known problems, and nonzero values encode the reasons for possible problems. The meaning of the individual bits are documented in the Redrock code at <https://github.com/desihub/redrock/blob/0.15.4/py/redrock/zwarning.py#L14> and further described in S. J. Bailey et al. (2023, in preparation). Some bits record problems with the input spectrum, e.g., that all flux values were masked, while other bits record problems with the Redrock fit itself, e.g., a failed parabola fit to the χ^2 versus z minimum. Most analyses should require ZWARN==0 to obtain good-quality results, which implicitly include the requirement that DELTACHI2 > 9. To obtain a purer sample of more confident redshifts, some analyses may place a higher cut on DELTACHI2.

3.1.4. Post Redshift Value-added Processing

After the redshift fitting, three additional steps were included in the pipeline to postprocess the data and derive value-added quantities such as line identifications, line flux estimates, refined redshift fits, and further quasar classifications.

In addition to the Redrock results, emlinefit provides simple fits of the major galaxy emission lines. The approach is purposefully simple; a more refined approach is performed with, e.g., FastSpecfit.¹²¹ The primary motivation is to fit the [O II] doublet, and use it to identify reliable redshift measurements for ELG spectra (see Section 4.2.1 and Equation (2)). For convenience, we also provide fits for the [O III] doublet ($\lambda\lambda$ 4960, 5007 Å), and for the H α , H β , H γ , and H δ lines. All lines are computed for all spectra. However, detailed studies should be performed prior to using quantities other than [O II], or [O II] on non-ELG targets, to assess their accuracy. The fits are simple Gaussian fits at the expected position based on the Redrock best-fit results; the fitted flux is not forced to be positive, so negative values can be reported. The continuum is estimated from the wavelengths 200 Å (in rest-frame) around the emission line (bluewards for the [O II] doublet). For the [O II] doublet, the line ratio is left free during the fit; for the [O III] doublet, it is fixed. For more details, see Section 7 of Raichoor et al. (2023).

To improve the classification and the redshift determination for quasars, we also provide results from two additional codes: an Mg II broadband fitter and a neural network classifier, QuasarNET (Busca & Balland 2018; Farr et al. 2020). The Mg II fitter aims to classify spectra that exhibit a broad Mg II emission line as QSO. The algorithm determines the width of the Mg II emission by fitting a Gaussian in a 250 Å window (observer-frame) centered at the position of the Mg II line given by the redshift identified by Redrock. For the QSO classification, the Mg II emission line is considered broad if the improvement of χ^2 is better than 16, the width of the Gaussian is greater than 10 Å, and the significance of the amplitude of the Gaussian is greater than 3.

Additionally, we run QuasarNET on all the targets. QuasarNET is a deep convolutional neural network classifier designed explicitly to identify quasars and their redshifts. The input power spectrum is reduced by four layers of convolutions and is then passed to a fifth, fully connected layer before feeding into six line finder units: one for Ly α , C IV, C II, Mg II,

H α , and H β . Each line finder unit consists of a fully connected layer trained to identify a particular emission line. The output of each unit is a confidence level (between 0 and 1) to have found the desired line and the redshift at which it was found. The DESI LSS analyses require at least one emission line to have a confidence level above 0.95 for a spectrum to be considered a QSO. For each target identified by QuasarNET to be a QSO, Redrock is rerun using only QSO templates and a tophat redshift prior of ± 0.05 to determine the final redshift.

3.2. Suggested Quality Cuts

The choice of a “good” redshift is subjective and depends on the individual science case in question. In this paper, unless stated differently, we have elected to restrict to spectra with no hardware, observing, or redshift fitting flags (ZWARN==0). This is our generic recommendation, where some may choose to relax restrictions for specific bits if an analysis is robust to the implications of including such data, and some may choose to use additional selection criteria such as a cut on DELTACHI2 or, e.g., TSNR2_LRG. The LSS analyses within DESI use cuts that are generally more stringent than this, as outlined in Section 4.2.2. More details for each target class are available in the references cited in that section.

A less strict criterion would be to restrict based on the coadded spectrum’s fiberstatus, COADD_FIBERSTATUS, which encapsulates hardware and observing issues for all input data for that spectrum, but does not depend on redshift fitting. The bits are defined in the desispec.maskbits code.¹²² Note that ZWARN includes a bit that is false if COADD_FIBERSTATUS equals 0 or 8, where 0 signifies no issues, and $2^3 = 8$ corresponds to a positioner that had a restricted range but could still reach the target location. Therefore, selecting ZWARN==0 implies selecting COADD_FIBERSTATUS \in [0, 8] in addition to the redshift fitting flags.

3.3. Data Products

Full details of the directory organization and file formats in the EDR are given in the DESI data model at <https://desidatamodel.readthedocs.io>. The directory structure is summarized in Table 7. The following subsections provide a conceptual overview of the structure of the available data, starting from the root directory of the EDR; see Section 5 for methods to access these data.

3.3.1. Spectroscopic Data Processing Runs

Production data processing runs are alphabetically named after mountains and contained under spectro/redux/. Each production run uses a defined set of input data processed with a fixed set of tagged software. The EDR contains a single production named “Fuji,” available under spectro/redux/fuji/. Future data releases will contain one or more production runs, differing by the input raw data, the software tags used, or both.

In the top-level production directory, spectro/redux/fuji/tiles-fuji.fits contains a catalog of all DESI tiles included in Fuji. This can be used for a quick assessment of the footprint of the available DESI data and to filter available tiles by SURVEY and PROGRAM. Since tiles may be observed

¹²¹ <https://fastspecfit.readthedocs.io/en/latest/>

¹²² <https://github.com/desihub/desispec/blob/0.51.13/py/desispec/maskbits.py#L55>

Table 7
Summary of the Directory Structure of Data Available in the EDR

Directory	Description
<code>spectro/data/</code>	Raw data
<code>spectro/redux/fuji/</code>	Processed data
<code>healpix/</code>	Spectra, classifications, and redshifts grouped by HEALPix
<code>tiles/</code>	Spectra, classifications, and redshifts grouped by tile
<code>zcatalog/</code>	Combined redshift catalogs
<code>exposures/</code>	Intermediate processing files per exposure
<code>survey/</code>	Survey operations bookkeeping
<code>target/catalogs/</code>	Input target catalogs, same as “Early Target Selection” release
<code>target/fiberassign/</code>	Assignments of targets to fibers per tile
<code>vac/edr/</code>	Value-added catalogs contributed by the DESI science collaboration

Note. See <https://desidatamodel.readthedocs.io> for more details including subdirectory structure underneath these directories, individual file formats, and additional directories with pipeline inputs such as calibration files.

on multiple exposures spanning multiple nights, more detailed per-exposure information is available in `exposures-fuji.fits` if needed for time-domain studies or systematics comparisons of data on different nights.

3.3.2. Spectra, Coadds, Classifications, and Redshifts

Spectra, coadditions (coadds) of those spectra, and classifications and redshifts fit to those coadds are available under two broad groups: per tile, and full-depth. Tile-based spectra under `spectro/redux/fuji/tiles/` combine information across multiple exposures of the same tile, but not across different tiles even if the same target was observed on multiple tiles (such as high-redshift quasars). Full-depth coadds combine exposures for targets on a given HEALPix (Górski et al. 2005) pixel of sky, including combining data across tiles if the same target was observed on multiple tiles. These coadds are referred to as “healpix” coadds and redshifts since they are stored in files based on HEALPix pixel number (nested scheme, `NSIDE=64`) under `spectro/redux/fuji/healpix/`.

However, even in the healpix case, data are not combined across surveys (e.g., `sv1`, `sv2`, `sv3`) and programs (e.g., dark, bright, backup) in order to prioritize the uniformity of each (survey, program) combination. We anticipate that the tile-based spectra will be of primary interest to analyses of Target Selection Validation (`SURVEY=sv1`), while the HEALPix-based full-depth spectra will be used more for the overlapping rosettes of the One-Percent Survey (`SURVEY=sv3`) and future releases of DESI Main Survey data.

Tile-based spectra, coadds, classifications, and redshifts come in additional subgroupings under `spectro/redux/fuji/tiles/`. The `cumulative/` directory tree contains all data for each tile, coadded across exposures and nights. The `pernight/` directory tree combines data within a night but not across nights, enabling reproducibility studies of the same targets observed under different conditions on different nights. The `perexp/` directory contains classifications and redshift fits to individual exposures to explore performance and reproducibility at even lower S/N. Additional custom coadds, classifications, and redshift fits are available for selected tiles to match the expected depth of the Main Survey (`1x_depth`),

4 times the expected Main Survey depth (`4x_depth`), and coadds using only data from poor observing conditions (`lowspeed`).

If a file was only observed on a single exposure on a single night, the `cumulative/`, `pernight/`, and `perexp/` outputs are identical, but they are still kept in all three directories so that each can be used independently.

Future data releases will continue to support `tiles/`, `cumulative/` and `healpix/`, but other groupings of tile-based spectra will not be included for Main Survey data and may be dropped from reprocessing runs of the SV data.

3.3.3. Redshift Catalogs

Redshift and classification catalogs for individual tiles and healpix are available in the same directories as the spectra and coadds to which they were fit. For convenience, these catalogs are also combined across the thousands of individual files into stacked redshift catalogs in `spectro/redux/fuji/zcatalog/`. Like the spectra and coadds, these come in multiple groups, e.g., combining all of the cumulative tile-based redshifts for a given (survey, program) into a single file, with different files for different (survey, program) combinations.

For analyses that simply want the recommended “best” redshift for a given target regardless of the DESI-specific (survey, program), `zall-pix-fuji.fits` combines all the HEALPix-based redshifts across all programs into a single file, with a `ZCAT_PRIMARY` boolean column indicating which row is considered the best redshift for each target. This uses the code `desispec.zcatalog.find_primary_spectrum`,¹²³ which could also be used by any analysis to subselect multiply observed targets from a custom selection of spectra to determine the recommended redshift. It first prioritizes results with `Redrock ZWARN==0`, then sorts by the LRG-optimized template `S/N TSNR2_LRG`, although users can specify a different secondary sort column. A description of the template S/N can be found in Section 3.1.2 with further details in Section 4.14 of Guy et al. (2023).

Similarly, `zall-tilecumulative-fuji.fits` provides all cumulative tile-based redshifts across surveys and programs, with `ZCAT_PRIMARY` indicating the recommended best single tile-based redshift per target.

3.3.4. Target Catalogs

Target catalogs used as an input for DESI observations were previously published under the “Early Target Selection” release available at <https://data.desi.lbl.gov/public/ets/> and described in Myers et al. (2023). Although the EDR does not include any new target selection catalogs, `edr/target/` links to the same directory tree as `ets/target/` so that the EDR can be used as a self-contained release including target selection information, without having to combine information across releases.

3.3.5. Fiber Assignment Catalogs

Fiber assignment is the process of assigning individual targets to individual fibers. In DESI, the assignment of targets to fibers for a given tile is designed by the `fiberassign` program, as described in A. Raichoor et al. (2023b, in preparation). The

¹²³ <https://github.com/desihub/desispec/blob/0.51.13/py/desispec/zcatalog.py#L13>

output files, called *fiberassign* files, that detail the fiber assignments used in the EDR can be found in `target/fiberassign/tiles/tags/0.5/`. Within each *fiberassign* file, the FIBERASSIGN table contains the mapping of assigned TARGETID to FIBER and LOCATION¹²⁴; the TARGET_RA and TARGET_DEC coordinates and proper motions PMRA, PMDEC, and REF_EPOCH; which are in the International Celestial Reference System tied to Gaia DR2 (Lindgren et al. 2018); the input photometry, object shapes, and quality flags used for primary target selection (Myers et al. 2023)¹²⁵; and the targeting bitmasks described in Sections A.1, A.2, and A.3.

In addition to the target-to-fiber assignments, each file contains all possible assignments in the POTENTIAL_ASSIGNMENTS and TARGETS extensions. The TARGETS table has one row per TARGETID and includes the targeting bitmasks for each potential target. The POTENTIAL_ASSIGNMENTS table only has TARGETID, FIBER, and LOCATION columns; providing the mapping of which fibers could reach that target, with potentially multiple rows per TARGETID. Although *fiberassign* files contain the input photometry for targets that were assigned, they do not include full photometric information for unassigned targets covered by each tile, in order to keep the files to a manageable size. If photometric information is needed for unassigned targets, the TARGETIDs must be cross-matched back to the input targeting catalogs. This is most easily done by using the “LS/DR9 Photometry” VAC included in the EDR and discussed in Section 3.3.6, which combines and standardizes the information from the multiple input targeting catalogs.

Each raw data exposure directory also contains a copy of the *fiberassign* file that was used at the telescope at the time of observation. For some tiles, the photometry for secondary targets was incorrect, and this was corrected post facto in the files under `target/fiberassign/tiles/tags/0.5/`, which should be considered the most correct reference version. This was only done for catalog columns that were not actually used by observations. Spectroscopic data processing used these files to supersede the raw data versions when propagating the information downstream via the FIBERMAP extensions.

3.3.6. Value-added Catalogs

DESI data releases will include VACs, which are additional data products contributed by the DESI science collaboration. VACs are built upon the core data products (spectra, classifications, redshifts) from this spectroscopic data release.

EDR will include a set of VACs with the initial release, but will also add additional VACs based upon EDR when they become available from the DESI science collaboration in the future. The website <https://data.desi.lbl.gov/doc/vac/> will be kept up to date with details of the available VACs, including documentation and references to relevant journal articles. The files can be accessed in the same manner as the EDR data under the `vac/` subdirectory. In the rest of this section, we present

¹²⁴ FIBER [0-4999] tracks the position of the spectra on the spectrographs, with the spectrograph number=petal number=int(FIBER/500). LOCATION tracks the position of the fiber on the focal plane, which is purposefully randomized with respect to FIBER to break degeneracies between systematics related to position on the focal plane versus position on the spectrographs. Although there is a fixed 1:1 mapping between FIBER and LOCATION, both are recorded for convenience.

¹²⁵ Secondary targets are allowed to come from any data source, and thus, their exact input selection parameters are not tracked here.

two VACs in the EDR that are broadly applicable to many analyses using the EDR data—the LS/DR9 Photometry VAC and the SV Visual Inspection VAC. The LSS catalogs VAC used for DESI LSS analyses will also be described in Section 4. Additional VACs are available and described on the website.

LS/DR9 photometry VAC. This VAC delivers merged targeting catalogs (*targetphot*) from DESI target selection (Myers et al. 2023) and Tractor¹²⁶ catalog photometry (*tractorphot*) from the DESI LS/DR9 (Dey et al. 2019)¹²⁷ for all observed and potential targets (excluding sky fibers) in the EDR. The observed targets in this VAC correspond to objects with at least one spectrum in the EDR, while the potential targets are the targets that DESI *could have* observed in a given fiber assignment configuration (including the objects, which were actually observed).¹²⁸ The construction and organization of the LS/DR9 VAC are fully documented at <https://github.com/moustakas/desi-photometry>; here, we briefly describe its contents.

The LS/DR9 VAC includes *tractorphot* catalogs, which contain Tractor catalog photometry for every unique target in the *targetphot* catalogs. These catalogs are “value-added” compared to the information in catalogs described in Section 3.3.4 in two key ways. First, the *tractorphot* catalogs contain *all* the photometric quantities measured by Tractor in the LS/DR9, not just the measurements included in the light-weight sweep catalogs used to select DESI targets (see also Myers et al. 2023). Second, the *tractorphot* catalogs include photometry for targets that were not necessarily targeted from the LS/DR9, such as secondary targets and targets of opportunity (ToOs), by finding the LS/DR9 object within 1'' of the observed (or potential) DESI target.

SV visual inspection VAC. During the SV period, in order to validate the performance of the DESI pipeline and assist the target selections of the Main Survey, DESI members visually inspected (VI’ed) the deep coadded spectra of 16,594 galaxy targets; including 2718 BGS; 3,561 LRG; and 10,315 ELG targets; in addition to 5496 QSO targets. Each spectrum had at least two inspectors. Each inspector reported the VI redshift, the redshift quality, the source type, issues observed in the spectrum, and any extra comments for each spectrum. The results from the inspectors were combined and reconciled by the VI chairperson if needed. This VI information was used to quantify the performance of the DESI operation and validate the design of the survey. The details of the compilation of the catalogs and the corresponding analyses are summarized in Lan et al. (2023) for galaxies and Alexander et al. (2023) for quasars.

These VI catalogs are provided as a VAC in the EDR. The catalogs are organized based on the target types. For galaxies, we provide the catalogs for BGS, LRG, and ELG separately. For QSO, we provide two catalogs: the quasar-survey deep-field VI catalog analogous to that provided for the galaxies, and the missed QSO catalog from a sparse VI campaign (see Tables 1 and 4; and Section 2.3 of Alexander et al. 2023 for details). Each catalog contains target information, including TARGETID, TILEID, FIBER, TARGET_RA, and TARGET_DEC; and VI information, including the VI redshift (VI_Z), the redshift

¹²⁶ <https://github.com/dstdstn/tractor>

¹²⁷ <https://www.legacysurvey.org/dr9/description>

¹²⁸ Note that these catalogs are distinct from the photometric target catalogs described in Section 3.3.4, which contain *all* the possible photometric targets with no reference to DESI observations.

quality (VI_QUALITY), and the type of the source (VI_SPECTYPE). Note that we do not include issues or comments reported by the inspectors since most of them reflect the status of the spectra processed by an early version of the pipeline, rather than the improved pipeline used for the EDR. With the target information, one can crossmatch the VI catalogs with other catalogs in the EDR and obtain information on the sources such as the photometric properties as well as the redshift information from the DESI pipeline. We recommend using $VI_QUALITY \geq 2.5$ as a selection criterion for sources with confident VI redshifts; see Section 2 of Lan et al. (2023) and Section 2.2 of Alexander et al. (2023) for details of the VI_QUALITY flags within the context of the galaxy and quasar catalogs, respectively. There are 2640 BGS; 3513 LRG; 7856 ELG; and 4890 QSO targets with any VI classification and $VI_QUALITY \geq 2.5$. In total, there are 14,939 objects identified as a VI_SPECTYPE==GALAXY; 3182 objects identified as a QSO; and 778 identified as a STAR with $VI_QUALITY \geq 2.5$.

3.4. Other Files

In addition to the high-level user-facing data products, DESI data releases also contain raw data and intermediate data products.

The original raw data are available in `spectro/data/NIGHT/EXPID/` subdirectories where `NIGHT` is the YEARMDD date of sunset,¹²⁹ and `EXPID` is the zero-padded eight-digit monotonically increasing exposure identification number. These directories contain the original fiber assignment observing request, raw data from the spectrographs, guiders, fiber view camera, and sky monitors, and fits to those data performed as part of fiber positioning and field acquisition. For discussion of the instrument components, see DESI Collaboration et al. (2022), and for discussion of the survey operations, see Schlafly et al. (2023).

Intermediate data processing files in subdirectories of `spectro/redux/fuji/` include preprocessed spectrograph CCD data (`preproc/`); nightly biases, and arc- and flat-lamp calibrations (`calibnight/`); and intermediate spectra steps (`exposures/`), e.g., sky-subtracted spectra that are not flux calibrated (`sframe-*.fits.gz`).

For completeness, the EDR contains all inputs used by the spectroscopic processing pipeline, including CCD calibration files in `spectro/desi_spectro_calib/` and `spectro/desi_spectro_dark/`; stellar templates used to fit standard stars in `spectro/templates/basis_templates/`; and survey progress bookkeeping files in `survey/ops/` used to track if a tile is “done” and should be included in a release.

3.5. Known Issues

While working with the internal prerelease of EDR, the DESI collaboration has identified several issues with the data produced by the pipeline, which we report here for completeness.

1. Redrock templates do not include AGN-like galaxies with a mixture of broad and narrow lines. As a result, these types of galaxies are often fit equally well (or

equally poorly) with either GALAXY or QSO templates at the same redshift, which can also trigger ZWARN bit 2 (value $2^2=4$) for LOW_DELTACHI2 since the χ^2 difference between the two fits is small, indicating an ambiguous answer.

2. There are cases where Redrock is overconfident and reports $ZWARN==0$, i.e., no known problems, even though the fit is incorrect. This can include unphysical fits due to the overflexibility of PCA template linear combinations. This is particularly true for sky fibers, which have a higher fraction of $ZWARN==0$ than would be expected from purely random fluctuations. Users should be especially cautious in any search for serendipitous targets in nominally blank sky fibers.
3. The Redrock galaxy fits extend to redshift $z=1.7$, although the range $1.6 < z < 1.63$ is only constrained by the [O II] doublet in the midst of significant sky background while $1.63 < z < 1.7$ has no major emission line coverage. Thus, $1.6 < z < 1.7$ is particularly susceptible to unphysical fits. This was the motivation for the LSS catalogs to only consider galaxies with $z < 1.6$ (see Section 4).
4. Negative TARGETIDs indicate positioners that were nonfunctional and thus were not pointing at a known science target. Although these are unique within a given TILEID, they are not unique values across different TILEIDs. Since these are not science targets, most users can discard any negative TARGETID targets. This has been fixed for Main Survey nonfunctional positioners in future data releases, where negative TARGETIDs will be unique.
5. For most of the tiles in Target Selection Validation, proper-motion corrections were applied in fiberassign when the tile was designed.¹³⁰ A consequence is that the (TARGET_RA, TARGET_DEC, and REF_EPOCH) values are altered to have a REF_EPOCH of the date that the tile was designed, which makes them differ from the input photometric column values. The information is correct and consistent with the photometry, however.
6. In the coadded FIBERMAP tables, 0.03% of targets incorrectly have $COADD_FIBERSTATUS==0$ even though all of their data are masked. These result in $ZWARN \neq 0$ in the redshift fits, but the quality cuts based solely upon $COADD_FIBERSTATUS$ have a tiny amount of contamination.
7. In the coadded FIBERMAP tables, MEAN_FIBER_RA and MEAN_FIBER_DEC record the average as-observed position of the fibers (in comparison to the intended positions recorded in TARGET_RA and TARGET_DEC plus proper motions PMRA, PMDEC, REF_EPOCH). The FIBERMAP coordinate coaddition incorrectly included exposures that had been excluded from the spectral coaddition, which can result in incorrect MEAN_FIBER_RA/DEC values. The same issue applies to the standard deviations recorded in STD_FIBER_RA/DEC. As a result, TARGET_RA/DEC are more reliable than MEAN_FIBER_RA/DEC, while noting that the actual positioning can vary by $O(0''.1)$, which is still small compared to the $\sim 1''.5$ diameter fibers.

¹²⁹ The DESI “night” rolls over at KPNO noon, not midnight, so that data from a single observing night are grouped together even though they span 2 calendar days.

¹³⁰ The design date can differ from when a tile was observed.

Additional known issues and clarifications will be documented at <https://data.desi.lbl.gov/doc/releases/edr> when needed.

4. One-Percent Survey LSS Catalogs

DESI creates LSS catalogs from its data in order to facilitate clustering measurements. The overall process is similar to that applied to SDSS (most recently, eBOSS; Ross et al. 2020). We determine the area on the sky where good observations were possible for each tracer, applying criteria on the DESI data to select reliable redshifts, and provide weights that correct for variations in observing completeness. The end results are data and matched random catalogs, split into the various relevant DESI tracer classes, that can be passed directly to any common software for calculating redshift-space clustering measurements.

These catalogs for the One-Percent Survey are ideal for studying small-scale clustering, as the tiling strategy makes them highly complete for all tracer types (DESI Collaboration et al. 2023). Some studies using the results derived from these catalogs include Gao et al. (2023), A. Pearl et al. (2023, in preparation), Prada et al. (2023), Rocher et al. (2023), Yu et al. (2023), and Yuan et al. (2023). The catalog files are available in the EDR at `vac/edr/lss/v2.0`; see Section 5 for data access details.

4.1. Gathering Assignment and Observation Information

The DESI LSS catalogs begin by gathering the information that describes where and what on the sky DESI could observe. Two fundamental pieces of this information were generated by the DESI targeting team (Myers et al. 2023). These are (1) the data chosen (“targeted”) for spectroscopic follow-up, including photometric properties of the targets and metadata related to their observation (hereafter simply “data”) and (2) a uniform random distribution of points on the sky occupying the area covered by Legacy Survey imaging that also includes the metadata related to the photometric observations at the given location (hereafter “randoms”; see Section 4.5 of Myers et al. 2023). Both the data and randoms were given a unique identifier, `TARGETID`, by the DESI targeting team, and this identifier is used to match between relevant data files in all relevant cases. We use 18 random files (more are available), each with a density 2500 deg^{-2} . The 2500 deg^{-2} is convenient, as it allows for quick determination of footprint area after various cuts.

With these data and randoms, we first track the locations on the sky where DESI observations could have happened. We do this using the outputs of the DESI `fiberassign` software (A. Raichoor et al. 2023b, in preparation). As described in Section 3.3.5, prior to the observation of each DESI tile, targets are processed through `fiberassign` in order to assign targets to particular fibers (with each unique fiber corresponding to a unique robotic positioner and a unique location in the spectrograph CCDs). In addition to the particular assignment, the information on all potential assignments is also stored for each tile. Further, all settings used when running the `fiberassign` software are stored so that the assignments can be reproduced. This means that we can also run the randoms through `fiberassign`, with the matched settings. The positions of the randoms in the potential assignments thus provide a superset of the geometric area observable by DESI on every tile. We thus

concatenate the potential assignment information across all tiles for both data and randoms.¹³¹

The total set of concatenated potential assignment information includes many duplicated targets. In the One-Percent Survey, each location on the sky was potentially covered 13 times. Further, many sky locations are accessible to more than one robotic positioner. Initially, we keep all of the information on repeated potential assignments. Downstream, many will be vetoed, e.g., due to hardware performance or low data quality. At this stage, we also match to the information on redshifts in the cumulative tile-based redshift catalog provided in the EDR (see Section 3.3.2). For the data, we match not just to the target, but to the particular tile and fiber on which it was observed.¹³² Many rows for the data will have no match, and the corresponding entries will simply be null. For the randoms, we match in order to obtain the metadata related to the particular spectrum. We, therefore, match only to the tile and fiber and will have a match for all random targets.¹³³

The information on the number of overlapping tiles allows us to divide the observed area by coverage. The covered area listed in Table 2 is simply the unique area that is overlapped by any tile in that survey, but it does not include the detailed accounting for focal plane geometry, disabled/broken hardware, or higher-priority targets blocking lower-priority targets from being observed. Using data and randoms and repeated realizations of fiber assignment provides a much more accurate and geometrically detailed measurement of the true coverage.

Figure 4 displays this information for rosette number 1 (SV3 R1 in Table 4) of the bright-time program. Each point is a BGS target at a location covered at least once by the One-Percent Survey. One can see that some areas were covered up to 11 times. For dark-time observations, areas were covered up to 13 times. This dense coverage provides highly complete samples.

In order to jointly model the completeness of all targets with respect to each other, we simulate the observation of targets in the One-Percent Survey using multiple realizations of their assignment histories. The process and its results are described in more detail in J. Lasker et al. (2023, in preparation). Briefly, all DESI targets were initially assigned a random `SUBPRIORITY`, which is used to determine which target gets assigned a fiber when available targets have the same overall priority (see A. Raichoor et al. 2023b, in preparation; Myers et al. 2023). We create 128 alternative assignment histories by randomly shuffling the subpriorities 128 times.¹³⁴ For each of the 128 realizations, the One-Percent Survey observations are simulated by following the same order of tile observations and targeting feedback loop.¹³⁵ From these simulations, we package the results as a bit-value for each target that encodes the realization numbers it was observed in.

¹³¹ They are available in `vac/edr/lss/v2.0/potential_assignments`.

¹³² The particular columns used for the match are `TARGETID`, `TILEID`, `LOCATION`; `LOCATION` refers to the robotic positioner, which corresponds to a unique fiber.

¹³³ The files with matches to spectroscopic information are available at `vac/edr/lss/v2.0/inputs_wspect`.

¹³⁴ Each of the alternative assignment histories is available in `vac/edr/lss/v2.0/altmtl`.

¹³⁵ Targets with good observations have their priority adjusted so that unobserved targets are more likely to be assigned; see Section 5 of Schlafly et al. (2023).

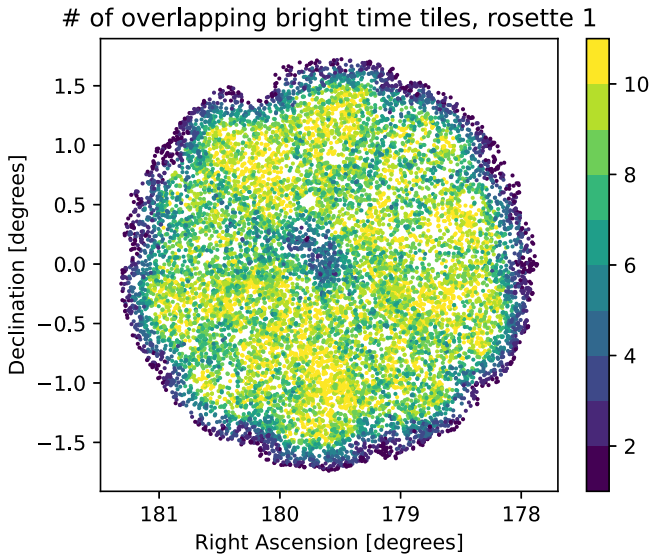


Figure 4. The number of overlapping bright-time tiles at each location of a BGS target in “rosette” number 1 of the DESI One-Percent Survey (SV3 R1 in Table 4).

From these bit-values, one can determine the individual and pairwise probabilities required to obtain unbiased clustering statistics (Bianchi & Percival 2017).

4.2. LSS Catalogs

The LSS catalogs are cut (subselected down) to unique TARGETID per supported tracer type. They come in two flavors. The “full” catalogs contain an entry for all reachable targets, whether or not they were observed.¹³⁶ They also include all columns believed to possibly be relevant. The “clustering” catalogs cut to good spectroscopic observations and the redshift range intended for clustering analysis.¹³⁷ They include weights to account for variations in the selection function and only include the columns required to calculate clustering statistics.

Catalogs were created for the four extragalactic DESI target types: BGS, LRG, ELG, and QSO. For all except QSO, catalogs are produced for additional subtype definitions. In the cases where the subtype corresponds to a bit-name from SV3 targeting (see Table 15 and surrounding text), we use that name. The additional LRG selection, named LRG_main, keeps only targets that satisfy the Main Survey selection (see Zhou et al. 2023 for details). The ELG sample is cut in three additional ways. First, ELG_HIP contains only the $\sim 75\%$ of the ELG sample assigned higher priority (see Raichoor et al. 2023 for more details). Then, for each of ELG and ELG_HIP, we also remove QSO targets. QSO targets have the highest priority, and it may, therefore, be useful to treat any targets that satisfy both the QSO and ELG selections within the QSO analysis. Finally, there are two BGS samples: BGS_ANY and BGS_BRIGHT. BGS_ANY is the combination of both the BGS_BRIGHT and BGS_FAINT BGS selections. See Hahn et al. (2022) for more details. A summary of the statistics for all tracer types is given in Table 8.

¹³⁶ They are available in `vac/edr/lss/v2.0/LSScats/full`.

¹³⁷ They are available in `vac/edr/lss/v2.0/LSScats/clustering`.

Table 8
Statistics for Each of the DESI Tracer Types for Which One-Percent Survey LSS Catalogs Were Created

Tracer	No. of Good z	z Range	Area (deg ²)	Completeness
BGS_ANY	241,746	$0.01 < z < 0.6$	174	94%
BGS_BRIGHT	143,853	$0.01 < z < 0.6$	174	96%
LRG	112,649	$0.4 < z < 1.1$	167	95%
LRG_main	86,040	$0.4 < z < 1.1$	167	95%
ELG	267,345	$0.6 < z < 1.6$	169	86%
ELGnotqso	259,317	$0.6 < z < 1.6$	164	88%
ELG_HIP	209,833	$0.6 < z < 1.6$	169	89%
ELG_HIPnotqso	202,734	$0.6 < z < 1.6$	164	90%
QSO	35,566	$0.6 < z < 3.5$	175	98%

Note. We list the number of good redshifts included, the redshift range we included them from, the sky area occupied, and the observational completeness within that area. The area is slightly different for different tracer types due to priority vetoes (e.g., a QSO target can remove sky area from lower-priority samples). The completeness listed is the number of targets observed divided by the number of targets within the entire observable area. The completeness can be increased by cutting on the rosette radius (see text and Figure 5).

4.2.1. Full Catalogs

Starting from the compilation of all potential observations, the first step in creating the full catalogs for the data is to cut to targets of a given target type. We then cut to unique targets. We cannot do so randomly, as, e.g., we must keep the cases that have been observed. We define the following boolean quantities:

1. H_{good} . The particular fiber on the given tile was observed with good hardware.
2. L_{fa} . The particular target, fiber, and tile were assigned and observed.
3. T_{fa} . The particular fiber and tile (but not necessarily target) were assigned and observed.
4. S_{good} . The particular fiber and tile (but not necessarily target) were determined by the spectroscopic pipeline to have a template squared S/N (T_{SNR2} , referred to here as S_{ratio}) above the vetoing threshold (defined below).

We clip S_{ratio} to be within the range (0, 200), and then, these quantities are combined to create a value to sort by

$$v_{\text{sort}} = L_{\text{fa}} S_{\text{good}} H_{\text{good}} (1 + S_{\text{ratio}}) + T_{\text{fa}} H_{\text{good}} + H_{\text{good}}. \quad (1)$$

We sorted by this v_{sort} in ascending order and then cut to unique targets by selecting the last entry for each unique target. After cutting to unique targets, we join to the redshift determined in the HEALPix-based redshift catalog and use Z_{HP} as the column name.

For ELG catalogs, we join the information on the [O II] emission line fits, produced with the spectroscopic release using the HEALPix-based coadd. We combine the information on [O II] flux and its inverse variance to obtain the S/N of the [O II] flux for each observed spectrum, which we denote $S_{[\text{O II}]}$. Following Raichoor et al. (2023), this information is combined with the $\Delta\chi^2$ obtained from the redshift fitting pipeline between the best and next-best-fit redshifts (the quantity DELTACHI2 in Section 3.1.3) to determine a criterion,

$[\text{O II}]_{\text{crit}}$ for selecting reliable redshifts:

$$[\text{O II}]_{\text{crit}} = \log 10(S_{[\text{O II}]}) + 0.2 \log 10(\Delta\chi^2). \quad (2)$$

For quasars, we join to the HEALPix-based quasar catalog, which contains extra information related to classifying the spectra as QSO or not and improved redshift estimates. These catalogs will be released as a VAC and will be fully documented in R. Canning et al. (2023, in preparation). The fiducial pipeline estimates of the redshifts are replaced by those from the quasar catalog.¹³⁸ The flavor of the quasar catalog that we use is the one that only contains entries for objects believed to be quasars.¹³⁹ Thus, there will be many more rows with null entries for the quasar information than for those with Redrock information.

For randoms, we must also cut to unique TARGETID, and we do so separately for each tracer type, as the tracer information is included in the sort. We also apply the imaging mask bits that were applied to the target samples. These are Legacy Survey bits¹⁴⁰ 1 (BRIGHT) and 13 (CLUSTER) applied to bright-time targets to flag objects with imaging pixels within half of the locus of a radius–magnitude relation of a “bright” star or in a globular cluster (GC) respectively. In addition, bit 12 (GALAXY) is included for dark-time targets to flag targets in a large galaxy in the Siena Galaxy Atlas (SGA; J. Moustakas et al. 2023, in preparation).¹⁴¹ In addition to the boolean quantities used to sort the data, we use the following:

1. P_{good} . The PRIORITY of the target that was assigned at the given tile and fiber was less than or equal to the PRIORITY of the given target class.
2. Z_{poss} . Either the tile and fiber were assigned to a target of the given target class, or no unassigned targets of the given target class were reachable by the fiber on this tile.

The randoms are then sorted by

$$v_{\text{sort}} = S_{\text{ratio}} H_{\text{good}} P_{\text{good}} Z_{\text{poss}}, \quad (3)$$

and we cut to unique random points by selecting the highest v_{sort} value for each.

The final step for the “full” catalogs is to apply vetoes.¹⁴² All of the boolean columns defined above for data and randoms must be True to pass the veto. Note that the combination of the P_{good} and Z_{poss} criteria act as a priority veto mask. Thus, the area occupied by the lowest-priority targets (as traced by the number of randoms) will be less than the highest-priority ones.

The sky area occupied for each target class in the One-Percent Survey is given in Table 8. The difference between the highest (QSO) and lowest (ELGnotqso) priority targets is only 7% due to the survey strategy to achieve high coverage. The ELG catalogs with QSO targets removed have a smaller area than those including the QSO targets because the priority used for the P_{good} determination is that of QSO when they are included but that of ELG_HIP targets when they are not.

¹³⁸ We replace the original Z_{HP} column with that from the quasar catalog and rename it Z_{RR} (to indicate “Redrock”). Z_{ERR} from the quasar catalog is renamed as $Z_{\text{ERR_QF}}$, and Z_{ERR} remains the Z_{ERR} from Redrock.

¹³⁹ We use the following file: `QSO_cat_fuji_sv3_dark_healpix_only_qso_targets.fits`. The quasar catalog will also provide a flavor that includes the diagnostic information for all targets.

¹⁴⁰ <https://www.legacysurvey.org/dr9/bitmasks/#maskbits>

¹⁴¹ <https://github.com/desihub/desitarget/blob/1.1.1/py/desitarget/geomask.py#L137>

¹⁴² The catalogs that have “noveto” in the file name are the catalogs produced prior to this veto process.

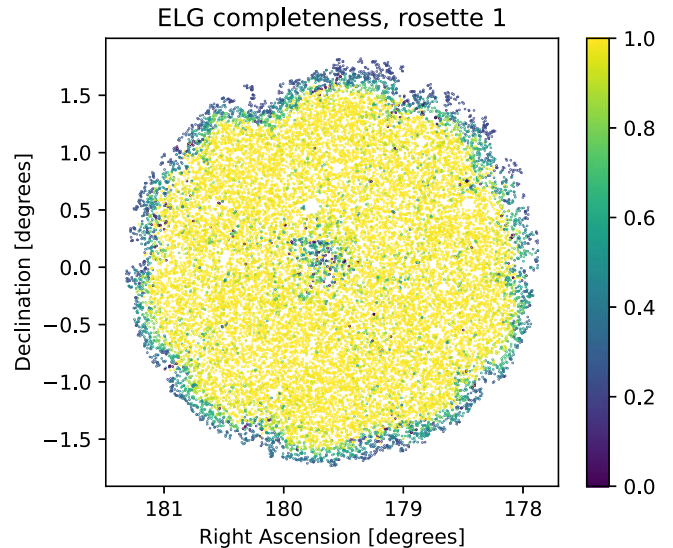


Figure 5. The observational completeness within each tile grouping of ELG targets on “rosette” number 1 (SV3 R1 in Table 4) from the DESI One-Percent Survey.

Correspondingly, there is a small increase in the completeness of the ELG samples with the QSO targets removed, as the area removed was at sky locations where only QSO targets were observable.

Finally, additional vetoes are applied based on the imaging data. For LRGs, we apply a custom mask, described in Zhou et al. (2023). For the other tracers, Legacy Survey bit 11 (MEDIUM) is always used to flag objects with imaging pixels within the locus of a radius–magnitude relation of a “medium” brightness star. For QSO, bits 8 (WISEM1) and 9 (WISEM1) are also applied. These refer to targets with pixels in the imaging that have a WISEMASK_W1 or WISEMASK_W2 bright star mask flag set respectively.

Given the vetoed catalogs, we determine a completeness both per fiber, C_{fib} , and per unique tile grouping, C_{tile} . Per fiber is simply the inverse of the number of data points at a given tile and fiber.¹⁴³ The values of C_{fib} are similar to the P_{obs} value obtained from 128 alternative assignment histories. The completeness per-tile grouping is simply the observed number divided by the total number within each tile group, i.e., $C_{\text{tile}} = N_{\text{observed}}/N_{\text{total}}$. As an example, Figure 5 shows the completeness, C_{tile} , of ELG targets in rosette number 1. The pattern observed there is typical of all rosettes. The ELG completeness in the plotted rosette is 87%, and across all rosettes, it is 86%. The ELG sample has the lowest completeness, as they had the lowest target priority. The completeness decreases toward the edges and the center, as the total number of overlapping tiles decreases in these regions. The completeness increases to 95% if one cuts to $0.2 < r_{\text{rosette}} < 1.45$, where r_{rosette} is the angular distance from the center of the rosette, in degrees.¹⁴⁴

4.2.2. Clustering Catalogs

For both data and randoms, the clustering files take the full files and reduce them to a subset of columns necessary for calculating two-point statistics. The full data file is cut to only

¹⁴³ In the catalogs, the column is `FRACZ_TILELOCID`.

¹⁴⁴ The corresponding column name is `ROSETTE_R` in the catalogs.

those objects with good redshifts and weights to account for selection function variations.

Catalogs are provided for the ‘‘S’’ (Dark Energy Camera Legacy Survey; DECaLS) and ‘‘N’’ (Beijing-Arizona Sky Survey/Mayall z-band Legacy Survey; BASS/MzLS) photometric regions (see Section 4.1.3 of Myers et al. 2023). Given that the photometry is different because different cameras/filters were used for each, we expect at least slight differences in the selection function between the two regions and thus will always estimate it separately. The area in the S and N regions is nearly identical for the One-Percent Survey. The difference varies from the S region being less than 1% greater for the ELG samples to 4% greater for the LRG sample.¹⁴⁵

Only data with good redshifts are kept. We use the HEALPix-based redshift (see Section 3.3.2) as the estimate for the redshift.¹⁴⁶ Each tracer has a different definition for a ‘‘good’’ redshift, as detailed in the respective target selection papers (BGS, Hahn et al. 2022; LRG, Zhou et al. 2023; ELG, Raichoor et al. 2023; and QSO, Chaussidon et al. 2023). The criteria were motivated by maximizing the completeness while minimizing the fraction of catastrophic failures expected for the Main Survey observations and used a combination of comparisons of Redrock redshift to a VEd redshift or multiple Redrock redshifts from repeated observations of the target. The estimated catastrophic failure fractions are less than 0.5% for all tracer types after restricting to ‘‘good’’ redshifts. Key quantities used to select good redshifts are the redshift pipeline flag ZWARN and the $\Delta\chi^2$ (DELTAChi2) obtained from the redshift fitting pipeline between the best and next-best-fit redshifts. We also restrict to a given redshift (z) range that is different for each tracer. The combined criteria are as follows:

1. *BGS*. ZWARN==0, $\Delta\chi^2 > 40$, $0.01 < z < 0.6$.
2. *LRG*. ZWARN==0, $\Delta\chi^2 > 15$, $0.4 < z < 1.1$.
3. *ELG*. [O II]_{crit} > 0.9, $0.6 < z < 1.6$ (with [O II]_{crit} defined by Equation (2)).
4. *QSO*. Not already rejected by the quasar catalog, $0.6 < z < 3.5$.

The quasar catalog requires that either Redrock or QuasarNET identified the object as a QSO, while the galaxy catalogs (BGS, LRG, ELG) do not explicitly require that the targeted objects are spectrally classified as galaxies.

For the DESI One-Percent Survey, we provide two weights to be used with the clustering catalogs. One, w_{comp} , accounts for fiber assignment incompleteness. The other, w_{FKP} , optimizes against expected S/N in two-point clustering measurements as a function of redshift and is based on Feldman et al. (1994). We will describe both below. In previous SDSS (most recently, Ross et al. 2020) and future DESI LSS catalogs, weights that account for fluctuations in both target density due to imaging quality and redshift success due to the S/N of spectroscopic observations are added. We do not include such weights for the DESI One-Percent Survey LSS catalogs. For target density fluctuations, their effects typically manifest on large angular scales, and the relatively small area of the One-Percent Survey footprint is not ideal for the regression methods typically used to define them. For the redshift success, the effective exposure time reached during the One-Percent Survey was such that (after selecting the greatest

S/N measurement out of any repeat observations) the variation in success rate is relatively low. Determining these weights for DESI Main Survey data is a primary focus of DESI year 1 analyses.

The completeness weights,¹⁴⁷ w_{comp} , are determined from the 128 realizations of alternative assignment histories. The process of generating these realizations is detailed in J. Lasker et al. (2023, in preparation). Given there is one data realization, we have 129 total realizations. The number of realizations in which a target was assigned is thus $128P_{\text{obs}} + 1$. The probability of assignment is $N_{\text{assigned}}/N_{\text{tot}}$, and we wish to use the inverse probability as the weight. Thus,

$$w_{\text{comp}} = 129/(128P_{\text{obs}} + 1). \quad (4)$$

These weights can be used to obtain unbiased statistics for any one-point measurement or for clustering measurements on projected scales that are large relative to the fiber-patrol radius, which is at most $89''$ (it depends on, e.g., the focal plane position due to the optics). For unbiased N -point clustering statistics in general, one should use the bit-values to determine the joint probability for any configuration, and, e.g., for two-point statistics following the process outlined in Bianchi et al. (2018). Comparisons of clustering results applying (or not) various weighting prescriptions to the One-Percent Survey data are presented in J. Lasker et al. (2023, in preparation), Rocher et al. (2023).

The clustering randoms contain the same rows as the full random files. Redshifts and weights are added to the randoms by randomly sampling the data. In this way, the weighted dN/dz of the data and random should match (and the weights on the random points are there *only* for this purpose). Other columns, such as photometry, that vary with redshift are similarly sampled. In all cases, any cuts that are applied to the data sample should also be applied to the random sample. Potential choices include, e.g., cuts on r_{rosette} , N_{tile} , or redshift. Any number of random files (recall, 18 total are available, each with a projected density of 2500 deg^{-2}), or even a subselection of a random file, can be used without biasing any potential statistic, with the caveat that using less random points means a higher shot-noise contribution from the randoms.

The comoving number density as a function of redshift, $n(z)$, is determined for each tracer by applying the completeness weights, and represents the estimated density for a complete sample. In order to calculate the comoving volume, we use a cosmological model based on the Planck 2018 results¹⁴⁸ (Aghanim et al. 2020) and calculate all comoving distances in the units $h^{-1} \text{ Mpc}$. The $n(z)$ are determined separately for the ‘‘N’’ and ‘‘S’’ regions. Figure 6 shows the measured $n(z)$, taking a simple mean of the ‘‘N’’ and ‘‘S’’ results. The $n(z)$ are used to determine the w_{FKP} weights that are included in the clustering catalogs.¹⁴⁹ We use

$$w_{\text{FKP}}(z) = \frac{1}{1 + n(z)P_0}. \quad (5)$$

¹⁴⁵ The N region in the One-Percent Survey has more area affected by stars that are bright in the infrared.

¹⁴⁶ Thus, for the ‘‘clustering’’ catalogs, the column ‘‘Z_HP’’ is changed to ‘‘Z.’’

¹⁴⁷ Their column name is WEIGHT_COMP; the column WEIGHT is identical to WEIGHT_COMP for the One-Percent Survey LSS catalogs, but this will not be the case for future DESI LSS catalogs.

¹⁴⁸ Specifically, the 2018 Planck TT, TE, EE+lowE+lensing mean results, including massive neutrinos.

¹⁴⁹ The column name is WEIGHT_FKP.

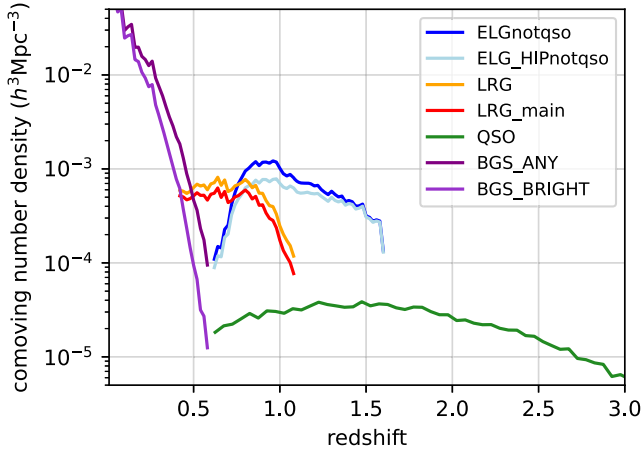


Figure 6. The comoving number density for samples used to create LSS catalogs in the DESI One-Percent Survey. For this display, we have taken the mean of the results in the “N” and “S” regions (see text for details).

We use a value of P_0 that is different for each tracer type and is approximately equal to the power spectrum amplitude at $k = 0.15h \text{ Mpc}^{-1}$; the values are 10^4 , 7000, 6000, and 4000 $\text{Mpc}^3 h^{-3}$ for LRG, BGS, QSO, and ELG.

4.2.3. BGS k - and e -Corrections

The BGS sample is approximately flux limited; thus, its galaxies will have an especially large range in their intrinsic luminosity. In order to compare the clustering of BGS galaxies at different redshifts and luminosities, we provide “ k ” and “ e ” corrections. Typically, absolute magnitudes are corrected by k -corrections to account for bandshifting effects, specifically that the observed flux distributions in a given passband will be different in the rest frames of galaxies at different redshifts. We thus provide r -band absolute magnitudes, M_r , with the BGS clustering catalogs,¹⁵⁰ defined via

$$M_r - 5 \log_{10}(h) = m_r - 5 \log_{10}(d_L(z)) - k_r(z). \quad (6)$$

Here, the subscript r represents the r band, $k(z)$ represents the k -correction of the galaxy, and $d_L(z)$ is the luminosity distance to the redshift z , determined using the same cosmology defined in the previous subsection (see Hogg et al. 2002 for a good overview of k -corrections). Optionally and in addition, an e -correction may be applied in order to account for the intrinsic luminosity evolution of a galaxy over time. Further, we derive the reference-frame $g - r$ color and thus also the g -band k correction. Results are provided using both $z = 0$ and $z = 0.1$ as the reference-frame.¹⁵¹

The methods we use to determine the BGS EDR $k + e$ corrections are detailed in S. Moore et al. (2023, in preparation).¹⁵² To begin with, we make use of the GAMA DR4 data set to create estimates of the k - and e -corrections (Driver et al. 2022). Each galaxy has an individual k -correction polynomial, calculated using KCORRECT v4.2 (see Blanton & Roweis 2007; Loveday et al. 2012 for further details). As such, each galaxy has an individual $k(z)$, given its observed $g - r$. These $k(z)$ values are divided into seven equal-

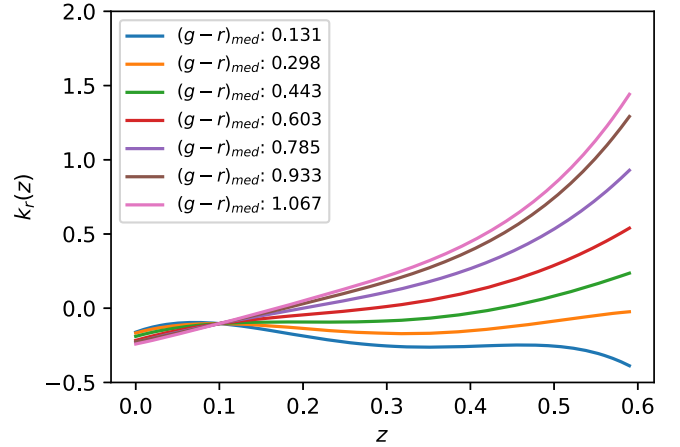


Figure 7. The seven r -band k -correction polynomials for median rest-frame $(g - r)_0$ in each color bin.

width $(g - r)_0$ color bins. Within each of these color bins, a fourth-order polynomial is fitted to the data points corresponding to the median $(g - r)_0$ color of the bin (see Figure 7). The polynomial is based on the functional form shown in Equation (7).

$$k(z) = \sum_{i=0}^4 a_i (z - z_{\text{ref}})^{4-i}. \quad (7)$$

The coefficients of the polynomials for $z_{\text{ref}} = 0.1$ are shown in Table 9. Moreover, a linear interpolation between these color polynomials is done such that the k -correction of a galaxy is found based on its rest-frame $(g - r)_0$ color and its redshift. The rest-frame $(g - r)_0$ colors for the DESI galaxies are found using an iterative root-finding method (Brent’s method as the default). Note that, for all k -corrections,

$$k(z_{\text{ref}}) = -2.5 \log_{10}(1 + z_{\text{ref}}) \quad (8)$$

is true. As such, the zeroth-power coefficient (a_4) enforces this condition for all individual k -correction polynomials, explaining why they are all the same value for each color bin.

Finally, the e -corrections we provide are determined using the same functional form as McNaught-Roberts et al. (2014):

$$E(z) = -Q_0(z - z_{\text{ref}}). \quad (9)$$

Specifically, we assume that the density evolution (P) is zero, and the luminosity evolution (Q) is the only factor to be considered. We provide results for the r band, for which we use $Q_0 = 0.97$ following the result found empirically in McNaught-Roberts et al. (2014). One can subtract the resulting $E(z)$ from M_r in order to obtain, e.g., BGS samples that have minimal evolution in number density with redshift.

5. Data Access

DESI data access is currently very file oriented, reflecting the manner in which most DESI collaborators access and use the data. In addition to these files, value-added data services and products are under development including a database and a suite of tutorials. The latter are provided on a best-effort basis to the community for convenience. We describe these data access methods as well as the data license and acknowledgments below. Documentation of DESI data access is further maintained at <https://data.desi.lbl.gov/doc/access/>.

¹⁵⁰ The column name is ABSMAG_R and is for the $z=0.1$ reference-frame.

¹⁵¹ Denoted via _OP0 and _OP1 in the column name for $z = 0$ and $z = 0.1$, respectively.

¹⁵² The code is at <https://github.com/SgmAstro/DESI>.

Table 9
Coefficient Table for the r -band k -correction Polynomials

Min	Max	Median	a_0	a_1	a_2	a_3	a_4
-100	0.18	0.131	-45.328	35.277	-6.604	-0.481	-0.104
0.18	0.35	0.298	-20.077	20.145	-4.620	-0.048	-0.104
0.35	0.52	0.443	-10.982	14.357	-3.676	0.339	-0.104
0.52	0.69	0.603	-3.428	9.478	-2.703	0.765	-0.104
0.69	0.86	0.785	6.717	3.250	-1.176	1.113	-0.104
0.86	1.03	0.933	16.761	-2.514	0.351	1.307	-0.104
1.03	100	1.067	20.302	-4.189	0.562	1.494	-0.104

5.1. File Access

For researchers who are members of other collaborations with NERSC account access, the files are directly available at `/global/cfs/cdirs/desi/public/edr/`, without requiring DESI membership. The exact same directory structure can be inspected, and individual files can be downloaded via <https://data.desi.lbl.gov/public/edr> without requiring a NERSC account. The efficient bulk download of larger amounts of data is available using the Globus¹⁵³ endpoint “DESI Public Data,” also without requiring a NERSC account. All three of these methods access the same files on disk at NERSC. The previous descriptions of file and directory locations in this paper started at the `public/edr/` level, regardless of whether that is prefixed by direct file access, `https`, `Globus`, or possibly some future data access method.

The entire EDR is over 80 TB, so users are encouraged to be selective in downloading only what they really need for an analysis. We anticipate that most users will start with one of the redshift catalogs in `vac/edr/lss/` or `spectro/redux/fuji/zcatalog/`, subselect to the objects of interest, and then proceed to download only the files containing spectra of those targets.

5.2. Other Interfaces

Catalog-level data (target photometry, fiber assignments, exposure metadata, spectral classifications, and redshifts, but not the spectra themselves nor most of the VACs) are available in a Postgres database with tables and access credentials described at <https://data.desi.lbl.gov/doc/access/database>. Users with NERSC accounts can directly query this database with Structured Query Language (SQL), or use SQLAlchemy wrapper objects provided with preinstalled `specprodDB` Python code. For users without NERSC credentials, a public copy of the database is available from the Astro Data Lab as described at <https://datalab.noirlab.edu/desi>. This platform includes anonymous public access via a web query interface and authenticated access via a JupyterLab server. Additionally, the Astro Data Lab serves a subset of DESI spectra via the SPectra Analysis and Retrieable Catalog Lab (SPARCL¹⁵⁴), which consists of a spectral database with a programmatic interface. The subset is limited to healpix-coadded spectra, which have been combined across cameras. Other types of spectra and files are only available at the primary file-based archive at NERSC as described previously.

Other access methods may be provided in the future, e.g., webpages for interactively browsing the data, or interfaces for downloading individual spectra or custom collections of

spectra. If and when these become available, they will be documented at <https://data.desi.lbl.gov/doc/access/>.

5.3. Tutorials

There is an internal effort within the DESI collaboration to design notebooks to help introduce specific data products or ways of accessing specific types of data. These are aggregated in a GitHub repository: <https://github.com/desihub/tutorials>. The tutorials are divided into thematic and topical subdirectories. Of most relevance is the `getting_started` subdirectory, which includes introductions to the types of files found in the EDR, and a notebook on working with the `zcatalog` files.

5.4. Data License and Acknowledgments

DESI data are released under the Creative Commons Attribution 4.0 International License.¹⁵⁵ This allows users to share, copy, redistribute, adapt, transform, and build upon the DESI data for any purpose, including commercially, as long as attribution is given by citing this paper and including the acknowledgments text listed at <https://data.desi.lbl.gov/doc/acknowledgments/>.

6. Conclusion

This paper describes the release of the first science data taken with the DESI instrument. This new sample consists of all commissioning and SV data taken between 2020 December 14, and 2021 June 10; with the majority of the data acquisition ending on 2021 May 13. These observations were taken to validate the survey design and observing strategy for the DESI Main Survey that commenced on 2021 May 14. The release includes deep spectra with robust visual inspection classification of 769 stars, 14,735 galaxies, and 3121 quasars from extended selection algorithms that were tested during the SV period. The release includes highly complete, good-quality, spectroscopic samples of 306,052 stars; 721,026 galaxies; and 44,151 quasars obtained over an area of roughly 170 deg^2 in the One-Percent Survey. In total, after accounting for additional spectra from secondary programs and all other DESI surveys, this release includes good calibrated spectra and catalog information for 496,128 stars; 1,125,635 galaxies; and 90,241 quasars that were spectroscopically classified and free of any known hardware, observational, or redshift fitting issues.

These data were all reprocessed with the DESI data reduction pipeline and redshift classification algorithms (S. J. Bailey et al. 2023, in preparation; Guy et al. 2023). Updated

¹⁵³ <https://globus.org>

¹⁵⁴ <https://astrosparcl.datalab.noirlab.edu>

¹⁵⁵ <https://creativecommons.org/licenses/by/4.0/>

versions are expected to make only minor changes to the quality of 1D spectra and redshift classifications.

The early data from DESI can be accessed as described in Section 5. Plots and key numbers in this paper were produced from notebooks and code in <https://github.com/desihub/edrpaper> using data from this EDR. The Digital Object Identifier (doi) for EDR is doi:10.5281/zenodo.7964161, which includes both the EDR data set and the data for the plots in this paper.

The redshift range, depth, and variety of spectroscopic targets make the data in this release an ideal sample for studies of stellar astrophysics, galaxy and quasar astrophysics, and early studies of the clustering of matter. Representing the range of potential studies, the DESI collaboration has already used these data to measure the 1D and 3D Ly α forest (Göksel Karaçaylı et al. 2023; Ramírez-Pérez et al. 2023; Ravoux et al. 2023), model the connection between galaxies and halos (Gao et al. 2023; Prada et al. 2023; Yu et al. 2023; Yuan et al. 2023), derive the probabilistic stellar mass functions from hundreds of thousands of BGS galaxies (Hahn et al. 2023), and identify very metal-poor stars in the Milky Way (Allende Prieto et al. 2023), among other topics.

The first year of the full 5 yr DESI survey concluded on 2022 June 13, and the DESI collaboration has finalized the internal data reductions for that sample. Those data will be publicly released after the completion and publication of the BAO and RSD measurements that motivated the construction of DESI. Meanwhile, DESI continues successful and efficient operations, planning its next major data sample when a third year of observation is complete. That 3 yr sample is expected to include more than 30 million spectroscopically confirmed galaxies and quasars, with a full 14,000 deg² footprint of the BGS and MWS programs. DESI will make the first year, the third year, and eventually its final sample publicly available following the release of the key cosmological analyses for each corresponding data set.

Acknowledgments

This material is based upon work supported by the U.S. Department of Energy (DOE), Office of Science, Office of High-Energy Physics, under contract No. DE-AC02-05CH11231, and by the National Energy Research Scientific Computing Center, a DOE Office of Science User Facility under the same contract. Additional support for DESI was provided by the U.S. National Science Foundation (NSF), Division of Astronomical Sciences under contract No. AST-0950945 to the NSF’s National Optical-Infrared Astronomy Research Laboratory; the Science and Technology Facilities Council of the United Kingdom; the Gordon and Betty Moore Foundation; the Heising-Simons Foundation; the French Alternative Energies and Atomic Energy Commission (CEA); the National Council of Science and Technology of Mexico (CONACYT); the Ministry of Science and Innovation of Spain (MICINN), and by the DESI Member Institutions: <https://www.desi.lbl.gov/collaborating-institutions>. Any opinions, findings, and conclusions or recommendations expressed in this material are those of the author(s) and do not necessarily reflect the views of the U.S. National Science Foundation, the U.S. Department of Energy, or any of the listed funding agencies.

The authors are honored to be permitted to conduct scientific research on Iolkam Du’ag (Kitt Peak), a mountain with particular significance to the Tohono O’odham Nation.

Facility: Mayall (DESI).

Software: astropy (Astropy Collaboration et al. 2013, 2018, 2022), healpy (Zonca et al. 2019), desispec (Guy et al. 2023), desitarget (Myers et al. 2023), Redrock (S. J. Bailey et al. 2023, in preparation).

Appendix A Primary Targets

This appendix includes tables for the primary targeting bits, some of which are replicated from Myers et al. (2023), for convenience, and described in Section 2.4.

A.1. Target Selection Validation (SV1) Targeting Bitmasks

Target Selection Validation (SURVEY=sv1) bitmasks are recorded in fibermap columns SV1_DESI_TARGET, SV1_BGS_TARGET, and SV1_MWS_TARGET. Table 10 lists the SV1_DESI_TARGET bits for dark-time targets, Table 11 lists the SV1_DESI_TARGET bits for general calibration targets such as standard stars and sky locations, Table 12 lists the SV1_BGS_TARGET bits for the BGS, and Table 13 lists the SV1_MWS_TARGET bits for MWS targets. These target selection bits are also defined programmatically in the open-source desitarget¹⁵⁶ software package. A YAML-format file describing the bits is in subdirectory py/desitarget/sv1/data/sv1_targetmask.yaml, with convenience wrapper objects in the Python module desitarget.sv1.sv1_targetmask.desi_mask. Examples of using these bitmasks with this code are given in Section 2 of Myers et al. (2023).

A.2. Operations Development (SV2) Targeting Bitmasks

The relevant targeting bits for Operations Development (SV2) are outlined in Table 14. Note that some targeting bits were retained moving from Target Selection Validation to SV2, and, therefore, only *new* bits and *changes* to existing bits are included in Table 14. The bitmask used to track SV2 subprograms is called sv2_desi_mask, and the bit-values for each SV2 target can be accessed via the SV2_DESI_TARGET, SV2_BGS_TARGET, and SV2_MWS_TARGET columns in data files (again, for more details, see Section 2.4 of Myers et al. 2023).

A.3. One-Percent Survey (SV3) Targeting Bitmasks

The relevant target selection bitmasks for the One-Percent Survey (SV3) are outlined in Table 15. Many targeting bits were retained moving from earlier phases of SV to the One-Percent Survey and, therefore, only *new* bits and *changes* to existing bits (when compared to Tables 10, 11, 12, 13, and 14) are included in Table 15. The bitmask used to track subprograms for the One-Percent Survey is called sv3_desi_mask, and the bit-values for each target can be accessed via the SV3_DESI_TARGET, SV3_BGS_TARGET, and SV3_MWS_TARGET columns in data files (again, for more details, see Section 2.4 of Myers et al. 2023).

¹⁵⁶ <https://github.com/desihub/desitarget>

Table 10
Dark-time Targeting Bits for SV1

Bit-name	Bit-value	Description
LRG	0	LRG
ELG	1	ELG
QSO	2	QSO
LRG_OPT	3	LRG from baseline version of optical cuts
LRG_IR	4	LRG from baseline version of IR cuts
LRG_SV_OPT	5	LRG from relaxed version of optical cuts
LRG_SV_IR	6	LRG from relaxed version of IR cuts
LOWZ_FILLER	7	LRG-like low- z filler sample (<i>not</i> used for SV1)
ELG_SV_GTOT	8	ELG from relaxed version of FDR ^a cuts and g -band magnitude limit
ELG_SV_GFIB	9	ELG from relaxed version of FDR ^a cuts and g -band fiber-magnitude limit
ELG_FDR_GTOT	10	ELG from FDR ^a cuts with g -band magnitude limit
ELG_FDR_GFIB	11	ELG from FDR ^a cuts with g -band fiber-magnitude limit
QSO_COLOR_4PASS	12	Low- z (tracer) QSO using color cuts
QSO_RF_4PASS	13	Low- z (tracer) QSO using random forest
QSO_COLOR_8PASS	14	High- z ($\text{Ly}\alpha$) QSO using color cuts
QSO_RF_8PASS	15	High- z ($\text{Ly}\alpha$) QSO using random forest
QSO_HZ_F	16	Faint, high-redshift QSO
QSO_Z5	17	$z \sim 5$ QSO
LRG_OPT_NORTH	18	LRG from baseline version of optical cuts tuned for Bok/Mosaic
LRG_IR_NORTH	19	LRG from baseline version of IR cuts tuned for Bok/Mosaic
LRG_SV_OPT_NORTH	20	LRG from relaxed version of optical cuts tuned for Bok/Mosaic
LRG_SV_IR_NORTH	21	LRG from relaxed version of IR cuts tuned for Bok/Mosaic
LOWZ_FILLER_NORTH	22	LRG-like low- z filler sample tuned for Bok/Mosaic (<i>not</i> used for SV1)
LRG_OPT_SOUTH	23	LRG from baseline version of optical cuts tuned for DECam
LRG_IR_SOUTH	24	LRG from baseline version of IR cuts tuned for DECam
LRG_SV_OPT_SOUTH	25	LRG from relaxed version of optical cuts tuned for DECam
LRG_SV_IR_SOUTH	26	LRG from relaxed version of IR cuts tuned for DECam
LOWZ_FILLER_SOUTH	27	LRG-like low- z filler sample tuned for DECam (<i>not</i> used for SV1)
ELG_SV_GTOT_NORTH	28	ELG from relaxed version of FDR ^a cuts and g -band limit for Bok/Mosaic
ELG_SV_GFIB_NORTH	29	As for ELG_SV_GTOT_NORTH but using a fiber-magnitude limit in g band
ELG_FDR_GTOT_NORTH	30	ELG from FDR ^a cuts with g -band magnitude limit for Bok/Mosaic
ELG_FDR_GFIB_NORTH	31	ELG from FDR ^a cuts with g -band fiber-magnitude limit for Bok/Mosaic
ELG_SV_GTOT_SOUTH	38	ELG from relaxed version of FDR ^a cuts and g -band magnitude limit for DECam
ELG_SV_GFIB_SOUTH	39	As for ELG_SV_GTOT_SOUTH but using a fiber-magnitude limit in g band
ELG_FDR_GTOT_SOUTH	40	ELG from FDR ^a cuts with g -band magnitude limit for DECam
ELG_FDR_GFIB_SOUTH	41	ELG from FDR ^a cuts with g -band fiber-magnitude limit for DECam
QSO_COLOR_4PASS_NORTH	42	Low- z (tracer) QSO using color cuts tuned for Bok/Mosaic
QSO_RF_4PASS_NORTH	43	Low- z (tracer) QSO using random forest tuned for Bok/Mosaic
QSO_COLOR_8PASS_NORTH	44	High- z ($\text{Ly}\alpha$) QSO using color cuts tuned for Bok/Mosaic
QSO_RF_8PASS_NORTH	45	High- z ($\text{Ly}\alpha$) QSO using random forest tuned for Bok/Mosaic
QSO_HZ_F_NORTH	46	QSO at high-redshift and faint tuned for Bok/Mosaic
QSO_Z5_NORTH	47	$z \sim 5$ QSO tuned for Bok/Mosaic
QSO_COLOR_4PASS_SOUTH	48	Low- z (tracer) QSO using color cuts tuned for DECam
QSO_RF_4PASS_SOUTH	53	Low- z (tracer) QSO using random forest tuned for DECam
QSO_COLOR_8PASS_SOUTH	54	High- z ($\text{Ly}\alpha$) QSO using color cuts tuned for DECam
QSO_RF_8PASS_SOUTH	55	High- z ($\text{Ly}\alpha$) QSO using random forest tuned for DECam
QSO_HZ_F_SOUTH	56	Faint, high-redshift QSO tuned for DECam
QSO_Z5_SOUTH	57	$z \sim 5$ QSO tuned for DECam

Notes. Bits are stored in the `sv1_desi_mask` and accessed via the `SV1_DESI_TARGET` column (see Myers et al. 2023, for more details).

^a “FDR” refers to the DESI Final Design Report (see DESI Collaboration et al. 2016a).

Table 11
SV1 Bits for Calibration, Object-avoidance, and to Indicate Non-dark-time Programs

Bit-name	Bit-value	Description
SKY	32	Blank sky locations
STD_FAINT	33	Standard stars for dark/gray conditions
STD_WD	34	White dwarf standard stars
STD_BRIGHT	35	Standard stars for bright conditions
BAD_SKY	36	Blank sky locations that are imperfect but still useable
SUPP_SKY	37	SKY is based on Gaia-avoidance (SKY will be set, too)
NO_TARGET	49	No known target at this location
BRIGHT_OBJECT	50	Known bright object to avoid
IN_BRIGHT_OBJECT	51	Too near a bright object; <i>do not observe</i>
NEAR_BRIGHT_OBJECT	52	Near a bright object but ok to observe
BGS_ANY	60	Any BGS bit is set (see Table 12)
MWS_ANY	61	Any MWS bit is set (see Table 13)
SCND_ANY	62	Any secondary bit is set (see Table 16)

Note. Bits are stored in the `sv1_desi_mask` and accessed via the `SV1_DESI_TARGET` column (see Myers et al. 2023, for more details). Additional standard star targets based purely on Gaia are included in Table 13.

Table 12
Bright Galaxy Survey (BGS) Targeting Bits for SV1

Bit-name	Bit-value	Description
BGS_FAINT	0	BGS faint targets
BGS_BRIGHT	1	BGS bright targets
BGS_FAINT_EXT	2	BGS faint extended targets
BGS_LOWQ	3	BGS low-quality targets
BGS_FIBMAG	4	BGS fiber-magnitude targets
BGS_FAINT_NORTH	8	BGS faint cuts tuned for Bok/Mosaic
BGS_BRIGHT_NORTH	9	BGS bright cuts tuned for Bok/Mosaic
BGS_FAINT_EXT_NORTH	10	BGS faint extended cuts tuned for Bok/Mosaic
BGS_LOWQ_NORTH	11	BGS low-quality cuts tuned for Bok/Mosaic
BGS_FIBMAG_NORTH	12	BGS low-quality cuts tuned for Bok/Mosaic
BGS_FAINT_SOUTH	16	BGS faint cuts tuned for DECam
BGS_BRIGHT_SOUTH	17	BGS bright cuts tuned for DECam
BGS_FAINT_EXT_SOUTH	18	BGS faint extended cuts tuned for DECam
BGS_LOWQ_SOUTH	19	BGS low-quality cuts tuned for DECam
BGS_FIBMAG_SOUTH	20	BGS fiber-magnitude cuts tuned for DECam
BGS_KNOWN_ANY	40	Known target from another survey
BGS_KNOWN_COLLIDED	41	BGS known SDSS/BOSS fiber collided
BGS_KNOWN_SDSS	42	BGS known SDSS targets
BGS_KNOWN_BOSS	43	BGS known BOSS targets

Note. Bits are stored in the `sv1_bgs_mask` and accessed via the `SV1_BGS_TARGET` column (see Myers et al. 2023, for more details).

Table 13
Milky Way Survey (MWS) Targeting Bits for SV1

Bit-name	Bit-value	Description
MWS_MAIN_BROAD	0	MWS magnitude-limited bulk sample
MWS_WD	1	MWS white dwarf target
MWS_NEARBY	2	MWS volume-complete (~ 100 pc) sample
MWS_MAIN_BROAD_NORTH	4	MWS targets from Bok/Mosaic
MWS_MAIN_BROAD_SOUTH	5	MWS targets from DECam
MWS_BHB	6	MWS blue horizontal branch targets
MWS_MAIN_FAINT	14	MWS magnitude-limited sample
MWS_MAIN_FAINT_NORTH	15	MWS magnitude-limited sample from Bok/Mosaic
MWS_MAIN_FAINT_SOUTH	16	MWS magnitude-limited sample from DECam
GAIA_STD_FAINT	33	Gaia-based standard stars for dark/gray conditions
GAIA_STD_WD	34	Gaia-based white dwarf stars for use as standards
GAIA_STD_BRIGHT	35	Gaia-based standard stars for bright conditions
BACKUP_BRIGHT	60	Bright backup Gaia targets
BACKUP_FAINT	61	Fainter backup Gaia targets
BACKUP_VERY_FAINT	62	Even fainter backup Gaia targets

Note. Bits are stored in the `sv1_mws_mask` and accessed via the `SV1_MWS_TARGET` column (see Myers et al. 2023, for more details). Gaia DR2 was used for target selection of Gaia targets during SV (Gaia Collaboration et al. 2018).

Table 14
Additional and Updated Targeting Bits for Operations Development (SV2)

Bit-name	Bit-value	Description
<i>Dark-time targeting bits in SV2_DESI_TARGET</i>		
QSO_HI_Z	4	QSO selected using high-redshift random forest
LRG_NORTH	8	LRG cuts tuned for Bok/Mosaic imaging data
ELG_NORTH	9	ELG cuts tuned for Bok/Mosaic imaging data
QSO_NORTH	10	QSO cuts tuned for Bok/Mosaic imaging data
LRG_SOUTH	16	LRG cuts tuned for DECam imaging data
ELG_SOUTH	17	ELG cuts tuned for DECam imaging data
QSO_SOUTH	18	QSO cuts tuned for DECam imaging data
<i>BGS targeting bits in SV2_BGS_TARGET</i>		
BGS_WISE	2	BGS targets selected using WISE imaging
BGS_FAINT_HIP	3	BGS faint targets prioritized like BGS_BRIGHT targets
BGS_WISE_NORTH	10	BGS_WISE cuts tuned for Bok/Mosaic imaging
BGS_WISE_SOUTH	18	BGS_WISE cuts tuned for DECam imaging
<i>MWS targeting bits in SV2_MWS_TARGET</i>		
MWS_BROAD	0	MWS magnitude-limited bulk sample
MWS_BROAD_NORTH	4	MWS cuts tuned for Bok/Mosaic imaging
MWS_BROAD_SOUTH	5	MWS cuts tuned for DECam imaging
MWS_MAIN_BLUE	8	MWS magnitude-limited blue sample
MWS_MAIN_BLUE_NORTH	9	MWS magnitude-limited blue sample tuned for Bok/Mosaic imaging
MWS_MAIN_BLUE_SOUTH	10	MWS magnitude-limited blue sample tuned for DECam imaging
MWS_MAIN_RED	11	MWS magnitude-limited red sample
MWS_MAIN_RED_NORTH	12	MWS magnitude-limited red sample tuned for Bok/Mosaic imaging
MWS_MAIN_RED_SOUTH	13	MWS magnitude-limited red sample tuned for DECam imaging

Note. Bits are stored in the `sv2_desi_mask` and accessed via the `SV2_DESI_TARGET` column (see Myers et al. 2023, for more details). Many bits from Tables 10, 11, 12, and 13 were reused for SV2, and only new or different bits are included in this table. For example, calibration bits listed in Table 11 remained the same moving from SV1 to SV2. Where the name and description of a bit-value has changed in this table compared to Tables 10, 11, 12, or 13, the bit was deprecated and updated for SV2.

Table 15
Additional and Updated Targeting Bits for SV3

Bit-name	Bit-value	Description
<i>Dark-time targeting bits</i>		
LRG_LOWDENS	3	LRG cuts to produce a lower-than-nominal ($\sim 600 \text{ deg}^{-2}$) target density
ELG_LOP	5	ELG scheduled for observations at lower priority
ELG_HIP	6	ELG scheduled for observations at higher priority
ELG_LOP_NORTH	11	ELG at lower priority tuned for Bok/Mosaic imaging
ELG_HIP_NORTH	12	ELG at higher priority tuned for Bok/Mosaic imaging
LRG_LOWDENS_NORTH	13	Lower-density LRG cuts tuned for Bok/Mosaic imaging
ELG_LOP_SOUTH	19	ELG at lower priority tuned for DECam imaging
ELG_HIP_SOUTH	20	ELG at higher priority tuned for DECam imaging
LRG_LOWDENS_SOUTH	21	Lower-density LRG cuts tuned for DECam imaging

Note. Bits are stored in the `sv3_desi_mask` and accessed via the `SV3_DESI_TARGET` column (see Myers et al. 2023, for more details). Many bits from Tables 10, 11, 12, 13, and 14 were reused for SV3, and only new or different bits are included in this table. For example, calibration, BGS, and MWS bits were not altered moving from SV2 to SV3. Where the name and description of a bit-value has changed in this table compared to Tables 10, 11, 12, 13, or 14, the bit was deprecated and updated for SV3.

Appendix B Secondary Targets

In addition to its primary science goals, the DESI survey incorporates a range of “secondary” targets to pursue bespoke research. In this appendix, we describe the secondary target campaigns included in the EDR and outline how the bit-values in their `scnd_mask` and `SCND_TARGET` column (see Section 2.4 of Myers et al. 2023) can be linked back to the relevant program.

DESI pursued secondary targets during both its “Target Selection Validation” and “One-Percent Survey” phases—which we refer to here as “SV1” and “SV3,” respectively, for consistency with how the bit-masks are named. In Table 16, we list the bit-names and bit-values for secondary targets that were scheduled during SV1. In Table 17, we indicate how these bits *changed* for SV3.¹⁵⁷ The target classes listed in Table 16 either were assigned to fill “spare” fibers on regular SV1 tiles or were assigned to their own “dedicated” campaign on custom tiles listed in Table 5. The targets that were intended for dedicated observations are marked with a * in Table 16. Almost all of the programs described in this appendix continue to be observed as part of the DESI Main Survey, although a few programs were changed to optimize targeting, and their bit-names were updated. The exceptions are as follows: `MWS_DDOGIANTS` and `VETO`, which were never actually observed; `GW190412` and `IC134191`, which were associated with specific fields of transients during SV; `MWS_CALIB` and `BACKUP_CALIB`, which were used specifically for calibrating targets for the SV1 stellar survey described in Cooper et al. (2023); and dedicated programs marked with a * in Table 16.

In the rest of this appendix, we outline each secondary target class, moving through the bit-names in Tables 16 and 17. Further details of the selection of each type of secondary target are available at the associated `docs` link for SV1¹⁵⁸ or SV3.¹⁵⁹ During SV1, secondary targets were permitted multiple observations. But, during SV3, most secondary targets were limited to a single observation, unless otherwise detailed below.

¹⁵⁷ Many bit-values were also deprecated moving from SV1 to SV3. So, some bits were set for *zero* targets for SV3.

¹⁵⁸ <https://data.desi.lbl.gov/public/ets/target/secondary/sv1/>

¹⁵⁹ <https://data.desi.lbl.gov/public/ets/target/secondary/sv3/>

B.1. VETO

This targeting bit was reserved to designate targets as unnecessary or problematic. In practice, `VETO` was never used, and, for later DESI programs, flagging targets as bad is done in the MTL ledgers described in Schlafly et al. (2023) instead.

B.2. UDG

This program was designed to obtain redshifts for, and hence distances to, a sample drawn from the few thousand known ultradiffuse galaxies (UDGs) across the entire DESI footprint ($\sim 0.5 \text{ deg}^{-2}$; Zaritsky et al. 2019, 2022). The targeted UDGs were field galaxies selected in sparse environments using imaging from the Legacy Survey. Such galaxies are expected to be among the least efficient large galaxies hitherto known. Their distances are essential for understanding their environments, and inferring their sizes and luminosities. Because the bluest UDGs in the field are expected to have emission lines that DESI could detect (see, e.g., Kadowaki et al. 2021), the sample was limited to $g - r < 0.3$.

B.3. FIRST_MALS

This project followed up sources from the MeerKAT Absorption Line Survey (MALS; see, e.g., Gupta et al. 2016), an *L*- and UHF-band survey targeting $\sim 150,000$ radio-loud AGN. In the DESI footprint, $\sim 60\%$ ($\sim 6 \text{ deg}^{-2}$) of these AGN are expected to have optical counterparts to $r < 23$. The project sought to obtain optical spectra for sources that have 21 cm and OH absorption spectra from MALS. The main goals were to help to characterize the redshift distribution of MALS AGN and intervening and associated absorption systems, to quantify biases due to dust in optically selected AGN samples, and to facilitate photometric redshift estimates for larger radio-selected samples.

B.4. WD_BINARIES

This targeting bit was only briefly used for observations associated with version 0.48.0 of the `desitarget` code before being replaced by `WD_BINARIES_BRIGHT` and `WD_BINARIES_DARK` (see Section B.31 for a more detailed description).

Table 16
Secondary Targeting Bits for SV1

Bit-name	Bit-value	Bit-name	Bit-value	Bit-name	Bit-value
VETO	0	DC3R2_GAMA	20	BRIGHT_HPM	40
UDG	1	UNWISE_BLUE ^a	21	WD_BINARIES_BRIGHT	41
FIRST_MALS	2	UNWISE_GREEN ^a	22	WD_BINARIES_DARK	42
WD_BINARIES	3	HETDEX_MAIN ^a	23	DESILBG ^a	43
LBG_TOMOG ^a	4	HETDEX_HP ^a	24	LBG_TOMOG_XMM ^a	44
QSO_RED	5	PSF_OUT_BRIGHT	25	LBG_TOMOG_COSMOS ^a	45
M31_KNOWN ^a	6	PSF_OUT_DARK	26	LBG_TOMOG_W3 ^a	46
M31_QSO ^a	7	HPM_SOUM	27	UNWISE_GREEN_II_3700 ^a	47
M31_STAR ^a	8	SN_HOSTS	28	UNWISE_GREEN_II_3800 ^a	48
MWS_DDOGIANTS	9	GAL_CLUS_BCG	29	UNWISE_GREEN_II_3900 ^a	49
MWS_CLUS_GAL_DEEP ^a	10	GAL_CLUS_2ND	30	UNWISE_GREEN_II_4000 ^a	50
LOW_MASS_AGN	11	GAL_CLUS_SAT	31	UNWISE_BLUE_FAINT_II ^a	51
FAINT_HPM	12	HSC_HIZ_SNE ^a	32	UNWISE_BLUE_BRIGHT_II ^a	52
GW190412	13	ISM_CGM_QGP ^a	33	DESILBG_TMG_FINAL ^a	53
IC134191	14	STRONG_LENS	34	DESILBG_G_FINAL ^a	54
PV_BRIGHT	15	WISE_VAR_QSO	35	DESILBG_BXU_FINAL ^a	55
PV_DARK	16	MWS_CALIB	36	LBG_TOMOG_COSMOS_FINAL ^a	56
LOW_Z	17	BACKUP_CALIB	37	BRIGHT_TOO	60
BHB	18	MWS_MAIN_CLUSTER_SV	38	DARK_TOO	61
SPCV	19	MWS_RRLYR	39

Notes. These bits are taken from the `desitarget` code (see https://github.com/desihub/desitarget/blob/2.5.0/py/desitarget/sv1/data/sv1_targetmask.yaml#L155-L226) and are described in the body of the Appendix.

^a A dedicated target class intended to be observed on custom tiles.

Table 17
Updates to Secondary Targeting Bits for SV3

Bit-name	Bit-value	Bit-name	Bit-value	Bit-name	Bit-value
LOW_Z_TIER1	15	PV_BRIGHT_MEDIUM	44	BRIGHT_TOO_LOP	59
LOW_Z_TIER2	16	PV_BRIGHT_LOW	45	BRIGHT_TOO_HIP	60
LOW_Z_TIER3	17	PV_DARK_HIGH	46	DARK_TOO_LOP	61
Z5_QSO	36	PV_DARK_MEDIUM	47	DARK_TOO_HIP	62
PV_BRIGHT_HIGH	43	PV_DARK_LOW	48

Note. These bits are taken from the `desitarget` code (see https://github.com/desihub/desitarget/blob/2.5.0/py/desitarget/sv3/data/sv3_targetmask.yaml#L132-L173) and are described in the body of the Appendix. In addition to the changes listed in the table, many bits from SV1 were not retained or set in SV3.

B.5. LBG_TOMOG

This campaign requested ~ 10 hr of dedicated dark time on a single DESI tile in the COSMOS or XMM-LSS fields of the CFHT Large Area U -band Deep Survey (CLAUDS; Sawicki et al. 2019) to target ~ 4500 Lyman break galaxies (LBGs) and quasars in the redshift range $2 < z < 3.5$. A major goal was to map the Ly α forest in detail by creating a 3D tomographic map of neutral hydrogen absorption (see, e.g., Ravoux et al. 2020). Additional goals included finding high-redshift protoclusters and voids. Quasars were targeted to $r \lesssim 23.5$ using the standard DESI targeting approach (Chaussidon et al. 2023), and LBGs were selected to $r \lesssim 24.5$ using a U -dropout method applied to the CLAUDS imaging catalogs. The LBG_TOMOG bit was used in files associated with versions 0.48.0, 0.49.0, 0.50.0, and 0.51.0 of the `desitarget` code but was gradually deprecated by the LBG_TOMOG_XMM, LBG_TOMOG_COSMOS, LBG_TOMOG_W3, and LBG_TOMOG_COSMOS_FINAL bits (see Section B.33).

B.6. QSO_RED

The QSO_RED sample targeted mildly dusty quasars that are too red to meet standard DESI criteria. The project sought to

ascertain whether obscuration in quasars is explained by viewing the broad-line region through a dusty torus at a grazing angle or by an early, dusty phase in the lifetime of quasars (see, e.g., Fawcett et al. 2020). The QSO_RED targets were selected from point sources in Legacy Survey's imaging using the Wide-field Infrared Survey Explorer (WISE) W1W2W3 color wedge of Mateos et al. (2012). Targets consistent with the “bluer” colors of existing DESI quasar targets (Chaussidon et al. 2023) were removed, producing a sample of $\sim 41,000$ QSO_RED targets over the DESI footprint ($\sim 3 \text{ deg}^{-2}$). As with all quasar-like target classes throughout the DESI survey (see Section 5 of Schlafly et al. 2023), QSO_RED sources were scheduled for four total observations (starting with SV3).

B.7. M31_KNOWN, M31_QSO, M31_STAR

The DESI Andromeda Region Kinematic (“DARK”) survey comprised three complementary programs aimed at studying the dynamics of our nearest large neighbor galaxy. The M31_KNOWN bit covered previously identified, bright targets—such as objects from the SPLASH survey (Dorman et al. 2012), GCs, HII regions, planetary nebulae, and variable sources. The M31_QSO bit flagged quasar targets behind M31 selected using

Gaia and WISE. The `M31_STAR` bit indicated sources selected from a combination of PAndAS (McConnachie et al. 2018), Gaia, and WISE. The dedicated observations of, and scientific results from, the DARK survey are detailed in Dey et al. (2023).

B.8. `MWS_DDOGIANTS`

The `MWS_DDOGIANTS` targeting bit was ultimately never used by DESI.

B.9. `MWS_CLUS_GAL_DEEP`

This campaign requested dedicated dark-time tiles to obtain spectra of open clusters, GCs, and dwarf spheroidal galaxies in the outskirts of our Galaxy. A major goal was to combine radial velocities with Gaia astrometry for faint ($19 < r < 21$) stars to constrain cluster membership and measure chemical abundances. Ultimately, the program aimed to characterize the initial mass function for clusters, the kinematics of stellar streams associated with GCs, and density profiles for dwarf spheroidals. Targets were selected using Legacy Survey's imaging and Gaia astrometry at a density of a few thousand per DESI tile.

B.10. `LOW_MASS_AGN`

The `LOW_MASS_AGN` program targeted faint ($r > 20$), low-redshift AGN in dwarf galaxies, selected using optical and infrared photometry from the eighth data release of the Legacy Surveys (LS DR8). The targets were preselected to be at low redshift ($0.02 \leq z_{\text{phot}} \leq 0.3$) based on photometric redshifts from Zhou et al. (2021), and to have faint z -band absolute magnitude ($M_z \gtrsim 21$), which was adopted as a proxy for stellar mass. Candidates were then targeted as AGN on the basis of their $z - W1$, $W1 - W2$, and $W2 - W3$ colors, resulting in a sample with a density of $\sim 20 \text{ deg}^{-2}$. The main scientific goal of the `LOW_MASS_AGN` program was to identify ~ 100 AGN driven by intermediate mass ($\lesssim 10^6 M_\odot$) black holes (see, e.g., Mezcuca & Domínguez Sánchez 2020). The program also aimed to test the validity of a new AGN selection criterion similar to that from Hviding et al. (2022), and extend it to low-mass galaxies for which the application of infrared AGN diagnostics is debated (Hainline et al. 2016; Satyapal et al. 2018).

B.11. `FAINT_HPM`, `BRIGHT_HPM`

The HPM project sought to measure radial velocities and spectroscopic types for ~ 1000 faint, high-proper-motion stars drawn from Gaia and the NOIRLab Source Catalog (NSC; Nidever et al. 2018, 2021). Targets were selected based on high proper motion ($\mu > 100 \text{ mas yr}^{-1}$), supplemented with reliable parallax measurements from Gaia and red colors from WISE and NSC. The assembled sample—extending to $G \sim 21$ (Gaia) and $r \sim 23$ (NSC)—was designed to find and study ejected white dwarfs (from double-degenerate binaries), ancient white and brown dwarfs, and hypervelocity stars. Fainter candidates were observed in dark time (`FAINT_HPM`), and brighter candidates were observed in bright time (`BRIGHT_HPM`).

B.12. `GW190412`, `IC134191`

These bits were intended to be used for dedicated, rapid-turnaround observations of DESI ToOs in the vicinity of a gravitational wave signal or an IceCube high-energy neutrino

event. The archival gravitational wave alert chosen to mimic a real trigger was GW190412 (Abbott et al. 2020), and a real-time follow-up was performed for the “gold” neutrino event 134191_17593623.¹⁶⁰ GW190412 and IC134191 targets were assigned in some files associated with versions 0.48.0, 0.49.0, and 0.50.0 of the `desitarget` code. The follow-up of GW190412 was performed 2 yr after the gravitational wave event, since gravitational wave detectors were not operating during SV, both as a test and to provide spectroscopic redshifts for a standard siren measurement (Palmese et al. 2021b). On the other hand, real time follow-up of ToOs by DESI (e.g., Palmese et al. 2021a) was achieved by prioritizing tiles near IC134191 during afternoon planning (see Schlafly et al. 2023) or by assigning the `BRIGHT_TOO_LOP`, `BRIGHT_TOO_HIP`, `DARK_TOO_LOP`, and `DARK_TOO_HIP` bits discussed in Section B.40.

B.13. `PV_BRIGHT`, `PV_DARK`

The low-redshift ($z < 0.15$) DESI Peculiar Velocity (PV) Survey was designed to improve constraints on the growth rate of structure (see, e.g., Howlett et al. 2017; Kim & Linder 2020). The survey comprised three samples (see, e.g., Saulder et al. 2023). First, the fundamental plane (“FP”) sample, which included bright ($r < 18$), elliptically shaped, galaxies, helps characterize the fundamental plane. Second, the Tully-Fisher (“TF”) sample, which included locations along the major axes of SGA galaxies (J. Moustakas et al. 2023, in preparation) with spiral-like colors, probes the TF relation. Third, the “extended” sample, which covered positions across the surfaces of large ($> 2 \times 1/4$) SGA galaxies, fills in areas that have no primary DESI science targets due to fiber-patrol limitations. The `PV_BRIGHT` targets were observed in bright time, and included TF and “extended” targets. The `PV_DARK` sample was observed in dark time, and included FP and TF targets.

B.14. `LOW_Z`

This campaign used imaging and photometric data from the Legacy Surveys to identify moderately faint ($19 < r < 21$) very-low-redshift ($z < 0.03$) galaxies. The target space was constrained using cuts on surface brightness and color adapted from the SAGA Survey (Geha et al. 2017; Mao et al. 2021) with minor adjustments. A machine-learning method (convolutional neural network; see Wu et al. 2022) was applied to prioritize the selection of most likely nearby galaxy candidates. The science goals included refining the luminosity function of dwarf galaxies and a census of possible gravitational wave hosts in the local Universe. The `LOW_Z` survey was designed as a “filler” class of several hundred targets per square degree, scheduled at a very low priority. The campaign is detailed in Darragh-Ford et al. (2022).

B.15. `BHB`

The BHB sample extended the MWS blue horizontal branch program (Cooper et al. 2023) to fainter ($19 < g < 21$) targets that required dark-time observations. The BHB sample was designed to probe stellar populations and kinematics at distances of $\sim 150 \text{ kpc}$ to constrain the dark matter mass distribution in the outermost galaxy. Targets were color-selected at a (subsampling) density of $\sim 2 \text{ deg}^{-2}$ using a

¹⁶⁰ See, e.g., https://gcn.gsfc.nasa.gov/amon_icecube_gold_bronze_events.html.

combination of $g-r$ and $r-z$ from the Legacy Surveys (similar to, e.g., Li et al. 2019) to separate BHB stars from blue stragglers, quasars, and white dwarfs. Further cuts on WISE W1 and Gaia G were applied to remove residual quasars. A few targets from RR Lyrae catalogs derived by the Gaia collaboration or Sesar et al. (2017) were included in the BHB sample.

B.16. SPCV

This project aimed to catalog—and obtain multiepoch spectra of—short-period cataclysmic variable stars (spCVs). Science goals included characterizing sources in the “cataclysmic variable period gap” of $\sim 2\text{--}3$ hr (e.g., Knigge et al. 2011), and finding reference spCVs for the *LISA* mission to use as verification binaries (e.g., Cornish & Robson 2017). Targets were selected using Gaia colors combined with variability amplitudes of >0.25 in Gaia G (see Abrahams et al. 2020). The resulting sample was limited to $16 < G < 21$, producing ~ 1300 candidate spCVs spread across the Milky Way.

B.17. DC3R2_GAMA

Spectra were obtained to characterize the relation between *ugriZYJHK* multicolor and redshift for photo- z calibration across $\approx 50\%$ of the color space visible to the Vera C. Rubin Observatory’s LSST (Ivezić et al. 2019) and Euclid (Euclid Collaboration et al. 2022). Targets were selected from public KiDS+VIKING optical-NIR imaging (Kuijken et al. 2019; Wright et al. 2019) in the GAMA 9, 12, and 15 hr equatorial fields at $z_{\text{fiber}} < 22.1$ and assigned to the self-organizing map of the C3R2 survey (Masters et al. 2017, 2019) transformed to KiDS-VIKING color space. From these, a sample of 13,270 spectra from 10,376 unique targets was observed on dedicated tiles 80971–80975. Targets were prioritized to maximize the ability to constrain the slope of redshift with respect to magnitude at fixed color, which is a main uncertainty of the C3R2 approach for direct calibration of redshift distributions for faint photometric galaxy samples. Some additional DC3R2_GAMA targets were observed using spare fibers during the course of SV. The first results from this campaign are presented in J. McCullough et al. (2023, in preparation).

B.18. UNWISE_BLUE, UNWISE_GREEN

This dedicated dark-time program was designed to calibrate the redshift distribution of galaxies for cosmic microwave background (CMB) lensing tomography measurements. Targets were randomly subselected from the “blue” (UNWISE_BLUE) and “green” (UNWISE_GREEN) samples of Krolewski et al. (2020), which were derived from W1 – W2 color cuts in the unWISE catalog of Schlafly et al. (2019). The $6''$ WISE PSF is too broad to reliably center DESI fibers on the galaxy of interest, so targets were additionally matched to the nearest Subaru HSC imaging (with a $2''/75$ radius) and limited to $y < 22.5$ ($y < 24$) for the blue (green) sample, resulting in ~ 9000 (~ 4500) UNWISE_BLUE (UNWISE_GREEN) targets. The main goal of the program was to improve cosmological constraints from Planck-unWISE lensing measurements by reducing the uncertainty in the unWISE redshift distribution, a primary contributor to S_8 uncertainty (see, e.g., Krolewski et al. 2021). This program was refined in later iterations of SV1—files associated with versions 0.51.0 and 0.52.0 of the *desitarget* code were supplemented with the additional bits listed in Section B.34.

B.19. HETDEX_MAIN, HETDEX_HP

The HETDEX dedicated dark-time campaign pursued higher-resolution spectra of a few thousand Ly α emitters (LAEs) from the Hobby–Eberly Telescope Dark Energy Experiment (Gebhardt et al. 2021). HETDEX targets LAEs in the redshift range $1.9 \lesssim z \lesssim 3.5$, but its relatively meager spectral resolution (~ 800 ; Hill et al. 2021) spawns contamination by low-redshift [O II] emitters. The DESI observations sought to characterize this contamination, while also preparing for future DESI-like experiments using LAEs. HETDEX_MAIN targeted HETDEX sources with spectral S/N > 5.2 , supplemented by a few hundred lower-significance emitters. HETDEX_HP targets comprised a few dozen faint, high-redshift LAEs to help characterize DESI detection limits for HETDEX sources.

B.20. PSF_OUT_BRIGHT, PSF_OUT_DARK

The PSF outliers campaign targeted point sources (TYPE=="PSF") in the Legacy Surveys that lie more than 10σ from the stellar locus in grz (in the spirit of, e.g., Covey et al. 2007). The PSF_OUT_BRIGHT (PSF_OUT_DARK) targets were intended for bright-time (dark-time) observations and were limited to $15 < r < 19$ ($16 < r < 22$). The program was designed as a “filler” survey—it comprised a little more than 100 total targets per square degree and was scheduled at very low priority to mop up spare fibers. The true target density was lower as $\sim 80\%$ of outliers from the stellar locus—such as candidate quasars, white dwarfs, and compact galaxies—were already targeted by DESI.

B.21. HPM_SOUM

The HPM_SOUM survey pursued spectroscopy of high proper-motion stars across the DESI footprint. The scientific goals of the program were similar to those for the FAINT_HPM campaign (see Section B.11). The target list comprised ~ 2900 faint ($r > 19.5$) stars with high proper motion ($\gtrsim 200$ mas yr $^{-1}$). These targets were drawn from the sample of Segev & Ofek (2019), which derived proper motions by comparing the positions of sources between the SDSS and Pan-STARRS1.

B.22. SN_HOSTS

This program targeted $\sim 20,000$ supernova hosts and nuclear variables from the Nearby Supernova Factory (e.g., Aldering et al. 2002), Palomar Transient Factory (e.g., Law et al. 2009), SDSS-II Supernova Survey (Frieman et al. 2008), and Zwicky Transient Factory (e.g., Bellm et al. 2019; Fremling et al. 2020). DESI spectroscopy is particularly warranted as the Zwicky Transient Facility “spectral energy distribution machine” (Blagorodnova et al. 2018) can only obtain low-resolution ($R \sim 100$) spectra. As about half of the SN_HOSTS data set was already targeted by the DESI BGS, the true SN_HOSTS sample only comprised $\sim 10,000$ targets. Scientific goals included probing correlations between the properties of supernovae and their host galaxies; improving cosmological constraints from supernovae; using direct, supernova-based distance measurements to characterize PVs and the fundamental plane of host galaxies; and enhancing populations of changing-look AGN and tidal disruption events.

B.23. GAL_CLUS_BCG, GAL_CLUS_2ND, GAL_CLUS_SAT

This dark-time campaign sought to build a volume-complete sample of galaxy clusters with spectroscopically confirmed members. Targets were compiled from galaxies with a probability of cluster membership of $P_{\text{mem}} > 0.90$ in version 6.3 of the SDSS redMaPPer catalog (see, e.g., Rykoff et al. 2014). The GAL_CLUS_BCG bit denotes brightest cluster galaxies—i.e., the redMaPPer most-probable central galaxy—to a redshift of $z < 0.35$. The GAL_CLUS_SCND bit signifies the *second* brightest cluster member candidate. The GAL_CLUS_SAT bit denotes all other ($P_{\text{mem}} > 0.90$) candidate cluster members to $z < 0.30$. GAL_CLUS_BCG targets were prioritized for DESI observations over GAL_CLUS_2ND, which were in turn prioritized over GAL_CLUS_SAT targets. After removing existing DESI targets, the sample comprised a few 100 (each) GAL_CLUS_BCG and GAL_CLUS_SCND targets and $\sim 10,800$ GAL_CLUS_SAT targets.

B.24. HSC_HIZ_SNE

This dedicated dark-time program focused on obtaining redshifts for supernova host galaxies identified in a deep-cadenced HSC survey in the COSMOS field (see Yasuda et al. 2019). The target sample consisted of 1036 supernova candidates (out of the 1824 candidates detailed in Yasuda et al. 2019) that lacked spectroscopy when the HSC_HIZ_SNE observations were proposed. A little more than 400 of these candidates were expected to be cosmologically important Type Ia supernovae. The main scientific goal of this program was to double the number of known Type Ia supernovae at redshifts of $z > 1$ and hence improve constraints on the dark energy equation of state.

B.25. ISM_CGM_QGP

The ISM_CGM_QGP campaign sought to probe the circumgalactic medium (CGM) by targeting 114 quasars ($S/N > 3$) with sight lines that pass within $30''$ (~ 250 kpc at $z = 2.0$) of a galaxy in the COSMOS (Laigle et al. 2016) or HSC Ultra-Deep (Aihara et al. 2018b) fields. Targets were selected from SDSS DR14 quasars (Pâris et al. 2018) with $g < 22$. The cool gas galaxy counterparts are selected from the COSMOS2020 catalog (Weaver et al. 2022). The main goals of the program (see also Zou et al. 2023) were to probe the metal budget in the CGM, and to characterize how the CGM is influenced by the properties of proximate galaxies.

B.26. STRONG_LENS

This program sought to obtain redshifts for strong gravitational lenses identified in DESI Legacy Survey's imaging (see Huang et al. 2020, 2021). The brightest image of each lensed source and $\sim 20\%$ of putative lensing galaxies were scheduled for observations, resulting in a total sample of 3588 targets spread throughout the DESI footprint. The main purpose of obtaining spectroscopic redshifts for the STRONG_LENS sample was to improve lensing models for these systems. Scientific goals included probing dark matter halo density profiles and subhalo abundances, and identifying superior systems to search for multiply imaged supernovae.

B.27. WISE_VAR_QSO

The WISE_VAR_QSO bit denotes quasar targets selected via variability estimated using the WISE “light curve sweeps” supplied with DR9 of the Legacy Surveys.¹⁶¹ The selection technique was based on cuts in structure–function-space (represented by the parameters A and γ) in a similar fashion to those from Myers et al. (2015; see Section 4.2.1) and Palanque-Delabrouille et al. (2011). The resulting target density was a little more than 100 deg^{-2} across most of the DESI footprint. As with all quasar-like classes throughout the DESI survey (see Section 5 of Schlafly et al. 2023), WISE_VAR_QSO targets were scheduled for four total observations (starting with SV3). The main goal of the WISE_VAR_QSO sample was to expand the pool of quasars recovered by DESI that could be used for studies of the Ly α forest.

B.28. MWS_CALIB, BACKUP_CALIB

These target classes indicate calibration sources that were adopted for the SV1 stellar survey described in Cooper et al. (2023). MWS_CALIB and BACKUP_CALIB targets were selected from publicly available survey catalogs (e.g., SDSS Segue, APOGEE, GALAH, and the Gaia ESO Survey). BACKUP_CALIB targets were limited to the magnitude range $10 < G < 16$, and MWS_CALIB targets were limited to $16 < G < 19$.

B.29. MWS_MAIN_CLUSTER_SV

This class flags targets observed as part of the SV1 stellar survey described in Cooper et al. (2023). Targets were selected to be “likely” members of Milky Way GCs. “Likely,” here, corresponds to a membership probability of $P > 0.3$, with P as defined in Vasiliev & Baumgardt (2021). Targets were limited to a magnitude range of $16 < G < 20$.

B.30. MWS_RRLYR

This target class formed part of the SV1 stellar survey described in Cooper et al. (2023). The selection targets stars that are likely RR Lyrae variables based on Gaia DR2. It combines sources that were labeled as RR Lyrae by the Specific Object Study pipeline (Clementini et al. 2019) and the general variability processing pipeline (Holl et al. 2018), limited to $14 < G < 19$. The sample can be reproduced by running the following Gaia archival query: WITH x as (SELECT vari_classifier_result.source_id FROM gaia_dr2.vari_classifier_result WHERE vari_classifier_result.best_class_name :: text "RR%" :: text UNION SELECT vari_rrlyrae.source_id FROM gaia_dr2.vari_rrlyrae) SELECT g.* FROM gaia_dr2.gaia_source as g, x where g.source_id=x.source_id and phot_g_mean_mag between 14 and 19;

B.31. WD_BINARIES_BRIGHT, WD_BINARIES_DARK

This campaign pursued a representative sample of all types of white dwarf binaries. The broad scientific focus was to characterize the entire dynamical range of bound white dwarfs, from intrinsically bright, high-mass transfer binaries to extremely

¹⁶¹ <https://www.legacysurvey.org/dr9/files/#light-curve-sweeps-9-0-lightcurves-sweep-brickmin-brickmax-lc-fits>

faint, highly evolved systems. The targets were selected by cross-matching the Galaxy Evolution Explorer (GALEX) source catalog with Gaia and retaining sources with an absolute magnitude of $M_{\text{FUV}} > 1.5(\text{FUV} - G) - 0.3$, which generally lie below the main sequence. Here, M_{FUV} is calculated using distances derived from Gaia parallaxes that are measured to $\geq 5\sigma$, and far-UV (FUV) and G represent magnitudes in GALEX FUV and Gaia G band. After removing existing DESI targets, this sample comprised $\sim 28,300$ (~ 7400) sources with $16 \leq G \leq 18$ ($G > 18$). The brighter (fainter) of these subsamples is signified using the `WD_BINARIES_BRIGHT` (`WD_BINARIES_DARK`) bit and scheduled for observations in a bright (dark) time.

B.32. `DESILBG`

This project sought ~ 10 hr of dedicated dark-time observations in fields covered by CLAUDS (Sawicki et al. 2019). By supplementing CLAUDS with deep grz imaging from HSC, the project aimed to target ~ 5000 LBGs and LAEs in the redshift range $2 < z < 4$. The main goal was to prepare for future DESI-like experiments by characterizing a population of high-density, high-redshift tracers with which to improve cosmological constraints at times before the dark energy began to dominate the Universe. Three different approaches were adopted to target redshifts near $z \sim 2$ (the BX technique, see, e.g., Adelberger et al. 2004) and $z \sim 3-4$ (u - and g -dropout techniques, see., e.g., Hildebrandt et al. 2009). The `DESILBG` bit was not introduced until version 0.51.0 of the `desitarget` code, and it was rapidly replaced by the bits described in Section B.35.

B.33. `LBG_TOMOG_XMM`, `LBG_TOMOG_COSMOS`, `LBG_TOMOG_W3`, `LBG_TOMOG_COSMOS_FINAL`

These targeting bits denote updates to the `LBG_TOMOG` program described in Section B.5. Overall, the science program remained the same, but the selection was tweaked slightly, or applied in a new field, as outlined at each bit's `docs` link (see the introduction to this appendix). The `LBG_TOMOG_XMM` and `LBG_TOMOG_W3` bits were introduced in version 0.51.0 of the `desitarget` code (and targeting files) and were also populated in version 0.52.0. The `LBG_TOMOG_COSMOS` bit was introduced in 0.51.0 and quickly deprecated in favor of the `LBG_TOMOG_COSMOS_FINAL` bit for 0.52.0.

B.34. `UNWISE_GREEN_II_3700`, `UNWISE_GREEN_II_3800`, `UNWISE_GREEN_II_3900`, `UNWISE_GREEN_II_4000`, `UNWISE_BLUE_FAINT_II`, `UNWISE_BLUE_BRIGHT_II`

These bits were introduced in version 0.51.0 of the `desitarget` code to augment the `UNWISE_BLUE` and `UNWISE_GREEN` targets. The science goals outlined in Section B.18 were unchanged, but adding bits facilitated a finer-grained control of how targets were prioritized for DESI observations. The `UNWISE_GREEN_II_4000` targets were assigned the highest priority, followed, in order, by `UNWISE_GREEN_II_3900`, `UNWISE_GREEN_II_3800`, `UNWISE_GREEN_II_3700`, `UNWISE_BLUE_FAINT_II`, and, finally, `UNWISE_BLUE_BRIGHT_II` at the lowest priority. The `UNWISE_BLUE_BRIGHT_II` and `UNWISE_BLUE_FAINT_II` targets were split at a Legacy Survey's fiber magnitude of $z_{\text{fiber}} = 21.1$. The green targets were split using WISE colors according to $W1 - W2 < 0.8$, $W1 < 17.0$

(`UNWISE_GREEN_II_4000`); $W1 - W2 < 0.8$, $W1 < 17.2$ (`UNWISE_GREEN_II_3900`); and $W1 - W2 < 0.8$ (`UNWISE_GREEN_II_3800`); with remaining sources from the original `UNWISE_GREEN` selection signified by `UNWISE_GREEN_II_3700`. The split in the blue sample allowed for longer exposure times on faint targets, whereas the split in the green sample deprioritized galaxies at $z > 1.6$, where the redshift completeness is poor due to the [O II] line and 4000 Å break redshifting out of the DESI wavelength range.

B.35. `DESILBG_TMG_FINAL`, `DESILBG_G_FINAL`, `DESILBG_BXU_FINAL`

Starting with version 0.52.0 of the `desitarget` code, the `DESILBG` sample was split into several subsamples to make it easier to track the provenance of each targeting approach described in Section B.32. The BX selection (using the BX technique, see, e.g., Adelberger et al. 2004) and u -dropout targets were signified by the `DESILBG_BXU_FINAL` bit; the g -dropouts were signified by the `DESILBG_G_FINAL` bit; and a new selection that resembled the `LBG_TOMOG` target class outlined in Section B.5 was built. A detailed code to derive each of these subsamples is available on GitHub.¹⁶²

B.36. `BRIGHT_TOO`, `DARK_TOO`

These target classes were intended to flag general ToOs during the SV1 phase of DESI. In actuality, ToOs were not tracked until SV3, and these bits were replaced by the bits described in Section B.40.

B.37. `LOW_Z_TIER1`, `LOW_Z_TIER2`, `LOW_Z_TIER3`

When DESI moved to its SV3 phase, the `LOW_Z` targets described in Section B.14 were split into three tiers to allow different target classes to be assigned different observational priorities. The highest-priority targets (`LOW_Z_TIER1`) contain the most likely low-redshift candidates based on the prediction of a machine-learning method (convolutional neural network; see Wu et al. 2022). The next-highest-priority targets (`LOW_Z_TIER2`) comprised objects that are in a tighter photometric space where most low-redshift candidates are situated (as introduced in Mao et al. 2021). The `LOW_Z_TIER2` sample was designed to *not* overlap with BGS targets. Finally, the lowest-priority targets (`LOW_Z_TIER3`) were based on the remaining targets within the overall photometric cuts (referred to as “ $z < 0.03$ -complete cuts” in Darragh-Ford et al. 2022). The `LOW_Z_TIER3` sample was allowed to overlap with BGS targets. Again, see Darragh-Ford et al. (2022) for a full description of the `LOW_Z` program.

B.38. `Z5_QSO`

The `Z5_QSO` program targeted quasars at redshifts of $5.0 \lesssim z \lesssim 6.5$ based on color cuts applied to Legacy Survey's imaging ($grzW1W2$) supplemented by i and y bands from Pan-STARRS1 (see, e.g., Wang et al. 2017; Yang et al. 2019). Where available, J band from public NIR surveys was also incorporated to reject stellar contaminants. The main color criteria, which are detailed in Yang et al. (2023), produce a target sample with a density of $\sim 0.5 \text{ deg}^{-2}$. The science goals included constraining the quasar luminosity function at high

¹⁶² See <https://github.com/michaeljwilson/DESILBG/blob/1.0.2/gold/README>.

redshift, building a sample to study the intergalactic medium near the epoch of reionization, and probing super-massive black hole growth in the early Universe. As with all DESI quasar-like targets (see Section 5 of Schlafly et al. 2023), the Z5_QSO sample was scheduled for four total observations.

*B.39. PV_BRIGHT_HIGH, PV_BRIGHT_MEDIUM,
PV_BRIGHT_LOW, PV_DARK_HIGH, PV_DARK_MEDIUM,
PV_DARK_LOW*





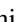




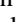




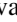








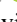









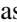



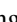


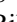



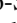




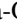



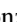

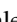


Starting with SV3, the PV_BRIGHT and PV_DARK samples described in Section B.13 were split into three subclasses (each) to facilitate them being scheduled for observations at different priorities (for details, see Table 1 of Saulder et al. 2023). Broadly, the highest-priority targets (PV_BRIGHT_HIGH, PV_DARK_HIGH) included “FP” targets and the subset of “TF” targets that were positioned along the axes of SGA galaxies. Then, the medium-priority targets (PV_BRIGHT_MEDIUM, PV_DARK_MEDIUM) included all other “TF” targets. Finally, any additional PV targets were signified by the lowest-priority targeting bits (PV_BRIGHT_LOW, PV_DARK_LOW). PV_BRIGHT_HIGH and PV_DARK_HIGH were scheduled for extra observations during SV3 (a total of five) to improve spectral S/N.

*B.40. BRIGHT_TOO_LOP, BRIGHT_TOO_HIP,
DARK_TOO_LOP, DARK_TOO_HIP*

These bits were used to handle ToOs in SV3—i.e., targets such as transients that need to be observed at short notice. Transient ToOs were selected from the DECam Survey of Intermediate Redshift Transients (Palmese et al. 2022), and will be described in A. Palmese et al. (2023 in preparation). In the bit-names, DARK signifies a ToO to be observed in dark time, and BRIGHT denotes a ToO that can be scheduled for *either* dark- or bright-time observations. LOP indicates a “low priority” ToO, which would be prioritized below all primary targets and most secondaries.¹⁶³ HIP signifies a “high-priority” ToO, which would be prioritized above *all* other DESI targets, including primaries. The general mechanisms by which ToOs are handled are discussed more in Section 3.2.2 of Myers et al. (2023) and Section 5.4 of Schlafly et al. (2023).

ORCID iDs

S. Ahlen  <https://orcid.org/0000-0001-6098-7247>
 S. Alam  <https://orcid.org/0000-0002-3757-6359>
 D. M. Alexander  <https://orcid.org/0000-0002-5896-6313>
 A. Anand  <https://orcid.org/0000-0003-2923-1585>
 F. Andrade-Oliveira  <https://orcid.org/0000-0003-0171-0069>
 E. Armengaud  <https://orcid.org/0000-0001-7600-5148>
 J. Asorey  <https://orcid.org/0000-0002-6211-499X>
 S. Avila  <https://orcid.org/0000-0001-5043-3662>
 A. Aviles  <https://orcid.org/0000-0001-5998-3986>
 S. Bailey  <https://orcid.org/0000-0003-4162-6619>
 A. Balaguera-Antolínez  <https://orcid.org/0000-0001-5028-3035>
 O. Ballester  <https://orcid.org/0000-0002-7126-5300>
 A. Bault  <https://orcid.org/0000-0002-9964-1005>
 S. F. Beltran  <https://orcid.org/0000-0001-6324-4019>

S. BenZvi  <https://orcid.org/0000-0001-5537-4710>
 L. Beraldo e Silva  <https://orcid.org/0000-0002-0740-1507>
 A. Berti  <https://orcid.org/0000-0003-3582-6649>
 F. Beutler  <https://orcid.org/0000-0003-0467-5438>
 D. Bianchi  <https://orcid.org/0000-0001-9712-0006>
 C. Blake  <https://orcid.org/0000-0002-5423-5919>
 R. Blum  <https://orcid.org/0000-0002-8622-4237>
 A. S. Bolton  <https://orcid.org/0000-0002-9836-603X>
 S. Brieden  <https://orcid.org/0000-0003-3896-9215>
 A. Brodzeller  <https://orcid.org/0000-0002-8934-0954>
 Z. Cai  <https://orcid.org/0000-0001-8467-6478>
 A. Carnero Rosell  <https://orcid.org/0000-0003-3044-5150>
 F. J. Castander  <https://orcid.org/0000-0001-7316-4573>
 J. L. Cervantes-Cota  <https://orcid.org/0000-0002-3057-6786>
 S. Chabanier  <https://orcid.org/0000-0002-5692-5243>
 E. Chaussidon  <https://orcid.org/0000-0001-8996-4874>
 J. Chaves-Montero  <https://orcid.org/0000-0002-9553-4261>
 C. Chuang  <https://orcid.org/0000-0002-3882-078X>
 S. Cole  <https://orcid.org/0000-0002-5954-7903>
 A. P. Cooper  <https://orcid.org/0000-0001-8274-158X>
 A. Cuceu  <https://orcid.org/0000-0002-2169-0595>
 T. M. Davis  <https://orcid.org/0000-0002-4213-8783>
 R. de Belsunce  <https://orcid.org/0000-0003-3660-4028>
 R. de la Cruz  <https://orcid.org/0000-0001-9908-9129>
 A. de la Macorra  <https://orcid.org/0000-0002-1769-1640>
 J. DeRose  <https://orcid.org/0000-0002-0728-0960>
 A. Dey  <https://orcid.org/0000-0002-4928-4003>
 B. Dey  <https://orcid.org/0000-0002-5665-7912>
 G. Dhungana  <https://orcid.org/0000-0002-5402-1216>
 Z. Ding  <https://orcid.org/0000-0002-3369-3718>
 K. Douglass  <https://orcid.org/0000-0002-9540-546X>
 J. Ereira  <https://orcid.org/0000-0002-0194-4017>
 S. Escoffier  <https://orcid.org/0000-0002-2847-7498>
 X. Fan  <https://orcid.org/0000-0003-3310-0131>
 K. Fanning  <https://orcid.org/0000-0003-2371-3356>
 V. A. Fawcett  <https://orcid.org/0000-0003-1251-532X>
 S. Ferraro  <https://orcid.org/0000-0003-4992-7854>
 A. Font-Ribera  <https://orcid.org/0000-0002-3033-7312>
 J. E. Forero-Romero  <https://orcid.org/0000-0002-2890-3725>
 D. Forero-Sánchez  <https://orcid.org/0000-0001-5957-332X>
 C. S. Frenk  <https://orcid.org/0000-0002-2338-716X>
 B. T. Gänsicke  <https://orcid.org/0000-0002-2761-3005>
 L. Á. García  <https://orcid.org/0000-0003-1235-794X>
 J. García-Bellido  <https://orcid.org/0000-0002-9370-8360>
 C. García-Quintero  <https://orcid.org/0000-0003-1481-4294>
 L. H. Garrison  <https://orcid.org/0000-0002-9853-5673>
 S. Gontcho A Gontcho  <https://orcid.org/0000-0003-3142-233X>
 A. X. Gonzalez-Morales  <https://orcid.org/0000-0003-4089-6924>
 V. Gonzalez-Perez  <https://orcid.org/0000-0001-9938-2755>
 O. Graur  <https://orcid.org/0000-0002-4391-6137>
 D. Green  <https://orcid.org/0000-0002-0676-3661>
 B. Hadzhiyska  <https://orcid.org/0000-0002-2312-3121>
 C. Hahn  <https://orcid.org/0000-0003-1197-0902>
 J. J. Han  <https://orcid.org/0000-0002-6800-5778>
 M. M. S Hanif  <https://orcid.org/0009-0006-2583-5006>
 H. K. Herrera-Alcantar  <https://orcid.org/0000-0002-9136-9609>
 C. Howlett  <https://orcid.org/0000-0002-1081-9410>
 D. Huterer  <https://orcid.org/0000-0001-6558-0112>

¹⁶³ The “filler” targets such as the LOW_Z and PSF_OUT targets are scheduled at a priority lower than low-priority ToOs.

- V. Iršič  <https://orcid.org/0000-0002-5445-461X>
M. Ishak  <https://orcid.org/0000-0002-6024-466X>
A. Jacques  <https://orcid.org/0000-0001-9631-831X>
L. Jiang  <https://orcid.org/0000-0003-4176-6486>
Y. P. Jing  <https://orcid.org/0000-0002-4534-3125>
S. Joudaki  <https://orcid.org/0000-0001-8820-673X>
E. Jullo  <https://orcid.org/0000-0002-9253-053X>
N. G. Karaçaylı  <https://orcid.org/0000-0001-7336-8912>
T. Karim  <https://orcid.org/0000-0002-5652-8870>
S. Kent  <https://orcid.org/0000-0003-4207-7420>
D. Kirkby  <https://orcid.org/0000-0002-8828-5463>
T. Kisner  <https://orcid.org/0000-0003-3510-7134>
F. Kitaura  <https://orcid.org/0000-0002-9994-759X>
S. E. Kposov  <https://orcid.org/0000-0003-2644-135X>
A. Kovács  <https://orcid.org/0000-0002-5825-579X>
A. Kremin  <https://orcid.org/0000-0001-6356-7424>
B. L'Huillier  <https://orcid.org/0000-0003-2934-6243>
C. Lamman  <https://orcid.org/0000-0002-6731-9329>
T.-W. Lan  <https://orcid.org/0000-0001-8857-7020>
M. Landriau  <https://orcid.org/0000-0003-1838-8528>
J. U. Lange  <https://orcid.org/0000-0002-2450-1366>
J. Lasker  <https://orcid.org/0000-0003-2999-4873>
A. Leauthaud  <https://orcid.org/0000-0002-3677-3617>
L. Le Guillou  <https://orcid.org/0000-0001-7178-8868>
M. E. Levi  <https://orcid.org/0000-0003-1887-1018>
T. S. Li  <https://orcid.org/0000-0002-9110-6163>
E. Linder  <https://orcid.org/0000-0001-5536-9241>
A. Lyons  <https://orcid.org/0000-0001-9579-0903>
M. Manera  <https://orcid.org/0000-0003-4962-8934>
C. J. Manser  <https://orcid.org/0000-0003-1543-5405>
D. Margala  <https://orcid.org/0009-0001-5897-1956>
P. Martini  <https://orcid.org/0000-0002-4279-4182>
P. McDonald  <https://orcid.org/0000-0001-8346-8394>
G. E. Medina  <https://orcid.org/0000-0003-0105-9576>
A. Meisner  <https://orcid.org/0000-0002-1125-7384>
J. Mena-Fernández  <https://orcid.org/0000-0001-9497-7266>
J. Meneses-Rizo  <https://orcid.org/0000-0003-3201-9788>
M. Mezcua  <https://orcid.org/0000-0003-4440-259X>
P. Montero-Camacho  <https://orcid.org/0000-0002-6998-6678>
J. Moustakas  <https://orcid.org/0000-0002-2733-4559>
S. Nadathur  <https://orcid.org/0000-0001-9070-3102>
L. Napolitano  <https://orcid.org/0000-0002-5166-8671>
J. A. Newman  <https://orcid.org/0000-0001-8684-2222>
J. Nie  <https://orcid.org/0000-0001-6590-8122>
R. Nikutta  <https://orcid.org/0000-0002-7052-6900>
G. Niz  <https://orcid.org/0000-0002-1544-8946>
P. Norberg  <https://orcid.org/0000-0002-5875-0440>
H. E. Noriega  <https://orcid.org/0000-0002-3397-3998>
E. Paillas  <https://orcid.org/0000-0002-4637-2868>
N. Palanque-Delabrouille  <https://orcid.org/0000-0003-3188-784X>
Z. Pan  <https://orcid.org/0000-0003-0230-6436>
D. Parkinson  <https://orcid.org/0000-0002-7464-2351>
W. J. Percival  <https://orcid.org/0000-0002-0644-5727>
I. Pérez-Ràfols  <https://orcid.org/0000-0001-6979-0125>
A. Porredon  <https://orcid.org/0000-0002-2762-0244>
F. Prada  <https://orcid.org/0000-0001-7145-8674>
R. Pucha  <https://orcid.org/0000-0002-4940-3009>
A. Raichoor  <https://orcid.org/0000-0001-5999-7923>
M. Rashkovetskyi  <https://orcid.org/0000-0001-7144-2349>
C. Ravoux  <https://orcid.org/0000-0002-3500-6635>
A. Rocher  <https://orcid.org/0000-0003-4349-6424>
C. Rockosi  <https://orcid.org/0000-0002-6667-7028>
R. Ruggeri  <https://orcid.org/0000-0002-0394-0896>
V. Ruhlmann-Kleider  <https://orcid.org/0009-0000-6063-6121>
C. G. Sabiu  <https://orcid.org/0000-0002-5513-5303>
K. Said  <https://orcid.org/0000-0002-1809-6325>
A. Saintonge  <https://orcid.org/0000-0003-4357-3450>
L. Samushia  <https://orcid.org/0000-0002-1609-5687>
E. Sanchez  <https://orcid.org/0000-0002-9646-8198>
C. Saulder  <https://orcid.org/0000-0002-0408-5633>
E. Schaan  <https://orcid.org/0000-0002-4619-8927>
E. F. Schlafly  <https://orcid.org/0000-0002-3569-7421>
H. Seo  <https://orcid.org/0000-0002-6588-3508>
A. Shafieloo  <https://orcid.org/0000-0001-6815-0337>
R. Sharples  <https://orcid.org/0000-0003-3449-8583>
W. Sheu  <https://orcid.org/0000-0003-1889-0227>
J. Silber  <https://orcid.org/0000-0002-3461-0320>
F. Sinigaglia  <https://orcid.org/0000-0002-0639-8043>
M. Siudek  <https://orcid.org/0000-0002-2949-2155>
A. Smith  <https://orcid.org/0000-0002-3712-6892>
M. T. Soumagnac  <https://orcid.org/0000-0001-6753-1488>
Z. Sun  <https://orcid.org/0000-0002-8246-7792>
G. Tarlé  <https://orcid.org/0000-0003-1704-0781>
L. A. Ureña-López  <https://orcid.org/0000-0001-9752-2830>
R. Vaisakh  <https://orcid.org/0009-0001-2732-8431>
D. Valcin  <https://orcid.org/0000-0003-0129-0620>
F. Valdes  <https://orcid.org/0000-0001-5567-1301>
M. Valluri  <https://orcid.org/0000-0002-6257-2341>
M. Vargas-Magaña  <https://orcid.org/0000-0003-3841-1836>
A. Variu  <https://orcid.org/0000-0001-8615-602X>
L. Verde  <https://orcid.org/0000-0003-2601-8770>
M. Walther  <https://orcid.org/0000-0002-1748-3745>
B. Wang  <https://orcid.org/0000-0003-4877-1659>
M. S. Wang  <https://orcid.org/0000-0002-2652-4043>
R. H. Wechsler  <https://orcid.org/0000-0003-2229-011X>
J. Yang  <https://orcid.org/0000-0001-5287-4242>
C. Yèche  <https://orcid.org/0000-0001-5146-8533>
S. Yuan  <https://orcid.org/0000-0002-5992-7586>
H. Zhang  <https://orcid.org/0000-0001-6847-5254>
C. Zhao  <https://orcid.org/0000-0002-1991-7295>
Z. Zheng  <https://orcid.org/0000-0003-1887-6732>
R. Zhou  <https://orcid.org/0000-0001-5381-4372>
Z. Zhou  <https://orcid.org/0000-0002-4135-0977>
H. Zou  <https://orcid.org/0000-0002-6684-3997>
S. Zou  <https://orcid.org/0000-0002-3983-6484>
Y. Zu  <https://orcid.org/0000-0001-6966-6925>

References

- Abbott, R., Abbott, T. D., Abraham, S., et al. 2020, *PhRvD*, 102, 043015
Abbott, T. M. C., Adamów, M., Aguena, M., et al. 2021, *ApJS*, 255, 20
Abdurro'uf, Accetta, K., Aerts, C., et al. 2022, *ApJS*, 259, 35
Abrahams, E. S., Bloom, J. S., Mowlavi, N., et al. 2020, arXiv:2011.12253
Adelberger, K. L., Steidel, C. C., Shapley, A. E., et al. 2004, *ApJ*, 607, 226
Aghanim, N., et al. 2020, *A&A*, 641, A6
Aihara, H., AlSayyad, Y., Ando, M., et al. 2022, *PASJ*, 74, 247
Aihara, H., Arimoto, N., Armstrong, R., et al. 2018a, *PASJ*, 70, S4
Aihara, H., Armstrong, R., Bickerton, S., et al. 2018b, *PASJ*, 70, S8
Albrecht, A., Bernstein, G., Cahn, R., et al. 2006, arXiv:astro-ph/0609591
Aldering, G., Adam, G., Antilogus, P., et al. 2002, *Proc. SPIE*, 4836, 61
Alexander, D. M., Davis, T. M., Chaussidon, E., et al. 2023, *AJ*, 165, 124
Allende Prieto, C., Aguado, D. S., González Hernández, J. I., et al. 2023, *ApJ*, 957, 76

- Allende Prieto, C., Cooper, A. P., Dey, A., et al. 2020, *RNAAS*, **4**, 188
- Astropy Collaboration, Price-Whelan, A. M., Lim, P. L., et al. 2022, *ApJ*, **935**, 167
- Astropy Collaboration, Price-Whelan, A. M., Sipőcz, B. M., et al. 2018, *AJ*, **156**, 123
- Astropy Collaboration, Robitaille, T. P., Tollerud, E. J., et al. 2013, *A&A*, **558**, A33
- Bellm, E. C., Kulkarni, S. R., Graham, M. J., et al. 2019, *PASP*, **131**, 018002
- Bianchi, D., Burden, A., Percival, W. J., et al. 2018, *MNRAS*, **481**, 2338
- Bianchi, D., & Percival, W. J. 2017, *MNRAS*, **472**, 1106
- Blagorodnova, N., Neill, J. D., Walters, R., et al. 2018, *PASP*, **130**, 035003
- Blanton, M. R., & Roweis, S. 2007, *AJ*, **133**, 734
- Bolton, A. S., & Schlegel, D. J. 2010, *PASP*, **122**, 248
- Bolton, A. S., Schlegel, D. J., Aubourg, É., et al. 2012, *AJ*, **144**, 144
- Busca, N., & Balland, C. 2018, arXiv:1808.09955
- Chaussidon, E., Yèche, C., Palanque-Delabrouille, N., et al. 2023, *ApJ*, **944**, 107
- Clementini, G., Ripepi, V., Molinaro, R., et al. 2019, *A&A*, **622**, A60
- Cooper, A. P., Kogosov, S. E., Allende Prieto, C., et al. 2023, *ApJ*, **947**, 37
- Cornish, N., & Robson, T. 2017, *JPhCS*, **840**, 012024
- Covey, K. R., Ivezić, Ž., Schlegel, D., et al. 2007, *AJ*, **134**, 2398
- Dark Energy Survey Collaboration, Abbott, T., Abdalla, F. B., et al. 2016, *MNRAS*, **460**, 1270
- Darragh-Ford, E., Wu, J. F., Mao, Y.-Y., et al. 2023, *ApJ*, **954**, 149
- DESI Collaboration, Abareshi, B., Aguilar, J., et al. 2022, *AJ*, **164**, 207
- DESI Collaboration, Adame, A. G., Aguilar, J., et al. 2024, *AJ*, **167**, 62
- DESI Collaboration, Aghamousa, A., Aguilar, J., et al. 2016a, arXiv:1611.00036
- DESI Collaboration, Aghamousa, A., Aguilar, J., et al. 2016b, arXiv:1611.00037
- Dey, A., Najita, J. R., Kogosov, S. E., et al. 2023, *ApJ*, **944**, 1
- Dey, A., Schlegel, D. J., Lang, D., et al. 2019, *AJ*, **157**, 168
- Dickinson, M., Giavalisco, M., & GOODS Team 2003, in *The Mass of Galaxies at Low and High Redshift*, ed. R. Bender & A. Renzini (Berlin: Springer), 324
- Dorman, C. E., Guhathakurta, P., Fardal, M. A., et al. 2012, *ApJ*, **752**, 147
- Driver, S. P., Bellstedt, S., Robotham, A. S. G., et al. 2022, *MNRAS*, **513**, 439
- Driver, S. P., Hill, D. T., Kelvin, L. S., et al. 2011, *MNRAS*, **413**, 971
- Euclid Collaboration, Scaramella, R., Amiaux, J., et al. 2022, *A&A*, **662**, A112
- Farr, J., Font-Ribera, A., & Pontzen, A. 2020, *JCAP*, **2020**, 015
- Fawcett, V. A., Alexander, D. M., Rosario, D. J., et al. 2020, *MNRAS*, **494**, 4802
- Feldman, H. A., Kaiser, N., & Peacock, J. A. 1994, *ApJ*, **426**, 23
- Fremling, C., Miller, A. A., Sharma, Y., et al. 2020, *ApJ*, **895**, 32
- Frieman, J. A., Bassett, B., Becker, A., et al. 2008, *AJ*, **135**, 338
- Gaia Collaboration, Brown, A. G. A., Vallenari, A., et al. 2018, *A&A*, **616**, A1
- Gaia Collaboration, Vallenari, A., Brown, A. G. A., et al. 2023, *A&A*, **674**, A1
- Gao, H., Jing, Y. P., Gui, S., et al. 2023, *ApJ*, **954**, 207
- Gebhardt, K., Mentuch Cooper, E., Ciardullo, R., et al. 2021, *ApJ*, **923**, 217
- Geha, M., Wechsler, R. H., Mao, Y.-Y., et al. 2017, *ApJ*, **847**, 4
- Göksel Karaçaylı, N., Martini, P., Guy, J., et al. 2024, *MNRAS*, **528**, 3941
- Górski, K. M., Hivon, E., Banday, A. J., et al. 2005, *ApJ*, **622**, 759
- Gupta, N., Srianand, R., Baan, W., et al. 2016, arXiv:1708.07371
- Guy, J., Bailey, S., Kremin, A., et al. 2023, *AJ*, **165**, 144
- Hahn, C., Aguilar, J. N., Alam, S., et al. 2023, arXiv:2306.06318
- Hahn, C., Wilson, M. J., Ruiz-Macias, O., et al. 2022, *AJ*, **165**, 253
- Hainline, K. N., Reines, A. E., Greene, J. E., & Stern, D. 2016, *ApJ*, **832**, 119
- Hildebrandt, H., Pielorz, J., Erben, T., et al. 2009, *A&A*, **498**, 725
- Hill, G. J., Lee, H., MacQueen, P. J., et al. 2021, *AJ*, **162**, 298
- Hogg, D. W., Baldry, I. K., Blanton, M. R., & Eisenstein, D. J. 2002, arXiv:astro-ph/0210394
- Holl, B., Audard, M., Nienartowicz, K., et al. 2018, *A&A*, **618**, A30
- Howlett, C., Staveley-Smith, L., & Blake, C. 2017, *MNRAS*, **464**, 2517
- Huang, X., Storfer, C., Gu, A., et al. 2021, *ApJ*, **909**, 27
- Huang, X., Storfer, C., Ravi, V., et al. 2020, *ApJ*, **894**, 78
- Hviding, R. E., Hainline, K. N., Rieke, M., et al. 2022, *AJ*, **163**, 224
- Ivezić, Ž., Kahn, S. M., Tyson, J. A., et al. 2019, *ApJ*, **873**, 111
- Kadowaki, J., Zaritsky, D., Donnerstein, R. L., et al. 2021, *ApJ*, **923**, 257
- Kim, A. G., & Linder, E. V. 2020, *PhRvD*, **101**, 023516
- Knigge, C., Baraffe, I., & Patterson, J. 2011, *ApJS*, **194**, 28
- Krolewski, A., Ferraro, S., Schlafly, E. F., & White, M. 2020, *JCAP*, **2020**, 047
- Krolewski, A., Ferraro, S., & White, M. 2021, *JCAP*, **2021**, 028
- Kuijken, K., Heymans, C., Dvornik, A., et al. 2019, *A&A*, **625**, A2
- Laigle, C., McCracken, H. J., Ilbert, O., et al. 2016, *ApJS*, **224**, 24
- Lan, T.-W., Tojeiro, R., Armengaud, E., et al. 2023, *ApJ*, **943**, 68
- Law, N. M., Kulkarni, S. R., Dekany, R. G., et al. 2009, *PASP*, **121**, 1395
- Li, T. S., Kogosov, S. E., Zucker, D. B., et al. 2019, *MNRAS*, **490**, 3508
- Lindegren, L., Hernández, J., Bombrun, A., et al. 2018, *A&A*, **616**, A2
- Loveday, J., Norberg, P., Baldry, I. K., et al. 2012, *MNRAS*, **420**, 1239
- Mao, Y.-Y., Geha, M., Wechsler, R. H., et al. 2021, *ApJ*, **907**, 85
- Masters, D. C., Stern, D. K., Cohen, J. G., et al. 2017, *ApJ*, **841**, 111
- Masters, D. C., Stern, D. K., Cohen, J. G., et al. 2019, *ApJ*, **877**, 81
- Mateos, S., Alonso-Herrero, A., Carrera, F. J., et al. 2012, *MNRAS*, **426**, 3271
- McConnachie, A. W., Ibata, R., Martin, N., et al. 2018, *ApJ*, **868**, 55
- McNaught-Roberts, T., Norberg, P., Baugh, C., et al. 2014, *MNRAS*, **445**, 2125
- Mezcua, M., & Domínguez Sánchez, H. 2020, *ApJL*, **898**, L30
- Miller, T., Doel, P., Gutierrez, G., et al. 2023, arXiv:2306.06310
- Myers, A. D., Moustakas, J., Bailey, S., et al. 2023, *AJ*, **165**, 50
- Myers, A. D., Palanque-Delabrouille, N., Prakash, A., et al. 2015, *ApJS*, **221**, 27
- Nidever, D. L., Dey, A., Fasbender, K., et al. 2021, *AJ*, **161**, 192
- Nidever, D. L., Dey, A., Olsen, K., et al. 2018, *AJ*, **156**, 131
- Palanque-Delabrouille, N., Yèche, C., Myers, A. D., et al. 2011, *A&A*, **530**, A122
- Palmese, A., BenZvi, S., Bailey, S., et al. 2021, GCN, 30923, 1
- Palmese, A., Bom, C. R., Mucesh, S., & Hartley, W. G. 2023, *ApJ*, **943**, 56
- Palmese, A., Wang, L., Chen, X., et al. 2022, TNSAN, 107, 1
- Pàris, I., Petitjean, P., Aubourg, É., et al. 2018, *A&A*, **613**, A51
- Prada, F., Ereza, J., Smith, A., et al. 2023, arXiv:2306.06315
- Raichoor, A., Eisenstein, D. J., Karim, T., et al. 2020, *RNAAS*, **4**, 180
- Raichoor, A., Moustakas, J., Newman, J. A., et al. 2023, *AJ*, **165**, 126
- Ramírez-Pérez, C., Pérez-Ràfols, I., Font-Ribera, A., et al. 2024, *MNRAS*, **528**, 6666
- Ravoux, C., Armengaud, E., Walther, M., et al. 2020, *JCAP*, **2020**, 010
- Ravoux, C., Karim, M. L. A., Armengaud, E., et al. 2023, *MNRAS*, **526**, 5118
- Rocher, A., Ruhlmann-Kleider, V., Burtin, E., et al. 2023, *JCAP*, **2023**, 016
- Ross, A. J., Bautista, J., Tojeiro, R., et al. 2020, *MNRAS*, **498**, 2354
- Ross, A. J., et al. 2020, *MNRAS*, **498**, 2354
- Ruiz-Macias, O., Zarrouk, P., Cole, S., et al. 2020, *RNAAS*, **4**, 187
- Rykoft, E. S., Rozo, E., Busha, M. T., et al. 2014, *ApJ*, **785**, 104
- Satyapal, S., Abel, N. P., & Secrest, N. J. 2018, *ApJ*, **858**, 38
- Saulder, C., Howlett, C., Douglass, K. A., et al. 2023, *MNRAS*, **525**, 1106
- Sawicki, M., Arnouts, S., Huang, J., et al. 2019, *MNRAS*, **489**, 5202
- Schlafly, E. F., Kirkby, D., Schlegel, D. J., et al. 2023, *AJ*, **166**, 259
- Schlafly, E. F., Meisner, A. M., & Green, G. M. 2019, *ApJS*, **240**, 30
- Scoville, N., Aussel, H., Brusa, M., et al. 2007, *ApJS*, **172**, 1
- Segev, N., & Ofek, E. O. 2019, *MNRAS*, **484**, 2462
- Sesar, B., Hernitschek, N., Mitrović, S., et al. 2017, *AJ*, **153**, 204
- Sevilla-Noarbe, I., Bechtol, K., Carrasco Kind, M., et al. 2021, *ApJS*, **254**, 24
- Silber, J. H., Fagrelus, P., Fanning, K., et al. 2023, *AJ*, **165**, 9
- Vasiliev, E., & Baumgardt, H. 2021, *MNRAS*, **505**, 5978
- Wang, F., Fan, X., Yang, J., et al. 2017, *ApJ*, **839**, 27
- Weaver, J. R., Kauffmann, O. B., Ilbert, O., et al. 2022, *ApJS*, **258**, 11
- Wright, A. H., Hildebrandt, H., Kuijken, K., et al. 2019, *A&A*, **632**, A34
- Wu, J. F., Peek, J. E. G., Tollerud, E. J., et al. 2022, *ApJ*, **927**, 121
- Yang, J., Fan, X., Gupta, A., et al. 2023, *ApJS*, **269**, 27
- Yang, J., Wang, F., Fan, X., et al. 2019, *ApJ*, **871**, 199
- Yasuda, N., Tanaka, M., Tominaga, N., et al. 2019, *PASJ*, **71**, 74
- Yèche, C., Palanque-Delabrouille, N., Claveau, C.-A., et al. 2020, *RNAAS*, **4**, 179
- York, D. G., Adelman, J., Anderson, J. E. J., et al. 2000, *AJ*, **120**, 1579
- Yu, J., Zhao, C., Gonzalez-Perez, V., et al. 2024, *MNRAS*, **527**, 6950
- Yuan, S., Zhang, H., Ross, A. J., et al. 2024, *MNRAS*, **530**, 947
- Zaritsky, D., Donnerstein, R., Dey, A., et al. 2019, *ApJS*, **240**, 1
- Zaritsky, D., Donnerstein, R., Karunakaran, A., et al. 2022, *ApJS*, **261**, 11
- Zhou, R., Dey, B., Newman, J. A., et al. 2023, *AJ*, **165**, 58
- Zhou, R., Newman, J. A., Dawson, K. S., et al. 2020, *RNAAS*, **4**, 181
- Zhou, R., Newman, J. A., Mao, Y.-Y., et al. 2021, *MNRAS*, **501**, 3309
- Zonca, A., Singer, L., Lenz, D., et al. 2019, *JOSS*, **4**, 1298
- Zou, H., Zhou, X., Fan, X., et al. 2017, *PASP*, **129**, 064101
- Zou, S., Jiang, L., Cai, Z., et al. 2024, *ApJ*, **960**, 34